Università degli Studi di Ferrara

DOCTORAL COURSE IN ENGINEERING SCIENCE

CYCLE XXXIII

Director Prof. Stefano Trillo

Target Generation Techniques for Multi-Axis Random Vibration Control: Development, Implementation and Experimental Validation

Scientific/Disciplinary Sector ING-IND/13

Candidate
Dott. Giacomo D'Elia

Supervisor
Prof. Giorgio Dalpiaz

Co-Advisor
Prof. Emiliano Mucchi

Years 2017/2020

Studiate. Anche se nella vita è meglio furbi che colti. Anzi: proprio per questo. Per non arrendersi a chi ci vorrebbe più furbi che colti. Perché la cultura rende liberi, critici e consapevoli. Non rassegnatevi a chi vi vorrebbe opportunisti e docili e senza sogni. Studiate. Meglio precari oggi che servi per sempre.

Ilvo Diamanti

DECLARATION OF AUTHORSHIP

I, Giacomo D'Elia, declare that this thesis titled, "Target Generation Techniques for Multi-Axis Random Vibration Control: Development, Implementation and Experimental Validation " and the work presented in it are my own. I confirm that:

- This work was done wholly while in candidature for Doctoral Degree at Università degli Studi di Ferrara;
- This work has been supervised and approved by Prof. Giorgio Dalpiaz and Prof. Emiliano Mucchi;
- This work is part of the papers

  [1] U. Musella, G. D'Elia, A. Carrella, B. Peeters, E. Mucchi, F. Marulo and P. Guillaume. "A minimum drives automatic target definition procedure for multi-axis random control testing." In: *Mechanical Systems and Signal Processing* 107 (2018), pp. 452-468.

  [2] G. D'Elia, U. Musella, E. Mucchi, P. Guillaume and B. Peeters. "Analyses of drives power reduction techniques for multi-axis random vibration control tests". In: *Mechanical Systems and Signal Processing* 135 (2020), 106395.

  [3] G. D'Elia and E. Mucchi. "Comparison of single-input single-output and multi-input multi-output control strategies for performing sequential single-axis random vibration control test." In: *Journal of Vibration and Control* 26 (2020), pp. 1988-2000.
- Where I have consulted the published work of others, this is always clearly attributed;
- Where I have quoted from the work of others, the source is always given;
- I have acknowledged all main sources of help;

Ferrara, 29/07/2021 Giacomo D'Elia

CONTENTS

LIST OF FIGURES

LIST OF TABLES

ACRONYMS

CSD	Cross Spectral Density
DAC	Digital-to-Analog Converter
DoF	Degree-of-Freedom
EDRM	Extreme Dynamic Responses Method
EIOM	Extreme Inputs/Outputs Method
EMA	Experimental Modal Analysis
ERS	Extreme Response Spectrum
FDS	Fatigue Damage Spectrum
FEM	Finite Element Method
IMMAT	Impedance-Matched Multi-Axial Test
IDM	Independent Drives Method
IRM	Independent References Method
LTI	Linear Time-Invariant
MAC	Modal Assurance Criteria
MDM	Minimum Drives Method
MIMO	Multi-Input Multi-Output
MSDM	Minimum Single Drive Method
OCBU	Orthogonal Coupling Bearings Unit
PSD	Power Spectral Density
SDM	Spectral Density Matrix
SISO	Single-Input Single-Output
SVD	Singular Value Decomposition
TTF	Time to Failure
VIBCO	VIBration COntrol

NOMENCLATURE

Latin symbols

a	acceleration RMS value
b	inverse power law exponent
C	Basquin's law constant
D	damage accumulation
E	Young's modulus
$\mathbf{F}$	matrix derived from the manipulation of the impedance matrix
G	shear modulus
$\mathbf{G^i}$	matrix derived from the manipulation of i-th column and i-th row of the impedance matrix
$\mathbf{H}$	transfer functions matrix
K	scale factor between response SDMs
k	Basquin's fatigue exponent
$\mathbf{L}$	Cholesky factor
$\mathbf{M_s}$	matrix multisine
$N0$	total number of zero up-crossing
n_0^+	number of zero up-crossing per second
n_p^+	number of peaks per second
P	matrix trace
p_a	probability density distribution of counted cycles
$\mathbf{Q}$	von Mises coefficient matrix
S_{ii}	Power Spectral Density of the i-th channel
S_{ij}	Cross Spectral Density between the i-th and j-th channels

$\mathbf{S}_{vM}$	Power Spectral Density of the von Mises equivalent stress
$\mathbf{S_{uu}}$	drives Spectral Density Matrix
$\mathbf{S_{xx}}$	acceleration Spectral Density Matrix recorded at the measured point
$\mathbf{S_{yy}^{ref}}$	reference Spectral Density Matrix
$\mathbf{S_{yy}}$	acceleration Spectral Density Matrix recorded at the control point
$\mathbf{S}_{\sigma\sigma}$	stress Spectral Density Matrix
T	fatigue life in seconds
$\mathbf{T}$	matrix derived from the manipulation of the transfer functions matrix
$\mathbf{u}(\mathbf{t})$	time-dependent drives vector
$\mathbf{W^{ij}}$	matrix whose vector sum between elements provides the control CSD (S_{ij})
$\mathbf{y}(\mathbf{t})$	time-dependent accelerations vector
$\mathbf{Z}$	mechanical impedance matrix

Greek symbols

α_i	*i*-th spectral width parameter
β	scale factor of the cross-PSD in single-axis control testing
γ_{ij}	coherence of the Cross Spectral Density between the *i*-th and *j*-th channels
δ	ratio between von Mises PSDs at resonance frequencies
θ_{ij}	phase angle between the *i*-th and *j*-th channels of matrix **F**
λ_i	*i*-th spectral moment
ξ_{ij}	phase angle between the *i*-th and *j*-th channels of matrix **T**
σ	vector of the six independent stress-tensor components
σ_{vM}	von Mises equivalent stress RMS value

ϕ_{ij}	phase angle of the Cross Spectral Density between the *i*-th and *j*-th control channels
ψ_{ij}	phase angle between the *i*-th and *j*-th channels of matrix $\mathbf{G^i}$
ζ	damping ratio

Subscripts & superscripts

$\square^T$	transpose of a matrix
$\square^H$	complex conjugate transpose of a matrix
$\square^{-1}$	inverse of a matrix
$\square^\dagger$	*Moore-Penrose* pseudo-inverse of a matrix
$\hat{\square}$	denote the matrix has been estimated
$\square'$	complex conjugate of a matrix element
$\mathrm{Tr}(\square)$	trace operator

1

INTRODUCTION

1.1 THE EVOLUTION OF VIBRATION CONTROL TESTING

Vibration control (VibCo) tests are performed to verify that a system and all its sub-components can withstand the vibration environment during its operational life. These tests aim to accurately replicate via controlled shaker excitation the in-service structural response of the specimen under test. Nowadays, the procedures for performing vibration control testing are based on guidances and test methodologies provided by international Standards, e.g MIL-STD 810 [4], GAM-EG 13 [5] and STANAG-4370 [6].

The first guidelines for vibration testing were born for military applications at the end of War World II. The war efforts, despite having brought countless deaths and devastated entire nations, it stimulated innovation in different mechanical fields. The arms race boosted new design of aircraft, ships, vehicles and general equipments. At that time, it became apparent the importance of performing qualification tests on new equipments prior to use, in order to provide assurance that the equipments would perform as expected in the operational environment for which they were designed. Prior to 1940, vibration testing was practically non-existent [7]. By the 1960s vibration test machines were advancing, as well as the understanding of the vibration phenomena. The World War II provided the great push that drove the military and industry to expand testing capabilities but it left a gap: standardization [8]. The decision made in 1960 and executed 1962 with the release of MIL-STD 810A [9] was the first attempt of providing standard procedures for vibration testing. MIL-STD 810A was a multi-method approach to vibration tests performed in a single axis at a time [10]. At the early '60s indeed, the available excitation systems

were single axis shakers. By exploiting a single axis shaker, the simplest way to expose a test article to an excitation in multiple axes was to perform a sequential Single-Input Single-Output (SISO) test: sequentially, the test article is rotated, the test set-up changed and a new test is performed with the required vibration profile as test specification. For decades, this test procedure has been established as a standard method to recreate in the laboratory the multi-directional nature of a real vibration environment [4, 5, 6, 11].

Practical aspects, linked for instance to the sizes of the article to be tested or to issues in changing multiple times the test set-up, can make the execution of sequential SISO test challenging (or even impossible) and time consuming. However, the most critical aspect of SISO vibration testing is that it poorly represents any real vibration environment and therefore can lead to an unacceptable time to failure estimation for the unit under test and different failure modes [12]. This has been shown in small-scale problems, such as printed wiring boards testing (where the inductor are critical components) [13] or thin plates [14, 15], but also in large-scale tests such as large spacecraft vibration testing [16, 17].

The only alternative to overcome the single-axis test limitations is to apply a simultaneous multi-axial excitation performing a Multi-Input Multi-Output (MIMO) vibration control test. Several publications show the advantages in replicating the in-serve conditions by exciting in more directions simultaneously. The works of Daborn on aerodynamically excited structures [18, 19] show how increasing the number of control channels and trying to match the operational mechanical impedance allows to closely match the response in location that are not controlled. These observations are at the basis of the so-called *IMMAT (Impedance-Matched Multi-Axial Test)* approach [20]. Roberts in [21] shows that the (known) environmental replication further improves by increasing the number of shakers and adopting rectangular control strategies. Similar benefits on the use of rectangular control techniques for multi-shaker systems are shown by Underwood and Keller in [22]. Whiteman in [23] and [24] compares single axis and multi-axis test methods for a simple notch cantilever beam structure. The works point out the inadequacy of the single axis procedure due to overestimated time to failure result even for such simple structure. Mršnik *et al.* in [25], by comparing different multi-axial criteria for vibration-fatigue analysis, show that combinations of two uncorrelated vibration sources can effect the resulting crack location on the specimen under

test. Himelblau *et al.* in [26] provide a motivational to perform MIMO VibCo testing by showing that tri-axial excitation could cause approximately twice the fatigue damage as similar test levels in single axis testing.

Even though the benefits of MIMO testing are clear and widely accepted by the environmental engineering community, this practice experienced a very slow growth. Initially, it was due to the available technology in terms of excitation mechanisms and computational power for the data acquisition hardware and vibration controllers. The first documented attempt to simultaneous multi-axial excitation is dated 1958 [27]. However, the first multi-input control algorithm was developed only twenty years later, in 1978 by David Smallwood from Sandia National Laboratories as documented in the 1982's publication *A Random Vibration Control System for Testing a Single Test Item with Multiple Inputs* [28]. Nowadays, the modern MIMO vibration control strategies rely on the work of Underwood [29], whose first patent on the topic is dated 1994 [30]. Recently, the increased complexity, sizes and cost of the test specimens built up the concern about replicating as close as possible the environments to be tested [31]. The recent update to include tailoring guidelines for multi-exciter testing in the last release of the United State Military Standard [32] highlights the will of the environmental engineering community to turn the multi-axis vibration control testing into the main reference procedure.

There are different types of MIMO VibCo tests (random, swept sine, time waveform replication) depending on the environment the test article needs to be exposed [33]. For automotive and aerospace systems and subsystems, a random VibCo test is required for all the main mechanical and electrical components [34]. Typical scenarios are the road excitation or the response to a diffuse acoustic field [35]. In the recent years, several publications addressed the effects of non-Gaussian or non-stationary vibration environments on the fatigue life estimation [36, 37, 38]. In particular, Palmieri et al. in [39] compares both the phenomena with an intensive numerical and experimental research carried out on Y-shaped specimens. The test results highlight that the combination of a non-stationary, non-Gaussian excitation produces higher damage accumulation, resulting in a shorter fatigue life of the specimen under test. To deal with this issue, innovative vibration control algorithms and methods have been recently proposed [40, 41, 42, 43]. Nevertheless, it is important to notice that all the techniques and methodologies described in the following of this thesis refer to broadband random Gaussian vibration environments.

1.2 MIMO TARGET GENERATION TECHNIQUES

To perform a VibCo test, the test engineer specifies the control target (test specification) and the control algorithm has to provide the input voltages to the shaker's amplifier by which the excitation system is capable to replicate the user-defined target.

For the SISO case the test specification is a Power Spectral Density (PSD, usually in g^2/Hz). The reference PSD could come directly from field measured data and taken as test specification after being averaged, smoothed or enveloped. Otherwise, especially for durability tests where it is impractical to replicate the real vibration environment due to cost and time reasons, the test specification is defined using Mission Synthesis procedures typically based on single axis spectral damage equivalence techniques [44]. Typical synthesized profiles, categorized according to the specific specimen, are provided by the Standards [4, 5].

In the MIMO case, it is possible to define required test levels for multiple control channels that will be controlled simultaneously. Additional information about the cross-correlation between the control channels is also included. This information must be provided in terms of Cross Spectral Densities (CSDs) between pairs of control channels by defining desired phase and coherence profiles. The definition of these terms is essential to also replicate the cross-correlation that naturally exists between difference responses [45]. These terms are also controlled by modern vibration controllers [46]. For these systems the control target is thus a full reference Spectral Density Matrix (SDM) in the frequency band of interest, where the diagonal of the matrix is composed by the PSDs (test specifications), and the off-diagonal terms are the reference CSDs. The target definition process plays already a key role for MIMO random VibCo tests as documented in recent studies [47, 48, 49, 50, 51].

Theoretically, a successful MIMO random VibCo test can be performed in case the operational environment is fully replicated in the laboratory, meaning that i) the nature of the operational loads can be exactly replicated with the available exciter(s); ii) the boundary conditions can be also exactly replicated with the available fixtures; iii) operational measurements are available for all the control points [52]. This approach require fully available operational measurements. Unfortunately, operational measurements are not always available and often the test specifications are provided just in terms of PSDs at the con-

trol locations. This is due to several reasons. First of all, the gradual transition from sequential SISO testing to simultaneous multi-axial testing needs to face the aforementioned legacy of SISO standards and specifications, provided in terms of PSDs only. Second, the standardization of the CSD terms is impractical to implement in a specification due to a lack of knowledge that makes challenging (and even impossibile) to average, smooth or envelope coherence and phase information from different operational conditions. The definition of the MIMO control target with no a-priori knowledge of the cross-correlation between control channels is very challenging. Filling in the off-diagonal terms, in fact, must guarantee that the reference SDM will have a physical meaning, i.e. it must be realizable and controllable [53]. This condition can be reached only if the MIMO control target is a positive (semi)definite matrix [54].

To overcome this algebraic constraint, the most commonly practised procedure to fill in the reference SDM is the *Independent References Method (IRM)*: the reference SDM is specified as a diagonal matrix by simply setting low coherence for all the cross terms. Due to the low coherence values, the phase specifications are not required. The CSD terms are irrelevant and the phase parameters are essentially a random variables. This MIMO target generation procedure assumes that the multiple vibration requirements are independent from each other in the entire frequency band. Even if this hypothesis cannot be considered truthful for all the real vibration environments, the *IRM* is very simple and user-friendly. For these reasons it is the procedure suggested by the Standards when no information about the CSDs are available [32].

De facto, the solution of finding a full reference matrix with fixed PSD terms is not unique. As pointed out in United State Military Standard [4], the choice of setting appropriate values to fill in the full reference control matrix *must reflect the desires of a knowledgeable environmental test engineer*. These considerations reflect the need of having a method, rather than standardized values, to define the specification of a multi-axial test.

The first attempt of MIMO target generation algorithm has been proposed by Smallwood in the late 80's [55]. The methodology has been finally developed around 20 years later when the author presented the so-called *Extreme Inputs/Outputs Method (EIOM)* [56]. Smallwood with the *EIOM*, in addition to providing a methodology to fill in the MIMO control target, tackles the problem of *meeting the minimum drives criteria*. The idea of minimising the drives power required to reach the test specifications is an attractive and interesting

solution, because the achievable power levels are often a limiting aspect for multi-exciter test. On the one hand, the drives power reduction allows to carry out the control test without over-stressing the excitation system, that means preserving the often expensive test equipment. On the other hand, it offers the possibility to fully exploit the excitation system capabilities preventing the data acquisition DAC (Digital-to-Analog Converter) overloads. The idea behind the method is to find the CSDs that minimize the input power required by the shakers to reach the reference PSDs. Unfortunately, the *EIOM* is not able to guarantee that the final target will be positive (semi)definite. This makes the method not suitable for practical testing. This issue is further tackled by the same author that proposes, in the later work [57], a constrained optimization algorithm to superimpose the required property.

At the author' knowledge, the only other MIMO target generation technique available in the literature is the *Independent Drives Method (IDM)* [58]. This method is also cited in the Annex E of reference [32] as a possible solution for minimizing the shakers power. The basic idea of the *IDM* is to find a set of uncorrelated inputs able to reproduce the desired control PSDs.

As highlighted in standards for multi-axial testing [4]: *"although an active area of research, general techniques to address minimum drives criteria have not been formally established at the time of publication"* (2014). It is clear that meeting the minimum drives requirements is still an open discussion in the multi-axial testing community.

1.3 MAIN PURPOSE AND ORIGINAL ASPECTS OF THE THESIS

As highlighted in the previous sections, nowadays multi-axis control tests are still considered a *pioneering* testing methodology due to the high degree of expertise needed to perform these tests and decades of single axis controlled excitation that built a legacy of SISO standards. As a consequence, the sequential single axis control testing is currently the most common procedure in the industrial practice. Therefore, the first objective of this thesis is to point out the limitations of SISO control strategy and the benefits that can be achieved by using the MIMO technology. The aim is to definitely push the MIMO control into the main standard practice for laboratory testing. In this context, the thesis provides in Chapter 3 a detailed study followed by piratical examples on how to manage the MIMO control target in order to better exploit the evident

potential of MIMO control. The novelties related to this particular research activity has been published in *Journal of Vibration and Control* of *SAGE journals*:

[3] G. D'Elia and E. Mucchi. "Comparison of single-input single-output and multi-input multi-output control strategies for performing sequential single-axis random vibration control test." In: *Journal of Vibration and Control* 26 (2020), pp. 1988-2000.

However, the main purpose of this thesis is to tackle the issue of defining the MIMO control target in case where operational measurements are not fully available and the test specifications are provided in terms of PSDs only. As previously highlighted, the issue of the *minimum drives criteria* is still an open topic which requires deeper investigations. Indeed, the nowadays state-of-the-art solutions contain some flaws which render the techniques unusable for practical laboratory vibration control tests. Therefore, on the basis of the needs pointed out in this topic, Chapter 4 of this thesis discloses two novel MIMO target generation techniques with the purpose of finally establishing a general methodology to be used in standard practice.

The first MIMO target technique, namely *Minimum Drives Method (MDM)*, is a newly developed algorithm that automatically provides the full reference SDM without modifying the PSDs, considered as test specifications. The innovative feature is the capability of minimizing the total power required by the shakers to match the reference PSDs and, at the same time, to directly guarantee realizable and controllable reference SDM. The input power suggested by the *MDM* is directly linked to the excitation that copes with the system's dynamics. Therefore the subsequent natural motion of the unit under test ensures good control performances. The analytical derivation and the implementation steps of the *MDM* are described in the article published by the journal *Mechanical Systems and Signal Processing*:

[1] U. Musella, G. D'Elia, A. Carrella, B. Peeters, E. Mucchi, F. Marulo and P. Guillaume. "A minimum drives automatic target definition procedure for multi-axis random control testing." In: *Mechanical Systems and Signal Processing* 107 (2018), pp. 452-468.

Moreover, the *MDM* has been recently implemented in the environmental control solutions of *Simcenter Testlab* (release 2019.1.3). Simcenter Testlab is the test-based engineering software of *SIEMENS*, which is the world leader for providing software and data acquisition hardware for vibro-acoustic analysis.

The second MIMO target generation technique instead, namely *Minimum Single Drive Method (MSDM)*, wants to be an alternative solution when the power required by the multiple-exciter system is mostly exploited by a single shaker. In these cases, in order to safely push the excitation system and to avoid DACs overloads, it could be more advantageous to focus the method for minimising the power of the overloaded drive instead of reduce the overall power of the system. Also the algorithm of *MSDM* is fully automated and it guarantees the generation of realizable reference SDM. A review of the entire work carried out on the MIMO target generation techniques and the details of the *MSDM* have been published in the journal *Mechanical Systems and Signal Processing*:

[2] G. D'Elia, U. Musella, E. Mucchi, P. Guillaume and B. Peeters. "Analyses of drives power reduction techniques for multi-axis random vibration control tests". In: *Mechanical Systems and Signal Processing* 135 (2020), 106395.

Furthermore, the opening sections of this chapter evidence that, all the MIMO target techniques available in the literature are focused on the drives power minimisation, thus paying special attention just on the safety of the excitation system without considering the impact on the specimen under test. At the author' knowledge, there are no works that investigate the effects caused by different control target techniques directly on the specimen. With this purpose, the last novelty proposed in Chapeter 5 of this thesis is an innovative MIMO target generation technique, which effectively copes with the fatigue-life of the specimen to be tested. The present technique, called *Extreme Dynamic Response Method (EDRM)*, aims to combine the test specifications in order to maximise the responses measured in some critical points of the specimen under test. Maximising the dynamic response of the specimen means to recreate in the laboratory the most severe vibration environment possible. Therefore, the extreme environmental conditions of the laboratory guarantee the specimen experiences the shortest time-to-failure, with a fatigue damage comparable or, at least, heavier with respect to the operational one. It is worth to notice that, the basic outline of the *EDRM* algorithm is based on the same concepts of the two other novel techniques presented in this thesis. Thus, also the *EDRM* is a fully automated procedure which always provides positive definite control matrices, i.e. realizable and controllable reference SDMs that are suitable for performing real random vibration control tests.

In conclusion, the original contribution of this thesis is to assess the definition of the MIMO control target focusing the results on two distinct aspects, both of which are critical issues on the field of environmental vibration control testing. The first aspect links to the safety and protection of the delicate test equipment, which are very expensive in most of the cases. The other aspect instead, is directly focused to the dynamic of the specimen under test and thus links to its fatigue-life. For both the addressed aspects, this thesis proposes novel MIMO target generation techniques, offering an extensive and complete analysis on the actual test procedures for performing multi-axial random vibration control testing.

1.4 OVERVIEW OF THE THESIS

The following is a brief overview of the various chapters:

Chapter 2 summarizes the theoretical background of MIMO random vibration control testing. Even if the intent of this thesis is not to provide the specifics of the control algorithms used in the conduct of multi-axis testing, some theoretical concepts are needed to highlight the key role of the MIMO control target definition. Therefore, this chapter presents the basic outline of the MIMO control strategy and the mathematical properties of the reference SDM.

Chapter 3 is devoted to address the first purpose of this manuscript, i.e. to investigate the use of SISO and MIMO control strategies for performing sequential single axis vibration control tests. In particular, the study presented in this chapter tackles the issue of reaching high level cross axis responses during those tests. In order to compare the capabilities of the two control strategies, the chapter presents a test campaign carried out on an automotive component by exploiting two different test facilities: a single axis shaker and the three degrees of freedom shaker table at the University of Ferrara. The analysis points out the inadequacy of the SISO control technique for performing single axis test. The coupling between the excitation system and the test specimen causes cross axis excitations that compromise the test validity. The MIMO control strategy instead, besides the feedback control of the main axis, allows the simultaneous vibration control along the two cross axes thus improving the quality of the single axis test.

Chapter 4 deals with the description of the MIMO control target techniques focused on the drives power reduction. The first part of the chapter critically analyses the two state-of-the-art drives power reduction procedures, i.e. the *EIOM* [56, 57] and the *IDM* [58]. The second part of the chapter instead, explains in detail the mathematical formulation and the implementation process of the proposed procedures, i.e. the *MDM* and the *MSDM*. A test campaign with the three-axial electrodynamic shaker of the University of Ferrara is carried out in order to point out the pros and cons of each procedure and to investigate the impact on the random control strategy of each target generation algorithm. The test results show how the developed procedures are able to significantly reduce, with respect to common choices normally used to obtain a positive semi-definite target matrix, the total drives power required to meet the PSD specifications. The single drives will also show power reductions. This enhancement opens the possibility to further increase the test levels (in terms of *gRMS*) avoiding DACs overloads or physical limitations of the excitation systems. It is also worth to notice that reducing the drive power required to match a target also means to work in safety with the expensive testing equipment.

Chapter 5 is dedicated to the investigation of the MIMO control target techniques focusing the analysis on the fatigue-life of the specimen under test. After a briefly introduction on the basic concepts of the fatigue theory, the chapter provides the mathematical implementation of the *EDRM* algorithm, that is the presented MIMO target technique for the dynamic response maximization. In order to underline the advantages of the proposed procedure compared to the others available in the literature, 48 ad-hoc designed specimens are tested in the laboratory of the University of Ferrara by using the 3-DoF shaker table. In particular, the specimens are rectangular section beam, 250 mm long, made of aluminium alloy and connected to the shaker table in cantilever configuration. The fatigue test campaign shows remarkable results. The *EDRM* always provides the shortest time-to-failure, confirming that the present procedure is capable of combing the test specifications into the most severe vibration environment.

Chapter 6 is devoted to the concluding remarks of the thesis.

2

MIMO RANDOM VIBRATION CONTROL: THEORETICAL BACKGROUND

In order to better understand the key role of the MIMO control target in multi-axis vibration testing, it is necessary to review some basic of the MIMO control theory. This chapter also clarifies the notation used throughout the entire manuscript. As shown in the following, the MIMO systems are characterised by the use of matrices. The size of the matrix is typically stated as $[n, m]$, where n is the number of rows and m is the number of columns. In this work, three dimensional matrices are also used where the third dimension is typically samples either in time or frequency domain. It is assumed that, if the matrix has three dimensions, then the operations are performed on each two dimensional matrix along the third dimension. For example, if the matrix is a matrix of frequency response functions, matrix operations will be performed at each frequency line. Moreover, in this work most of the derivations are in the frequency domain, but for the sake of clarity, the frequency dependence notation is omitted. Therefore, all the arrays are functions of the frequency (in Hz) if not specified otherwise.

2.1 FREQUENCY DOMAIN TRANSFER FUNCTION RELATIONSHIPS

A general Multiple-Input Multiple-Output (MIMO) linear system is represented in Figure 1. The multiple inputs (m) and the multiple outputs (ℓ) are represented by the two vectors, $\mathbf{u}(t) = \{u_1(t), ..., u_m(t)\}^T$ and $\mathbf{y}(t) = \{y_1(t), ..., y_\ell(t)\}^T$, respectively. It is important to note that generally, there is no one to one correspondence between inputs and outputs, and the number of inputs and the number of outputs may be different ($\ell \geqslant m$).

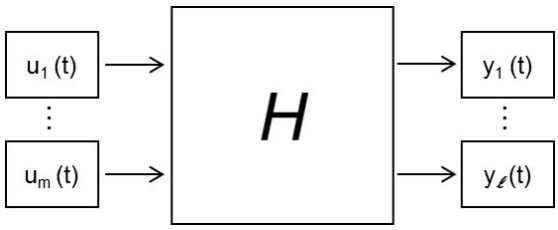

Figure 1: MIMO linear system

Let $\mathbf{U} \in \mathbb{C}^{m\times 1}$ be the column vector representing the *Fourier transform* of the m recorded input signals, and $\mathbf{Y} \in \mathbb{C}^{\ell\times 1}$ be the column vector of the *Fourier transform* of the ℓ recorded output signals

$$\mathbf{U} = \begin{bmatrix} U_1 \\ U_2 \\ \vdots \\ U_m \end{bmatrix} \qquad \mathbf{Y} = \begin{bmatrix} Y_1 \\ Y_2 \\ \vdots \\ Y_\ell \end{bmatrix} \tag{1}$$

Thus, it is possible to estimate the input/output (power) Spectral Density Matrices as [59]

$$\mathbf{S_{uu}} = E[\mathbf{U}\mathbf{U}^H] = \begin{bmatrix} S_{uu,11} & \dots & S_{uu,1m} \\ \vdots & \ddots & \vdots \\ S_{uu,m1} & \dots & S_{uu,mm} \end{bmatrix} \tag{2}$$

$$\mathbf{S_{yy}} = E[\mathbf{Y}\mathbf{Y}^H] = \begin{bmatrix} S_{yy,11} & \dots & S_{yy,1\ell} \\ \vdots & \ddots & \vdots \\ S_{yy,\ell 1} & \dots & S_{yy,\ell\ell} \end{bmatrix} \tag{3}$$

where the estimation process can be performed by means of the so-called *Welch's Averaged Periodogram*: the time series is weighted by a window to reduce leakage (e.g. a Hanning window) and the discrete Fourier transform (DFT) is applied to the weighted time series. Then, the DFT is multiplied by its complex conjugate transpose (Hermintian superscript, H). Typically, the

variance of the estimation is reduced by splitting the original time signals in overlapping segments, computing the weighted periodograms of all segments and taking the average. Because of a column vector is multiplied by a row vector, the periodogram is a rank-one estimate of the spectrum. Segment averaging increases the rank. Care must be taken that the number of averages is at least equal to the dimension of the estimated SDM [54]. Therefore, the diagonal terms of the input SDM ($\mathbf{S_{uu}} \in \mathbb{C}^{m\times m}$) and of the output SDM ($\mathbf{S_{yy}} \in \mathbb{C}^{\ell\times\ell}$), are represented by the PSDs of the input and output signals, respectively. The off-diagonal entries instead, are represented by the corresponding CSDs. Furthermore, it can be observed that both the input and output SDMs are Hermitian matrices ($S_{ij} = S'_{ji}$ for all i and j) and thus the lower triangular part of the matrix is the complex conjugate of the upper part [60].

In the hypothesis of a Linear Time-Invariant (LTI) system, the structure under test is represented by the Frequency Response Function (FRF) matrix ($\mathbf{H} \in \mathbb{C}^{\ell\times m}$), thus

$$\mathbf{Y} = \mathbf{HU} \tag{4}$$

The complex conjugate transpose of the output spectrum vector can be computed as

$$\mathbf{Y}^H = [\mathbf{HU}]^H = \mathbf{U}^H\mathbf{H}^H \tag{5}$$

Substitution into Equation (4) yields

$$\mathbf{YY}^H = \mathbf{HUU}^H\mathbf{H}^H \tag{6}$$

Therefore, taking the expected values of both sides of Equation (6) gives

$$\mathbf{S_{yy}} = \mathbf{HS_{uu}H}^H \tag{7}$$

It follows that

$$\mathbf{S_{uu}} = \mathbf{H^{-1}S_{yy}H^{-1}}^H \tag{8}$$

Equation (7) and Equation (8) are the input-to-output and the out-to-input relationships, which provide matrix solutions for general MIMO linear model problems.

It is worth noticing that for the general case in which the number of inputs and outputs is not the same ($m \neq \ell$), the FRF matrix is rectangular and the computation of its inverse ($\mathbf{H^{-1}}$) requires a pseudo-inverse approximation. The most used is the *Moore-Penrose* pseudo-inverse, which involves a Singular Value Decomposition (SVD) to provide the matrix condition number at each spectral line in the least-squares sense. The *Moore-Penrose* pseudo-inverse of the FRF matrix ($\mathbf{H}^{\dagger}$) can be derived as follows [61]

$$\begin{aligned}
&\mathbf{H} = \mathbf{T}\mathbf{S}\mathbf{V}^{\mathrm{H}} \\
&\mathbf{H}^{\mathrm{H}} = \mathbf{T}^{\mathrm{H}}\mathbf{T}\mathbf{S}\mathbf{V}^{\mathrm{H}} = \mathbf{S}\mathbf{V}^{\mathrm{H}} \\
&\mathbf{S^{-1}}\mathbf{T}^{\mathrm{H}}\mathbf{H} = \mathbf{S^{-1}}\mathbf{S}\mathbf{V}^{\mathrm{H}} = \mathbf{V}^{\mathrm{H}} \\
&\mathbf{V}\mathbf{S^{-1}}\mathbf{T}^{\mathrm{H}}\mathbf{H} = \mathbf{V}\mathbf{V}^{\mathrm{H}} = \mathbf{I} \\
&\mathbf{H}^{\dagger} = \mathbf{V}\mathbf{S^{-1}}\mathbf{T}^{\mathrm{H}}
\end{aligned} \tag{9}$$

where $\mathbf{T}$ and $\mathbf{V}$ are orthonormal and $\mathbf{S}$ is a diagonal matrix of non-negative real numbers. To compute $\mathbf{S^{-1}}$ the elements greater than the tolerance (fixed a priori) are inverted and kept, the elements less than the tolerance are replaced by zero. The SVD, first provides information on the properties of $\mathbf{H}$ at each spectral line, and second it offers solutions for addressing the noise problem by investigating the ratio of the largest to smallest singular value. The pseudo inverse of the FRF matrix ($\mathbf{H}^{\dagger}$) is often called system' *Mechanical Impedance* ($\mathbf{Z}$).

2.2 MIMO RANDOM CONTROL ALGORITHM

In vibration control testing, the MIMO model refers to input of multiple drive signals to an excitation system in a MDOF configuration, and multiple measured control outputs from the fixture or test item in a MDOF configuration. [44]. The purpose of any MIMO Random Vibration Control test is thus to reproduce certain user-defined spectra (test specifications) at specific control output locations. Therefore, the control algorithm has to generate the input SDM ($\mathbf{S_{uu}}$) to be send to the multiple shakers for replicating the user-defined reference SDM ($\mathbf{S_{yy}^{ref}}$). According to Equation (8), for MIMO control testing the output-to-input relationship can be written as

$$\mathbf{S_{uu}} = \hat{\mathbf{Z}}\mathbf{S_{yy}^{ref}}\hat{\mathbf{Z}}^{\mathrm{H}} \tag{10}$$

where $\hat{\mathbf{Z}}$ is the (pseudo) inverse of the FRFs matrix (Equation 9) estimated during the *System Identification* (Sys. Id.) pre-test phase. Typically, $\hat{\mathbf{H}}$ is estimated via H1 estimator [62] by performing a low level random pre-test with decorrelated drives

$$\hat{\mathbf{H}} = \hat{\mathbf{S}}_{\mathbf{yu}}\hat{\mathbf{S}}_{\mathbf{uu}}^{\dagger} \implies \hat{\mathbf{H}}^{\dagger} = \hat{\mathbf{Z}} \tag{11}$$

As a results of the inverse control problem, the reference SDM could be theoretically achieved by sending to the multiple shakers the drives signals that return the computed input SDM

$$\mathbf{u}(t) = \text{ifft}(\mathbf{U}) : \mathbf{S}_{\mathbf{uu}} = E[\mathbf{U}\mathbf{U}^{H}] = \hat{\mathbf{Z}}\mathbf{S}_{\mathbf{yy}}^{\mathbf{ref}}\hat{\mathbf{Z}}^{H} \tag{12}$$

Nevertheless, due to the possible non-linear behaviour of the unit under test and noise in the measurements, the system estimated in the pre-test phase will inevitably differ from the actual one ($\mathbf{H}\hat{\mathbf{Z}} \neq \mathbf{I}$)

$$\mathbf{S}_{\mathbf{yy}} = (\mathbf{H}\hat{\mathbf{Z}})\mathbf{S}_{\mathbf{yy}}^{\mathbf{ref}}(\mathbf{H}\hat{\mathbf{Z}})^{H} \neq \mathbf{S}_{\mathbf{yy}}^{\mathbf{ref}} \tag{13}$$

and a control action is needed to reduce the error

$$\mathbf{E} = \mathbf{S}_{\mathbf{yy}}^{\mathbf{ref}} - \mathbf{S}_{\mathbf{yy}} \tag{14}$$

Nowadays the various MIMO control system vendors do not always approach control in the same manner and some innovative random vibration control strategies have been proposed by few authors [63][46]. Moreover, it is not the intent of this thesis to provide the specifics of the control algorithms used in the conduct of multi-axis tests. However there are some basic concepts, keys to MIMO control problems, that will be addressed in the following.

The basic outlines of the MIMO random control algorithm are simplified in the flowchart of Figure 2. As introduced above, during control testing the presence of non-linearities and noise makes impossible the use of the theoretically computed input drives signals (Equation 12). To overcome this problem, the so called *Cholesky Factorisation* is applied directly to the reference SDM. The *Cholesky Factorisation* decomposes a positive (semi)definite matrix in a lower triangular matrix times its complex conjugate transpose

$$\mathbf{S}_{\mathbf{yy}}^{\mathbf{ref}} = \mathbf{L}\mathbf{L}^{H} \tag{15}$$

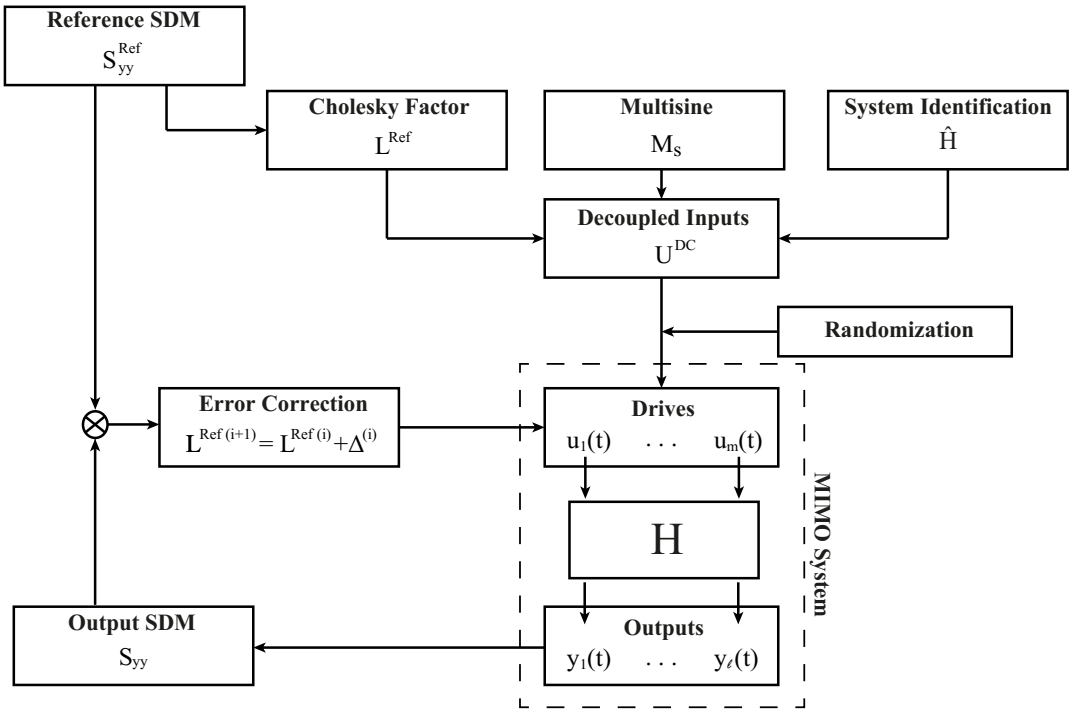

Figure 2: Flow chart of the MIMO Random Vibration Control algorithm

Exploting the output-to-inut control relationship of Equation (10) and the *Cholesky Factorisation* of Equation (15), it has been demonstrated [63] that the so called *Decoupled Inputs* can be computed as

$$\mathbf{U^{DC}} = \hat{\mathbf{Z}}\mathbf{L}^{\mathrm{ref}}\mathbf{M_s} \tag{16}$$

where $\hat{\mathbf{Z}} \in \mathbb{C}^{\ell \times m}$ is the estimated machanical impedance; $\mathbf{L}^{\mathrm{ref}} \in \mathbb{C}^{\ell \times \ell}$ is the Cholesky factor of the reference SDM, that is a lower triangular complex matrix whit real and non-negative diagonal elements; $\mathbf{M_s} \in \mathbb{C}^{\ell \times 1}$ is the *Multisine Matrix*, which represents the Fourier transform of a vector of ℓ independent white noise sequences. Actually, these sequences are just an approximation of white noise, and they are called *pseudo-random* signals, i.e. multisine signals where the sine components have unit amplitude and random phase.

The decoupled input signals are converted in time domain by applying the inverse DFT. The matrix formulation of the problem makes the application of

the *Time-Domain Randomisation* possible. The randomisation procedure converts the line spectrum from the pseudo-random signals to a true continuous spectrum and it ensures a continuous input data stream to the shaker, without having to carry out intensive matrix computations [53]. To meet these requirements, the time-domain randomisation procedure outlined by Smallwood in [63] is used. After the randomisation, the input drive signals ($\mathbf{u}(t)$) can finally be sent to the shakers and the resulting output signals ($\mathbf{y}(t)$) can be recorded. Once the output SDM ($\mathbf{S_{yy}}$) is estimated, the *Error Correction* (Δ) is computed. The error is calculeted on the lower triangular matrix ($\mathbf{L}$) based on the difference between the Reference SDM ($\mathbf{S_{yy}^{ref}}$) and the measured output SDM ($\mathbf{S_{yy}}$). The complexity of building these systems, e.g. designing the control system and specifying the test parameters, increases much faster than the rate of increase in the number of actuators. To a first order, the control complexity increases by at least the square of the number of actuators that are used [33].

Finally, it is important to emphasise the critical role of the *System Identification* to the success of any MIMO vibration control test. The estimation of the FRFs matrix ($\mathbf{\hat{H}}$) is strictly required to generate the decoupled inputs of Eqaution 16. However, as already explained above, the estimation process may introduce some inaccuracies at certain frequencies. Typically, these problematic frequencies correspond to structural anti-resonances, that is frequencies at which the system under test responds inefficiently to the excitation energy, due to the low-response behaviour. When the estimated magnitude of some elements of the FRFs matrix are too small, some columns or rows of the matrix become linearly dependent and near-singularities or singularities will occur. These problematic frequencies are the spectral lines where the feedback control actions will contain the most error and the system will be over or under testing [33]. To narrow these problems, the System Identification is done by exciting all the actuators simultaneously with band-limited Gaussian noise. The drive signals are typically flat spectrally and band limited to the maximum frequency of interest. In addition, the drive signals are also uncorrelated among themselves. The response levels for the system characterization should be chosen as high above the noise floor as possible in order to maximize the accuracy of the impedance estimate, but still ensure that the test article does not experience vibration levels above some operator chosen level, in order to not excessively stress the test specimen. In conclusion, an accurate test-design (e.g. the design configuration of the actuation systems, the test fixture subsystems

and the setup of the control point location) is critical to proper perform the System Identification and to avoid subsequent control problems which can compromise the validity of the MIMO control test.

2.3 MATHEMATICAL PROPERTIES OF THE REFERENCE SDM

As shown in the block-diagram of Figure 2, the definition of the control target is the starting-point of any MIMO control algorithm. Equations (3) gives an example of the basic outline which the reference SDM should have. It can be noted that both PSDs and CSDs, e.i. the diagonal and the off-diagonal terms of the reference matrix, are required test parameters. In particular, the PSDs are usually known quantities for the environmental test engineer, representing the test specifications. The CSDs instead, are often unknown quantities and they have to be calculated.

The reference CSDs can be computed starting from the respective reference PSDs and specifying coherence and phase profiles as functions of frequency. For instance, the reference CSD between the *i*-th and the *j*-th control output can be computed as [59]

$$S_{ij}^{ref} = \left|S_{ij}^{ref}\right| e^{i\phi_{ij}} = \sqrt{\gamma_{ij}^2 S_{ii}^{ref} S_{jj}^{ref}}\, e^{i\phi_{ij}} \tag{17}$$

where γ_{ij}^2 and ϕ_{ij} are the coherence and the phase angle between the two reference outputs, respectively. It is worth to underline that, for computation reason linked to the control process stability, coherence values of 0 and 1 are usually avoided. Typical values of low coherence and high coherence are $0.05 \div 0.08$ and $0.95 \div 0.98$, respectively.

As a result, in case of MIMO configuration the control target definition could be very challenging. As documented above infact, all the error correction strategies exploited in MIMO random control testing (mainly due to works of Underwood [46],[33], Smallwood [45] and Peeters [54]) rely on the possibility of apply the *Cholesky Factorisation* to one of the spectral matrices (either $\mathbf{S}_{\mathbf{yy}}^{ref}$ or $\mathbf{S}_{\mathbf{uu}}$) and then iteratively correct the resultant Cholesky factor. This operation is acceptable only if the reference SDM is a positive (semi)definite matrix.

Consequently, one of the most important aspects on defining the reference SDM is that it must result a positive (semi)definite matrix. This fundamental algebraic constraint, first of all it guarantees the physical meaning of the reference and secondly it leads to a realisable target for the control algorithm.

It can be demonstrated that all the Spectral Density Matrices in multi-axial random control are positive (semi)definite. By definition, a matrix $\mathbf{S}$ is positive (semi)definite if and only if the scalar $\mathbf{z}^H\mathbf{S}\mathbf{z}$ is (semi)positive for every non-zero column vector $\mathbf{z}$ of (generally complex) numbers. In random vibration control, the drives and the control signals are random signal (stationary and ergodic). Therefore, in accordance with Equation (3), for the random recordings $\mathbf{y}(t)$

$$\mathbf{S_{yy}} = E[\mathbf{Y}\mathbf{Y}^H] = \lim_{N\to\infty}\left[\frac{1}{N}\sum_{ii=1}^{N}(Y_{ii}Y'_{ii})\right] \tag{18}$$

where $\mathbf{Y}$ is the spectrum of the random recordings. By noticing that $\mathbf{Y}\mathbf{Y}^H = \mathbf{Y}\mathbf{I_d}\mathbf{Y}^H$ and following the definition of positive (semi)definite matrices, it may be said that the rank-1 matrix $[\mathbf{Y}\mathbf{Y}^H]$ is positive (semi)definite. Since the space of positive (semi)definite matrices is convex, a summation of positive (semi)definite matrices is still positive (semi)definite. This is also true in case of scaling for a real positive number $(1/N)$. Therefore, the averaging process of Equation (18) preserves the positive (semi)definiteness of the matrix $[\mathbf{Y}\mathbf{Y}^H]$ and, thus, $\mathbf{S_{yy}}$ is positive (semi)definite. As a consequence, also the user-defined reference SDM ($\mathbf{S}^{ref}_{\mathbf{yy}}$) must be positive (semi)definite in order to be physically realizable and controllable.

There are some properties that have practical implication in multi-axial random vibration control. Considering the general set of signals $\mathbf{y}(t)$, saying that the corresponding SDM ($\mathbf{S_{yy}}$) is positive (semi)definite also means (necessary and sufficient conditions) that:

(a) all the eigenvalues of $\mathbf{S_{yy}}$ are (semi)positive;

(b) $\mathbf{S_{yy}}$ has a unique Cholesky Decomposition, meaning that it can be decomposed in the product of two triangular hermitian matrices, referred as the *Cholesky factors*: $\mathbf{S_{yy}} = \mathbf{L}\mathbf{L}^H$;

(c) the *Sylvester's Criterion* is respected, i.e. all the *Principal Minors* of $\mathbf{S_{yy}}$ have positive determinants. The Principal Minors are the square sub-matrices that share the diagonal with the full matrix and the first element.

Moreover, if $\mathbf{S_{yy}}$ is positive semi-definite then:

(d) the trace of $\mathbf{S_{yy}}$ is real and (semi)positive, being the matrix trace the sum of its eigenvalues;

(e) follows from (a) or (c) that the determinant of $\mathbf{S_{yy}}$ is real and (semi)positive;

(f) also $\mathbf{S_{uu}} = \mathbf{Z}\mathbf{S_{yy}}\mathbf{Z}^{H}$ is positive (semi)definite.

The property (b) is fundamental and allows the control algorithm to work on the Cholesky Decomposition of the target matrix (the approach proposed by Smallwood in [45] and [28], and previously described in Section 2.2) or, following the property (f), of the drives matrix (as proposed by Underwood in [33]). Property (d) underlines that the method chosen for defining the MIMO control target needs to guarantee that the trace of the reference matrix (and following property (f), of the drives matrix) needs to be positive.

3

EXPERIMENTAL ASSESSMENT OF RANDOM VIBRATION CONTROL STRATEGIES: SISO VS MIMO

3.1 INTRODUCTION

Random vibration control tests are conducted in the laboratory to simulate with high degree of accuracy the vibration environment that a specimen has to withstand during its life cycle. For decades, single axis shakers have been the only available excitation systems. Therefore, in order to recreate in the laboratory the multi-directional nature of a real vibration environment, the sequential single axis random vibration control testing has been established as a standard method. In such tests, the test specimen is sequentially rotated along three orthogonal axes and excited in one direction at a time by exploiting a single axis shaker. The SISO control strategy is the simplest technique for carrying out these types of tests: the control algorithm tunes the input voltages to the shaker (Single-Input) in order to excite the specimen with the required PSD profile (Single-Output). However, the methodologies for performing random vibration control tests are constantly evolving thank to the enormous advances in control technologies. Over recent years, the avant-garde test facilities have the capability to address simultaneous multi-axial vibration testing by exploiting MIMO control techniques. Unfortunately, most of the current industrial practice is strongly relying on SISO control that still remains the nowadays standard technique for qualification and durability testing.

The purpose of this chapter is to reveal one of the possible inconvenient related to the use of SISO control strategy when performing single axis random vibration testing. With the SISO control strategy, only the PSD profile on the drive axis of vibration is feedback controlled, while the vibration levels along

Figure 3: Three DoF shaker table at the University of Ferrara: Dongling 3ES-10-HF-500.

the two axes orthogonal to the main axis (called *cross axes* or *off axes*) can only be measured. Nevertheless, the presence of uncontrollable cross axis vibrations could compromise the validity of the single axis test. In some cases, the coupling between the excitation system and the test specimen can cause cross axis excitations that alter the dynamic behaviour of the test specimen by inducing different stress state and unexpected failure modes. In accordance with Standard practice [4], if the amplitude of the cross axis PSD is more than 0.2 times the amplitude of the required PSD on the drive axis of vibration, the single axis test should be deemed as invalid. In order to overcome the SISO control limitations, the use of more advanced MIMO control strategies could be an effective option. The MIMO control configuration guarantees to accurately replicate the required PSD profile on the main axis of vibration and to simultaneously control the cross axis vibration levels below the acceptable thresholds. However, the MIMO control target must be correctly defined in

order to fully exploit the benefits of the MIMO configuration, otherwise the risk is to use more expensive and complicated test equipments without improving the final results. In this context, the original contribution of this work is also to provide a detailed analysis surrounded by practical examples about the definition of the MIMO control target to be used in single axis vibration testing.

Therefore, the experimental assessment proposed in this chapter critically compares the use of SISO and MIMO control strategies for performing sequential single axis random vibration control tests. In particular, the study focuses on the different approach of the two control techniques to tackle the cross axis vibration problem. A test campaign has been carried out using two different test facilities with the same performance characteristics: a single axis shaker and the three DoF (Degree of Freedom) shaker table at the University of Ferrara. The details of the test equipments are provided in Section 3.2. Moreover, Section 3.3 offers the critical study and the practical examples on the MIMO control target definition. Section 3.4 shows the test case where SISO and MIMO control techniques are experimentally compared. Finally, Section 3.5 closes the chapter providing the concluding remarks of the activity.

3.2 TEST FACILITY DESCRIPTION

3.2.1 *Three DoF shaker table*

In 2017 the MechVib, Mechanics and Vibration Research Group, of the University of Ferrara purchased the Dongling 3ES-10-HF-500 (Figure 3). This avant-garde excitation system is a 3-DoF shaker table capable of exciting test specimens in three directions simultaneously. The innovative characteristic of the system is the Orthogonal Coupling Bearings Unit (*OCBU*) which connects the three independent electro-dynamic shakers of 10 kN each. The *OCBU* (Figure 4) is a cutting-edge technology, patented by Dongling, which provides reliable motion of the slide table in the three orthogonal directions. A dedicated refrigerating hydraulic system pumps high-pressure oil inside the bearings unit. The oil film that wets the bearing surfaces has enough stiffness and durability to avoid the metal-to-metal contact. Moreover, an optimized throttle hole distribution ensures the transmit force. The excitation system is equipped with a smart power amplifier system. The smart technology uses three power units working in parallel and it guarantees the stability and reliability of the

Figure 4: Orthogonal Coupling Bearings Unit (OCBU) exploited by the 3 DoF shaker table to excite test specimens in three orthogonal directions simultaneously. Patent-protected by *Dongling Technology*

system. The shakers are air-cooled, and they cover a wide frequency range (up to 2 kHz). The shaker head expander is a magnesium alloy table of 14 kg. It is designed to be as light as possible but stiff in the useful frequency range. The maximum payload is 100 kg. By exploiting the *SIEMENS* vibration control technologies (data acquisition hardware and vibration control software), it is possible to perform vibration control testing in frequency domain (sine and random) and in time domain (time waveform replication). This advanced excitation system is suitable for the dynamic characterisation of test specimens,

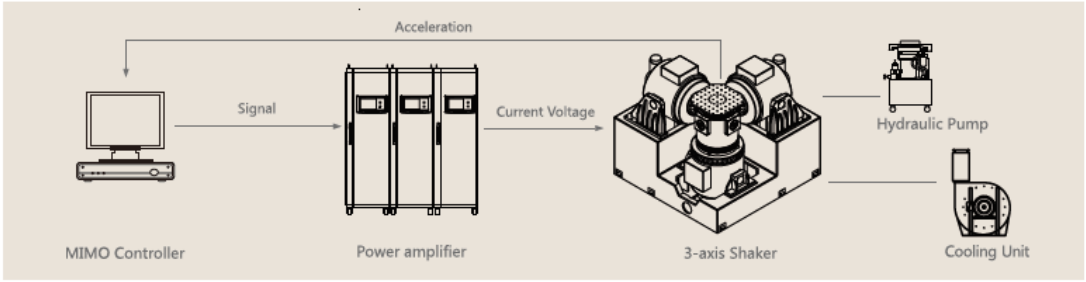

Figure 5: Schematic representation of the 3-DoF shaker table test facility.

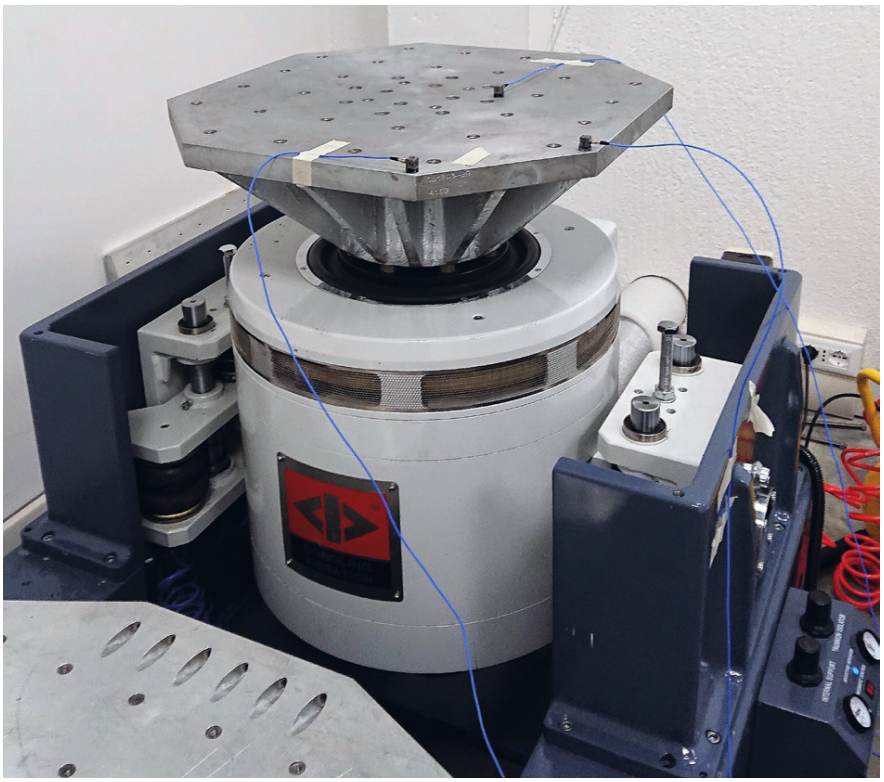

Figure 6: Single axis shaker at G.S.D. Srl of Pisa: Dongling ES-10-240.

as well as, for the replication of the vibration environment in vibration control testing. A schematic representation of the entire test facility is shown in Figure 5. Table 1 summaries the main performance characteristics of the 3-DoF shaker table.

3.2.2 *Single axis shaker table*

The Dongling ES-10-240, shown in Figure 6, is a single axis shaker of 10 kN rated force. It is electro-dynamic and air-cooled. As amplifier system, the shaker uses the same smart technology described in the previous section for the 3-DoF excitation system. The useful frequency range is up to 2 kHz (first system resonance is 2400 $\pm$ 5% Hz). The maximum payload is 300 kg, that is higher than the one supportable by 3-DoF shaker table thanks to the extra stability deriving from the lack of the *OCBU*. For the same reason, other

Table 1: Performance characteristics of the Donling 3-DoF shaker table (3ES-10-HF-500) and of the Dongling single axis shaker (ES-10-240).

	3ES-10-HF-500	ES-10-240
Rated Force	10 kN	10 kN
Max Payload	100 kg	300 kg
Max Displ. (p-p)	38 mm	51 mm
Max Velocity	1.2 m/s^2	2 m/s^2
Freq. Range	$3 \div 2000$ Hz	$3 \div 2000$ Hz

performances such as the maximum displacement and the maximum velocity are slightly higher with respect to the 3-DoF shaker table. Table 1 compares the main performance characteristics of the excitation systems. The Dongling ES-10-240, as all the Dongling' shakers, is compatible with *SIEMENS* technologies and therefore it can be driven by means of *Simcenter Testlab* and *SCADAS* controller. The Dongling ES-10-240 is installed at the G.S.D. Srl of Pisa (Italy). GSD has been operating in the field of Applied Electromagnetics since 1995. The company performs electromagnetic compatibility testing on electrical and electronic equipment for industrial use. The single axis shaker is exploited for qualification and durability tests in order to provide to the customer the CE mark and certification in accordance with the International Standards requirements.

3.3 DEFINING THE MIMO CONTROL TARGET

3.3.1 *Practical examples*

The definition of the control target is the first step for carrying out any random vibration control test. In SISO control configuration, this procedure results to be easy and direct. The control target is just the PSD profile that needs to be reproduced at the single output location. Nevertheless, the control target definition could be more challenging in case of MIMO control configuration. As explained in Chapter 2, when multiple outputs need to be controlled simultaneously, besides the vibration levels for each control output, the cross-

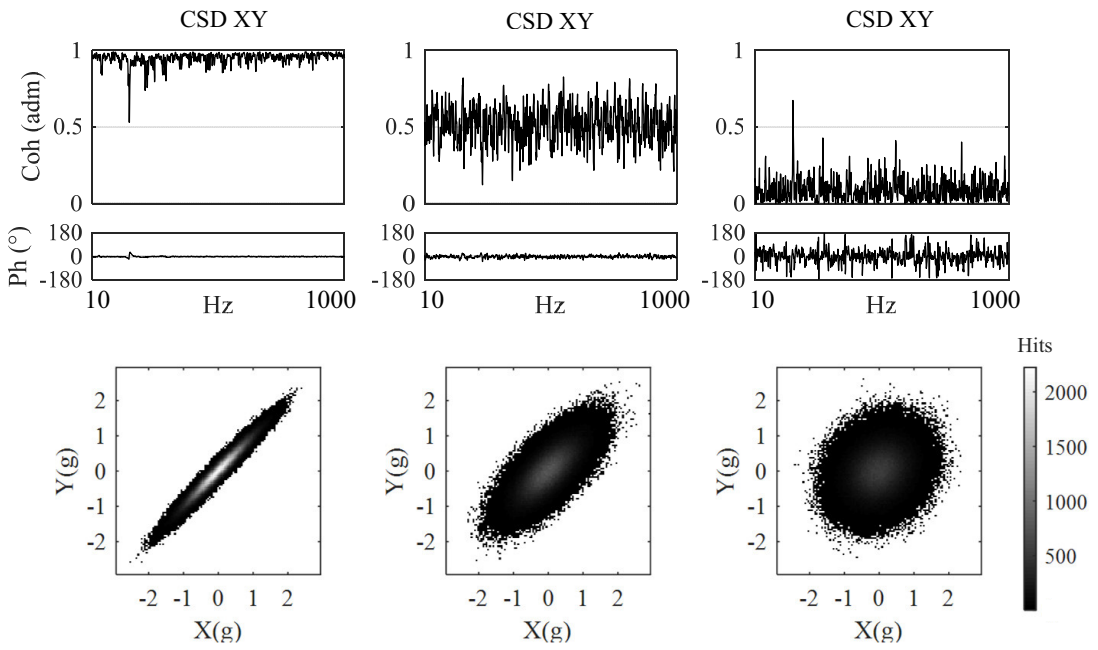

Figure 7: Coherence role for two (in phase) control outputs: $\gamma^2_{XY} = 0.98$ (left), $\gamma^2_{XY} = 0.5$ (middle) and $\gamma^2_{XY} = 0.05$ (right).

correlation between each pair of the outputs has to be defined. The definition of the reference CSDs is important as much as the definition of the reference PSDs. Setting different profiles of phase and coherence for the reference CSDs means to change the way of combining the test specifications along the control output directions. As a consequence, the test specimen could be excited in completely different manners even imposing the same reference PSD.

Figure 7 gives a practical example for a two-inputs two-outputs control case. The same flat PSD profile (0.56 g_{RMS} in the frequency range [10-1000] Hz) is considered as test specification along the two control directions X and Y. The figure shows three different ways of combining the two reference PSDs: the values of coherence and phase of reference CSD_{XY} are represented in the top of the figure; the bivariate histogram plots of the recorded acceleration signals along X and Y are depicted in the bottom of the figure, with the color bar that shows the relative number of hits. In particular, the figure highlights the effects of the coherence variation from high coherence ($\gamma^2_{XY} = 0.98$) to low coherence ($\gamma^2_{XY} = 0.05$) for in phase control outputs ($\phi_{XY} = 0^o$).

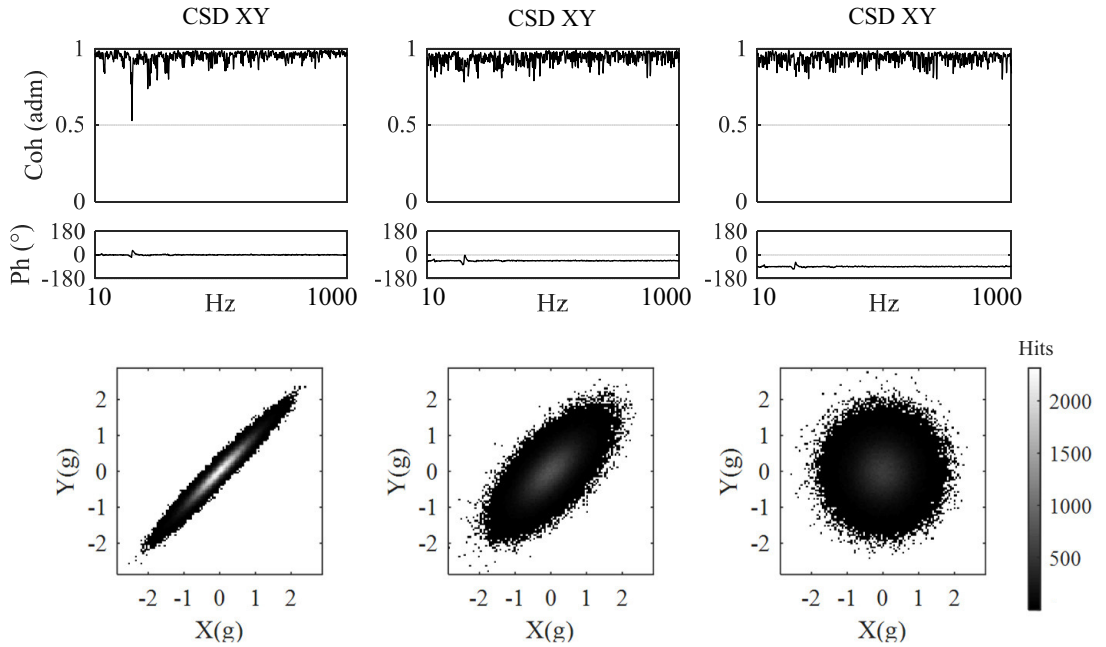

Figure 8: Phase role for two (fully coherent) control outputs: $\phi^2_{XY} = 0^o$ (left), $\phi^2_{XY} = 45^o$ (middle) and $\phi^2_{XY} = 90^o$ (right).

It can be noted that, in case of fully coherent (in phase) control outputs, the data distribution is perfectly oriented toward the bisector of the two control directions. This combination is practically identical to a single output test 45° inclined. Moreover, the more the coherence is low, the more the phase value loses in relevance: the data dispersion increases around the bisector until reaching a circle data distribution (uncorrelated control outputs). However, Figure 8 shows that it can be possible to obtain similar results by keeping fully coherent control outputs ($\gamma^2_{XY} = 0.98$) and playing with the phase values. The data distribution moves from an elliptical to a circular shape by simply setting 45° and 90° out of phase fully coherent control outputs.

The previously described examples underline how the choice of phase and coherence profiles could be decisive in order to properly combine the test specifications and to correctly excite the test specimen. Due to the key role for any successful MIMO control test, the definition of the MIMO control target is still being investigated in numerous publications as underlined in the introduction of this thesis (Chapter 1) .

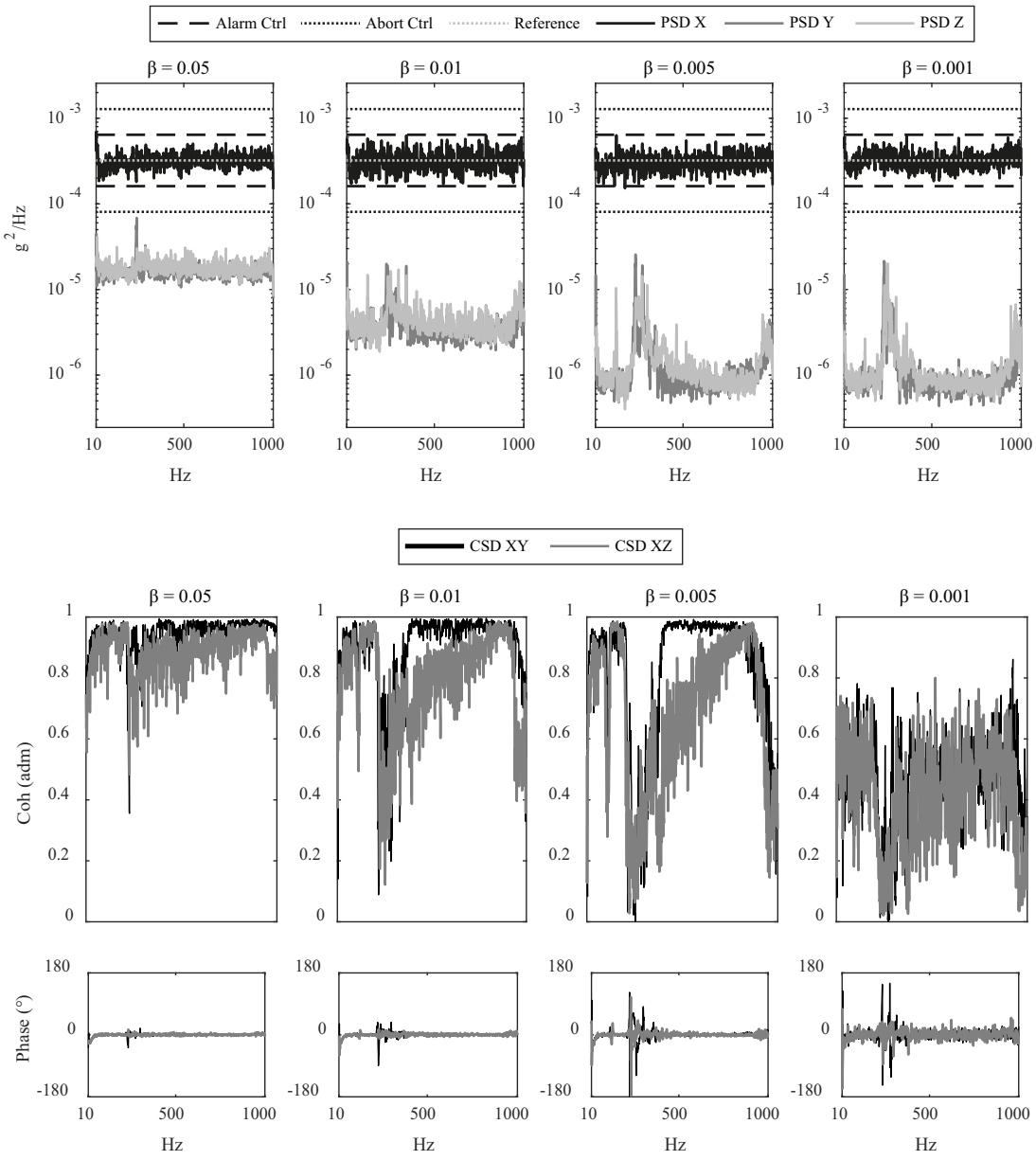

Figure 9: Effects of the scale factor β used for defining the cross axis reference PSDs: measured PSDs in the three control outputs (top); coherence and phase values of the two measured CSDs (bottom).

3.3.2 *Experimental approach for single axis random vibration testing*

This paragraph describes through a series of experimental cases how to define the MIMO control target for performing a true single axis vibration test. The 3-DoF shaker table at the University of Ferrara, described in Section 3.2.1 and shown in Figure 3, is used as excitation system. The Simcenter SCADAS Mobile SCM202V (V8 input and DAC4 output modules) is used as data acquisition system and Simcenter Testlab as vibration control software.

The following test case takes advantage of the MIMO control strategy in order to feedback control the main axis of vibration and to simultaneously force the cross axis levels below the acceptable thresholds. Therefore, a three-outputs control configuration is at least required, i.e. one control output for each of the three orthogonal directions. Typically, the only available test specification corresponds to the PSD profile that needs to be replicated on the main axis of vibration. In order to complete the control target, the user has to specify the PSD profiles of the two cross axes and to define the coherence and phase values for combining the three reference PSDs. Following the previously described examples of Figure 7 and Figure 8, a straight line movement is generated by in phase and fully coherent control outputs. Therefore, in order to perform a true single axis vibration test, it is necessary to set zero phase and high coherence for all the reference CSDs and to rescale down the reference cross axis PSDs as

$$PSD_{Cross}(f) = \beta * PSD_{Main}(f) \tag{19}$$

where β is the scale factor that guarantees a data distribution perfectly oriented along the main axis of vibration. The test case explains the effects of imposing different values of β for the definition of the cross axis reference PSDs. The control accelerometer is fixed on the bare head expander of the shaker. A flat PSD profile of 0.56 g_{RMS} in the frequency range [10-1000] Hz is the test specification along the main axis of vibration (axis X). Directions Y and Z correspond to cross axes. The orientation of the frame of reference is shown in red in Figure 3.

Figure 9 shows the control results obtained with four different scale factors β. In particular, the PSDs measured along axes X, Y and Z are depicted in the top of the figure, i.e. the black, grey and light grey curves respectively. For the main axis of vibration, the dashed-black lines and the dotted-black lines are the alarm and abort control limits fixed at $\pm$3dB and $\pm$6dB from the reference

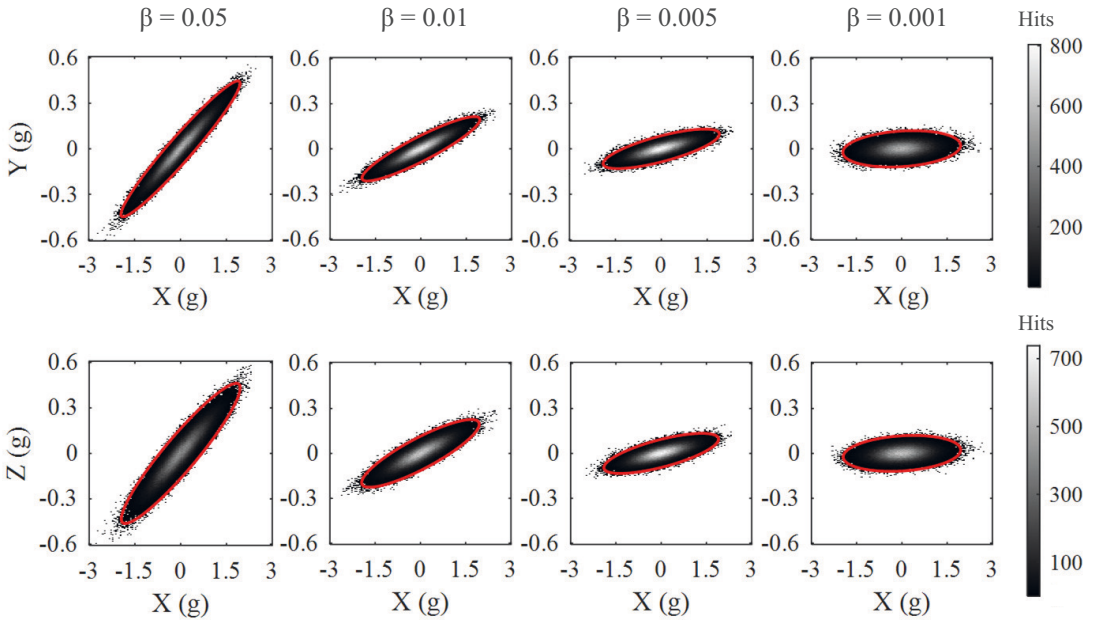

Figure 10: Effects of the scale factor β used for defining the cross axis reference PSDs: bivariate histogram plots between the measured acceleration signals along main axis X and cross axis Y (top); main axis X and cross axis Z (bottom).

(dotted-grey line). The bottom of the figure shows the coherence and the phase values deriving from the combination of the three control outputs. Figure 9 emphasizes some remarkable results. There is a physical control limit below which the cross axis PSDs cannot be further lowered, even imposing lower scale factors. Moreover, the lower the scale factor β, the higher the deviation from the in phase and fully coherent outputs scenario. As a consequence, going beyond the physical control limit by setting too low scale factors does not lead to any gain in terms of cross axis PSD reduction, rather it worsens the quality of the single axis vibration test. The bivariate histogram plots between the acceleration signals, shown in Figure 10, confirm the previous results. The color bar shows the relative number of hits and the red line is the 3σ confidence ellipse, the region that contains the 99.7% of all samples. The case of $\beta = 0.001$ has the same cross axis acceleration levels with respect to the case of $\beta = 0.05$, but a more spread data distribution due to lower coherence values between the control outputs.

Unfortunately, the a priori knowledge of the best scale factor β to be used for defining the cross axis reference PSDs is practically impossible. It strongly depends on the specific interactions between excitation system and test specimen, combined with the controller capabilities to perform the actual test. The proper scale factor can significantly vary from case to case. Therefore, some preliminary tests could be useful in order to set the scale factor β and to properly define the MIMO control target for the actual test.

3.4 TEST CASE: SEQUENTIAL SINGLE AXIS RANDOM VIBRATION CONTROL

3.4.1 *Experimental setup*

To compare and to point out the different capabilities of SISO and MIMO control strategies, the same series of tests has been carried out using the two test facilities: the single axis shaker Dongling ES-10-240 at G.S.D. srl of Pisa and the 3-DoF shaker table Dongling 3ES-10-HF-500 at the University of Ferrara, described in Section 3.2 and shown in Figure 6 and Figure 3 respectively. As previously explained, the vibration test systems are provided by the same supplier (*Dongling Technologies*) and both are electrodynamic and air cooled shakers of 10 kN rated force. The use of excitation systems with similar performance characteristics should exclude potential sources of uncertainty in the obtained results and it guarantees the most comparable possible analysis.

The same sequential single axis vibration test has been carried out in three different combinations of excitation system and vibration control technology:

Combination I) single axis shaker with SISO control strategy

Combination II) 3-DoF shaker table with SISO control strategy

Combination III) 3-DoF shaker table with MIMO control strategy

It is worth to notice that for Combination II), the 3-DoF shaker table can be used as single-input excitation system by shutting down the power supply of two shakers.

The test specimen is an Exhaust Gas Recirculation (EGR) valve, an automotive component used to reduce the emissions in internal combustion engines. The sequential single axis vibration test is performed by exploiting a specifically designed fixture that allows the sequential rotation of the EGR valve in

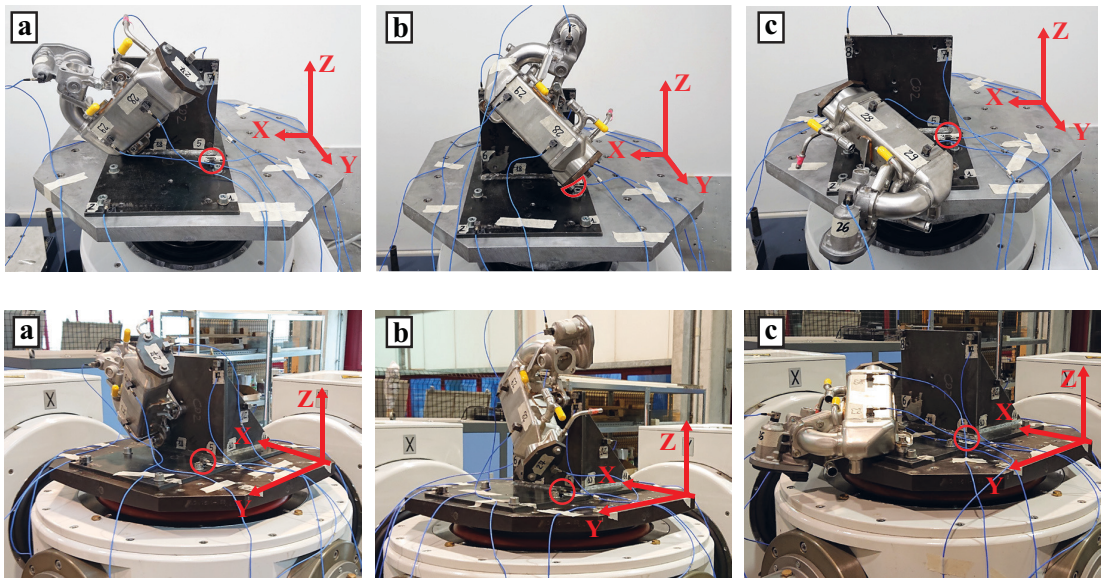

Figure 11: Test configurations for sequential single axis vibration test with the single axis shaker (top) and with the 3-DoF shaker (bottom): a) transversal test configuration; b) longitudinal test configuration; c) vertical test configuration. The red circle highlights the control accelerometer location.

three test configurations: transversal configuration, longitudinal configuration and vertical configuration, shown in Figure 11 a), b) and c) respectively. For all the test configurations, axis Z is the main axis of vibration where the single axis test specification should be replicated. Therefore, axes X and Y correspond to the cross axes of vibration that are feedback controlled only with MIMO control configuration by using the 3-DoF shaker table, i.e. Combination III). The three-axial control accelerometer is mounted on the fixture at the head expander mounting point (highlighted with a red circle in Figure 11). Additional 13 three-axial accelerometers are mounted on the system as measurement points: 4 on the EGR valve and 9 on the fixture. All the sensors are ICP (Integrated Circuit Piezoelectric) triaxial accelerometers by *PCB Piezotronics* (model: 356B21) with a resolution of 0.004 g (rms) in the bandwidth [1-10000] Hz and a sensitivity of 10 mV/g (±10%).

The single axis test specifications come from field measured data after being averaged, smoothed and enveloped for representing the operational vibration environment of the EGR valve. Table 2 summarizes the breakpoints of the

Table 2: Breakpoints of the reference PSDs used in the main axis of vibration for the three sequential test configurations (Transversal, Longitudinal and Vertical)

PSD_{TRANS}		PSD_{LONG}		PSD_{VERT}	
Hz	$g^2/Hz(e^{-3})$	Hz	$g^2/Hz(e^{-3})$	Hz	$g^2/Hz(e^{-3})$
10	0.88	10	0.23	10	0.008
40	2.2	35	0.56	25	0.008
120	2.2	105	0.56	30	0.43
125	1.2	110	0.49	110	0.43
190	0.27	175	0.35	115	0.22
195	0.56	180	0.97	175	0.22
235	0.56	260	0.97	180	1.4
240	0.87	265	0.56	260	1.4
320	0.87	275	0.56	270	0.37
325	0.56	280	0.97	310	0.37
345	0.46	360	0.97	330	0.88
350	3.0	365	0.70	410	0.88
430	3.0	390	0.70	420	0.43
435	1.8	395	1.1	450	0.43
450	1.6	450	1.1		
0.817 g_{RMS}		0.577 g_{RMS}		0.535 g_{RMS}	

reference PSDs to be replicated in the main axis of vibration for the three sequential test configurations.

The Siemens SCADAS Mobile SCM202V (V8 input and DAC_4 output modules) is used as data acquisition system and Simcenter Testlab as vibration control software.

3.4.2 *Test results and discussion*

Figure 12 shows the control point results for the sequential single axis vibration test carried out in the three previously described control test combinations

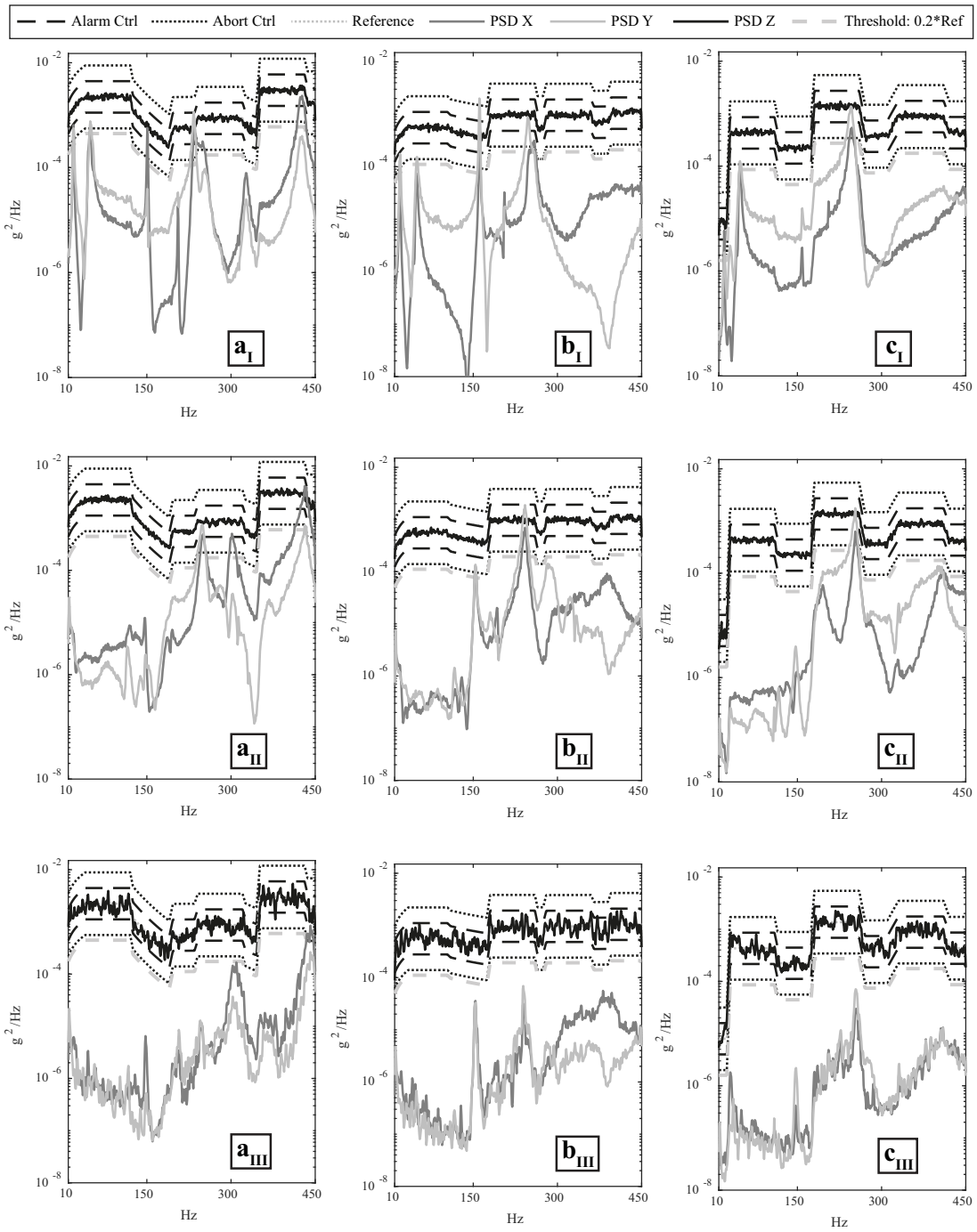

Figure 12: Control point results for sequential single axis vibration test: a) transversal test configuration; b) longitudinal test configuration; c) vertical test configuration. Subscript: I) single axis shaker - SISO control; II) 3-DoF shaker table - SISO control; III) 3-DoF shaker table - MIMO control.

Table 3: Values describing the cross axes behaviour during sequential single axis vibration test: N_{OVER} is the number of spectral lines in which the cross axis PSD exceeded the acceptable threshold. Δ_{MAX} provides the maximum difference between the cross axis PSD and the threshold PSD.

		Combination I	
		N_{OVER}	Δ_{MAX}
Transversal conf.	X (cross)	63(11.2%)	7.4 dB @ 235 Hz
	Y (cross)	23(4.0%)	10.1 dB @ 234 Hz
Longitudinal conf.	X (cross)	21(3.7%)	8.9 dB @ 162 Hz
	Y (cross)	34(6.0%)	14.3 dB @ 161 Hz
Vertical conf.	X (cross)	17(3.0%)	5.7 dB @ 20 Hz
	Y (cross)	31(5.5%)	7.0 dB @ 245 Hz

		Combination II	
		N_{OVER}	Δ_{MAX}
Transversal conf.	X (cross)	79 (14.0%)	9.7 dB @ 434 Hz
	Y (cross)	29 (5.1%)	6.3 dB @ 248 Hz
Longitudinal conf.	X (cross)	18 (3.2%)	5.6 dB @ 242 Hz
	Y (cross)	30 (5.3%)	9.9 dB @ 242 Hz
Vertical conf.	X (cross)	9 (1.6%)	3.6 dB @ 253 Hz
	Y (cross)	23 (4.0%)	8.1 dB @ 253 Hz

		Combination III	
		N_{OVER}	Δ_{MAX}
Transversal conf.	X (cross)	6 (1.1%)	1.9 dB @ 441 Hz
	Y (cross)	0	/
Longitudinal conf.	X (cross)	0	/
	Y (cross)	0	/
Vertical conf.	X (cross)	0	/
	Y (cross)	0	/

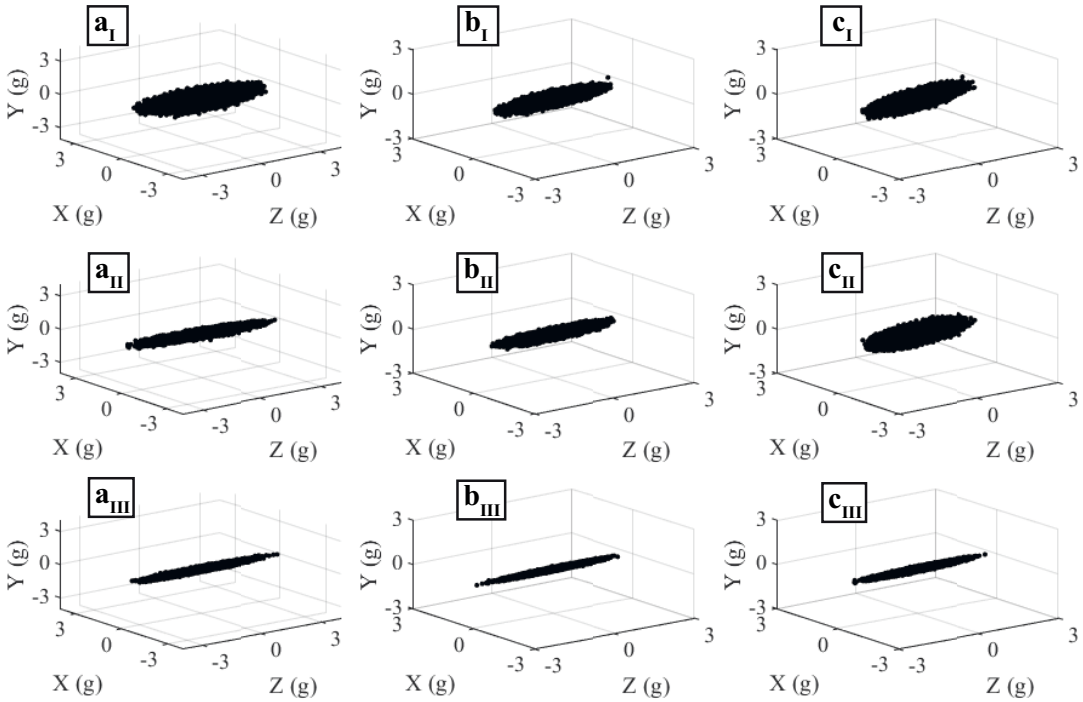

Figure 13: Three-dimensional scatter plots between the control point acceleration signals: a) transversal test configuration; b) longitudinal test configuration; c) vertical test configuration. Subscript: I) single axis shaker - SISO control; II) 3-DoF shaker table - SISO control; III) 3-DoF shaker table - MIMO control.

(Combinations I, II and III). For the main axis of vibration (axis Z), the black curves are the measured PSDs, the dashed-black lines and the dotted-black lines are the alarm and the abort control limits fixed at $\pm$3dB and $\pm$6dB from the references (dotted-grey lines). The grey and light-grey curves are the measured PSDs along cross axes X and Y, respectively. The dashed-grey lines represent the acceptable thresholds for the cross axis vibration levels (0.2 times the reference PSDs on the main axis of vibration [4]). Figure 12 highlights the limitations of SISO control strategy to perform a true single axis vibration test. In both Combinations I and II, although the test specification along the main axis of vibration is perfectly replicated, at some frequencies the cross axis PSDs exceed the acceptable threshold (in some cases they even

Table 4: Values gRMS of the recorded control signals during sequential single axis vibration test; Combination I) single axis shaker - SISO control; Combination II) 3-DoF shaker table - SISO control; Combination III) 3-DoF shaker table - MIMO control.

		Combination I	Combination II	Combination III
Trans. Conf.	X (cross)	0.225 g_{RMS}	0.281 g_{RMS}	0.122 g_{RMS}
	Y (cross)	0.156 g_{RMS}	0.153 g_{RMS}	0.068 g_{RMS}
	Z (main)	0.818 g_{RMS}	0.823 g_{RMS}	0.804 g_{RMS}
Long. Conf.	X (cross)	0.104 g_{RMS}	0.113 g_{RMS}	0.059 g_{RMS}
	Y (cross)	0.137 g_{RMS}	0.150 g_{RMS}	0.037 g_{RMS}
	Z (main)	0.580 g_{RMS}	0.580 g_{RMS}	0.590 g_{RMS}
Vert. Conf.	X (cross)	0.096 g_{RMS}	0.102 g_{RMS}	0.030 g_{RMS}
	Y (cross)	0.156 g_{RMS}	0.166 g_{RMS}	0.037 g_{RMS}
	Z (main)	0.540 g_{RMS}	0.535 g_{RMS}	0.547 g_{RMS}

exceed the main axis PSD). In accordance with the Standard's rules, both sequential single axis tests carried out with SISO control strategy must be considered invalid. The MIMO control configuration instead, even if introduces a slightly lower control quality in the main axis of vibration (always within the control abort limits), keeps the feedback control of the cross axis responses towards low levels. The cross axis peaks are significantly reduced or even eliminated. Table 3 summarizes some significant values to describe the cross axes behaviour. N_{OVER} is the number of spectral lines in which the cross axis PSD exceeded the acceptable threshold. N_{OVER} is also expressed as a percentage of the total spectral lines in the bandwidth. Δ_{MAX} provides the maximum difference between the cross axis PSD and the threshold PSD. It can be noted how, for Longitudinal Configuration in Combination I, Δ_{MAX} along cross axis Y is equal to 14.3 dB. It means that, at the frequency of interest, the measured cross axis PSD is about 27 time higher than the permitted level. The three-dimensional scatter plots deriving from the control point acceleration signals, shown in Figure 13, give a further remarkable insight of the better behaviour of the MIMO control strategy on globally limiting the cross axis

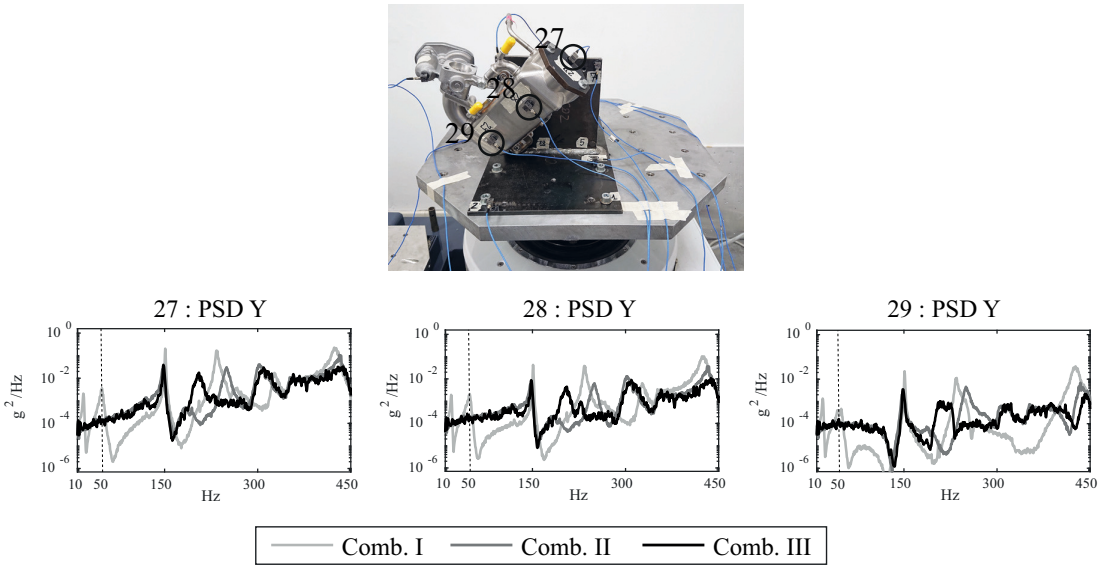

Figure 14: Measurement point results for single axis vibration test in transversal configuration: Comb. I) single axis shaker - SISO control; Comb. II) 3-DoF shaker table - SISO control; Comb. III) 3-DoF shaker table - MIMO control.

vibrations. Combination III offers a high straight line distribution of the data along the main axis of vibration, thus ensuring to excite the test specimen in the effective single axis testing manner. Moreover, Table 4 provides the gRMS values of all recorded control signals. The values confirm the previous results, i.e. Combination III guarantees at least one-half lower cross axis values with respect to other test combinations.

The evident different capability of SISO and MIMO control strategies to perform true single axis vibration test, inevitably implies some differences on the dynamics behaviour of the test specimen during the various control tests. Figure 14 shows the effects that uncontrolled cross axis vibrations cause on the EGR valve. For sake of brevity, the results of transversal configuration are taken as demonstrative example, but similar results can be obtained for the other test configurations. The three plots correspond to three measurement points fixed on the EGR valve, i.e. points 27, 28 and 29 (highlighted with black circles in the top of the figure). The light-grey, grey and black curves are the measured PSDs for Combinations I, II and III respectively. It can be noted that the frequencies where the PSD profiles of Combinations I and II (SISO cases) do not match the profile of Combination III (MIMO case), are the

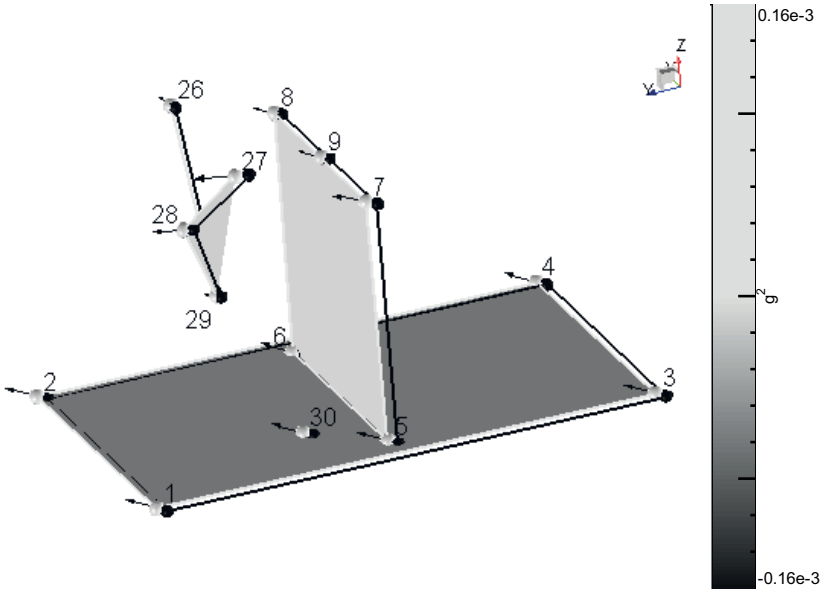

Figure 15: Operational Deflection Shape analysis at 49 Hz for single axis vibration test in transversal configuration with Combination I) single axis shaker - SISO control.

same frequencies where uncontrollable cross axis peaks occur at control point (Figure 12). For these critical frequencies, an Operational Deflection Shape (ODS) analysis has been done in order to provide additional insight about the nature of the mismatched peaks. An example is given in Figure 15 for the peak at 49 Hz. The analysis highlights a rigid deflection shape mode of the entire system (EGR valve and fixture). Therefore, the recorded peak in the measurement points cannot be considered a characteristics of the EGR valve resonance, but it is a consequence of the SISO control configuration that excites the test specimen along a cross axis.

3.5 CONCLUDING REMARKS

This work tackles the problem of high level cross axis responses during single axis vibration control test. Two different excitation systems, i.e. a single axis shaker and a 3-DoF shaker table, have been used in combination with two different control strategies: the SISO control technique (nowadays common

practice) and the MIMO control technique (more advanced practice). An EGR valve has been used as the test specimen for the sequential single axis random vibration control test. The control test results clearly point out different capabilities of the two control strategies. In particular, SISO control configuration results to be ineffective when the system dynamics is such that cross axis vibrations occur at the control point location. In some cases, the cross axis peaks are comparable with the acceleration levels on the main axis of vibration thus compromising the validity of the single axis vibration test. The use of MIMO control strategy totally overcomes these limitations by feedback controlling the cross axis vibrations towards low levels. Moreover, the work has shown the key role of the MIMO control target definition. A proper definition of the reference SDM can improve the potential of MIMO control strategy in order to definitely avoid the cross axis vibration problems. Finally, the analysis on the measurement points has verified that uncontrollable cross axis excitations can alter the dynamic behaviour of the test specimen.

4

MIMO TARGET GENERATION TECHNIQUES FOR DRIVES POWER MINIMIZATION

4.1 INTRODUCTION

In multi-axis vibration control testing, the power required by the excitation system for replicating the user-defined test specifications is a limiting factor which cannot be overlooked. Objective of this chapter is thus to investigate the so-called problem of meeting the *minimum drive criteria*. Excessive power, on top of over-stressing the often expensive test equipment, could cause data acquisition overloads which inevitably interrupt the test even before the full level run. In MIMO control testing, the power required by the exciters is strictly related to the target definition procedure. According to the output-to-input relationship of Equation (10) detailed in Chapter 2, the theoretical definition of the input SDM can be expressed in the extended form as

$$\begin{bmatrix} S_{uu,11} & \dots & S_{uu,1m} \\ \vdots & \ddots & \vdots \\ S_{uu,m1} & \dots & S_{uu,mm} \end{bmatrix} = \begin{bmatrix} \hat{Z}_{11} & \dots & \hat{Z}_{1m} \\ \vdots & \ddots & \vdots \\ \hat{Z}_{\ell 1} & \dots & \hat{Z}_{\ell m} \end{bmatrix} \begin{bmatrix} S^{ref}_{yy,11} & \dots & S^{ref}_{yy,1\ell} \\ \vdots & \ddots & \vdots \\ S^{ref}_{yy,\ell 1} & \dots & S^{ref}_{yy,\ell\ell} \end{bmatrix} \begin{bmatrix} \hat{Z}'_{11} & \dots & \hat{Z}'_{\ell 1} \\ \vdots & \ddots & \vdots \\ \hat{Z}'_{1m} & \dots & \hat{Z}'_{m\ell} \end{bmatrix} \tag{20}$$

Equation (20) evidences that all the elements of the reference SDM are involved on the computation of each diagonal term of the input SDM, i.e. the PSDs of the input drive signals. It follows that, if the estimated impedance matrix ($\hat{\mathbf{Z}}$) has non-zero off diagonal elements, it can be possible to vary the drives power by changing the phases and the coherences of the reference CSDs without compromising the reference PSDs (test specifications). This briefly introduction highlights that an accurate definition of the MIMO control target can allow

the conduct of the control test minimising the overall power required by the shakers.

In the recent years advanced procedures have been developed in this research direction. The currently available drives power reduction techniques are: the *EIOM* [56, 57] and the *IDM* [58]. Both the algorithms have some limitations that will be critically analysed in Section 4.2. Furthermore, two novel MIMO target generation techniques, namely *Minimum Drives Method (MDM)* and *Minimum Single Drive Method (MSDM)*, are presented in Section 4.3 and Section 4.4, respectively. In particular, the *MDM* is a MIMO target generation technique that overcomes the algebraic constrain limitation of the *EIOM*, making the procedure fully automatic and suitable for random control testing. The *MSDM* instead, wants to be an alternative solution when the power required by the multiple-exciter system is mostly exploited by a single shaker. In order to show the capabilities of the proposed techniques and to point out the advantageous and disadvantageous of each procedure, the MIMO target generation algorithms are firstly theoretically explained and then experimentally compared by using the 3 DoF electrodynamic shaker at the University of Ferrara. The test results are discussed in Section 4.5. Finally, Section 4.6 provides the concluding remarks of this research activity.

4.2 STATE-OF-THE-ART SOLUTIONS

4.2.1 *Extreme Inputs/Outputs Method (EIOM)*

This MIMO target generation procedure has been the pioneer on the drive power reduction for multi-axis tests and it represents a milestone in this area. In the late 80's, Smallwood proposed a first draft of the method [55]. However, the *EIOM* has been finally formalized around 20 years later in [56]. As explained in the following, the procedure contains a flaw and a solution to the problem has been suggested by the same author in a subsequent work [57].

The idea behind the *EIOM* is to take the sum of the drives power as an indicator for the overall power required by the exciters. In algebraic terms, this means to find the set of coherences and phases between the control channels that minimises the drives trace. The choice of the drive trace as quantity to be minimized is undoubtedly advantageous because a closed form expression can

be derived in terms of user-defined PSDs and in terms of unknown coherences and phases between pairs of control channels.

In the general case of m inputs and ℓ outputs, the diagonal terms of the input SDM expressed in the extended from in Equation (20) can be calculated as

$$S_{uu,ii} = \sum_{j=1}^{\ell} \sum_{k=1}^{\ell} \hat{Z}_{ij} S^{ref}_{yy,jk} \hat{Z}'_{ik} \qquad \forall i = 1 : m \tag{21}$$

By definition the trace of the input SDM is the sum of the diagonal terms [60]

$$P = Tr(\mathbf{S_{uu}}) = \sum_{i=1}^{m} \left(\sum_{j=1}^{\ell} \sum_{k=1}^{\ell} \hat{Z}_{ij} S^{ref}_{yy,jk} \hat{Z}'_{ik} \right) \tag{22}$$

By introducing matrix $\mathbf{F} = \hat{\mathbf{Z}}^{\mathbf{H}} \hat{\mathbf{Z}}$, Equation (22) can be written as

$$P = \sum_{j=1}^{\ell} \sum_{k=1}^{\ell} S^{ref}_{yy,jk} \sum_{i=1}^{m} \hat{Z}'_{ik} \hat{Z}_{ij} = \sum_{j=1}^{\ell} \sum_{k=1}^{\ell} S^{ref}_{yy,jk} F_{kj} \tag{23}$$

Due to the Hermitian form of both $\mathbf{S^{ref}_{yy}}$ and $\mathbf{F}$, Equation (23) can be expressed as

$$P = \sum_{j=1}^{\ell} S^{ref}_{yy,jj} F_{jj} + 2 \sum_{j=1}^{\ell-1} \sum_{k=j+1}^{\ell} Re\{S^{ref}_{yy,jk} F'_{jk}\} \tag{24}$$

Therefore, the drives trace can be finally defined in terms of coherences and phases between the pairs of control channels, i.e. the information that needs to be provided to the vibration controller

$$P = \sum_{j=1}^{\ell} S^{ref}_{yy,jj} F_{jj} + 2 \sum_{j=1}^{\ell-1} \sum_{k=j+1}^{\ell} \sqrt{\gamma^2_{jk} S^{ref}_{yy,jj} S^{ref}_{yy,kk}} \left| F_{jk} \right| \cos(\phi_{jk} - \theta_{jk}) \tag{25}$$

where

$$S^{ref}_{jk} = \left| S_{jk} \right| e^{i\phi_{jk}} = \sqrt{\gamma^2_{jk} S^{ref}_{yy,jj} S^{ref}_{yy,kk}}\, e^{i\phi_{jk}} \tag{26}$$

$$F_{jk} = \left| F_{jk} \right| e^{i\theta_{jk}} \tag{27}$$

It is worth noticing that the matrix $\mathbf{F}$ can be computed from the estimated FRFs matrix ($\hat{\mathbf{H}}$) during the system identification pre-test phase and therefore the terms $|F_{jk}|$ and θ_{jk} can be considered as known quantities. Also the PSD terms ($S^{ref}_{yy,jj}\ \forall jj = 1:\ell$) are known and considered as test specifications. The first term on the right hand side of Equation (25) is always positive and fixed for the given test specifications and test setup. The second term contains the quantities ϕ_{jk} and γ^2_{jk} that is unknowns of the target definition procedure. This term can be negative because of the cosine function and it can provide a negative contribution on the drives trace calculation. Therefore, the expression of Equation (25) has a minimum if

$$\begin{cases} \phi_{jk} = \theta_{jk} + \pi \\ \gamma^2_{jk} = 1 \end{cases} \qquad \forall j = 1:\ell,\ \forall k = 1:\ell,\ j \neq k \tag{28}$$

In the following the conditions of Equation (28) will be referred as the *Minimum Trace Conditions*.

Therefore, the reference phase of the *Minimum Trace Conditions* guarantees that all the cosines are equal to -1, meaning that each cross term of the double summation will be subtracted from the positive and fixed term. Moreover, the coherences equal to 1 guarantees that all the cross terms will be subtracted with the maximum amplitude, meaning that the drives trace will be fully minimized. By imposing the *Minimum Trace Conditions* into Equation (25), the drives trace is

$$P = \sum_{j=1}^{\ell} S^{ref}_{yy,jj} F_{jj} - 2 \sum_{j=1}^{\ell-1} \sum_{k=j+1}^{\ell} \sqrt{S^{ref}_{yy,jj} S^{ref}_{yy,kk}}\, |F_{jk}| \tag{29}$$

All the other possible combinations of coherences and phases return drive traces with higher value, i.e higher total power required. The effects on the drives trace minimization considering different phases and coherences selection are graphically explained in Figure 16. The drive trace (P) can be seen as the summation of two real terms: the single sum in Equation (25) is fixed and always positive and it is represented by the red solid arrow. The solid blue arrow is representative for the double summation in Equation (25). This term is tunable since it contains the phase and the coherence between pairs of control channels that need to be defined. Each contribution to the sum can be

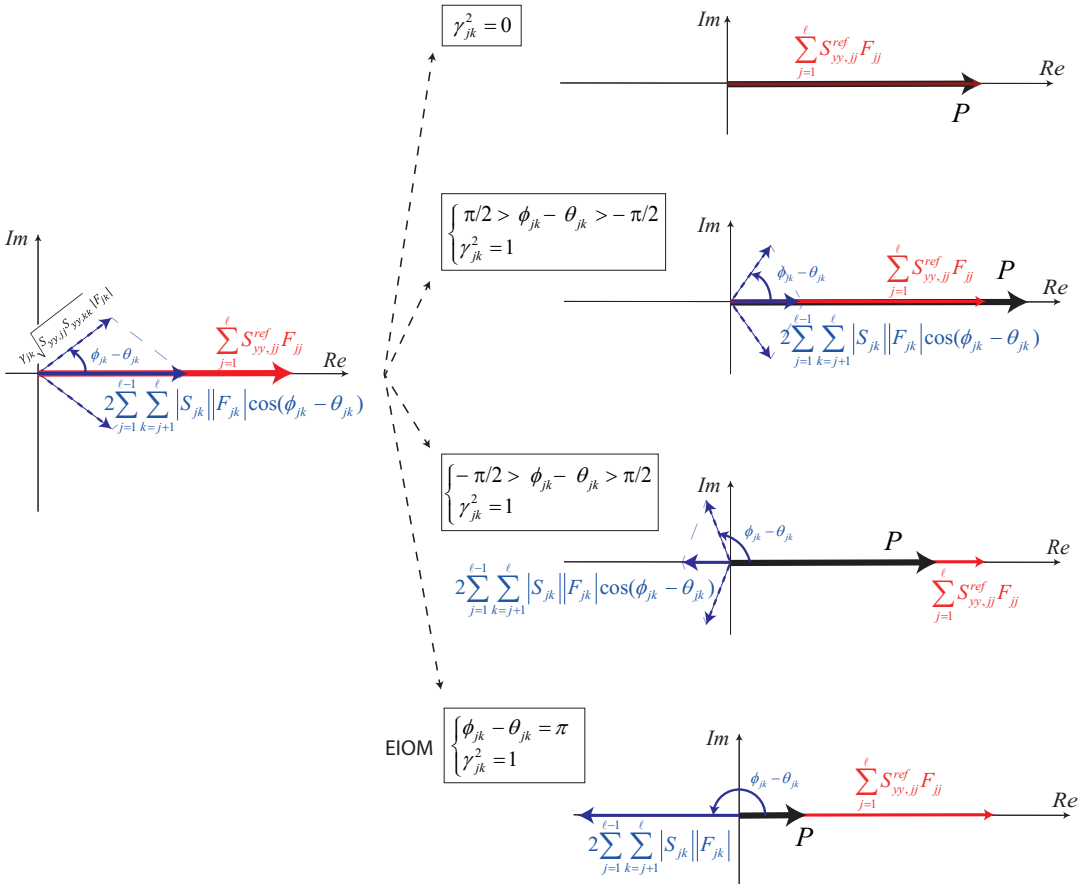

Figure 16: *EIOM*: phases and coherences selection

interpreted as the projection on the complex plane's real axis of a vector with magnitude $|F_{jk}|\sqrt{S_{yy,jj}\, S_{yy,kk}}$ scaled by $\sqrt{\gamma_{jk}^2}$ and with phase $(\phi_{jk} - \theta_{jk})$, represented by the dash-dot arrows. Being the coherence a real number between 0 and 1, the multiplication by its square root scales these vectors. The phases instead, change the orientation of the projection along the real axis. The *EIOM* suggests the maximum possible reduction from the positive fixed term, since all the (unscaled) vectors are forced to lay on the negative real axis.

Unfortunately, this MIMO target generation procedure cannot be used to run a control test because it does not guarantee that the resulting reference SDM is positive (semi)definite. To meet the *Minimum Trace Conditions*, all the cross-terms in the double summation of Equation (25) are forced to assume

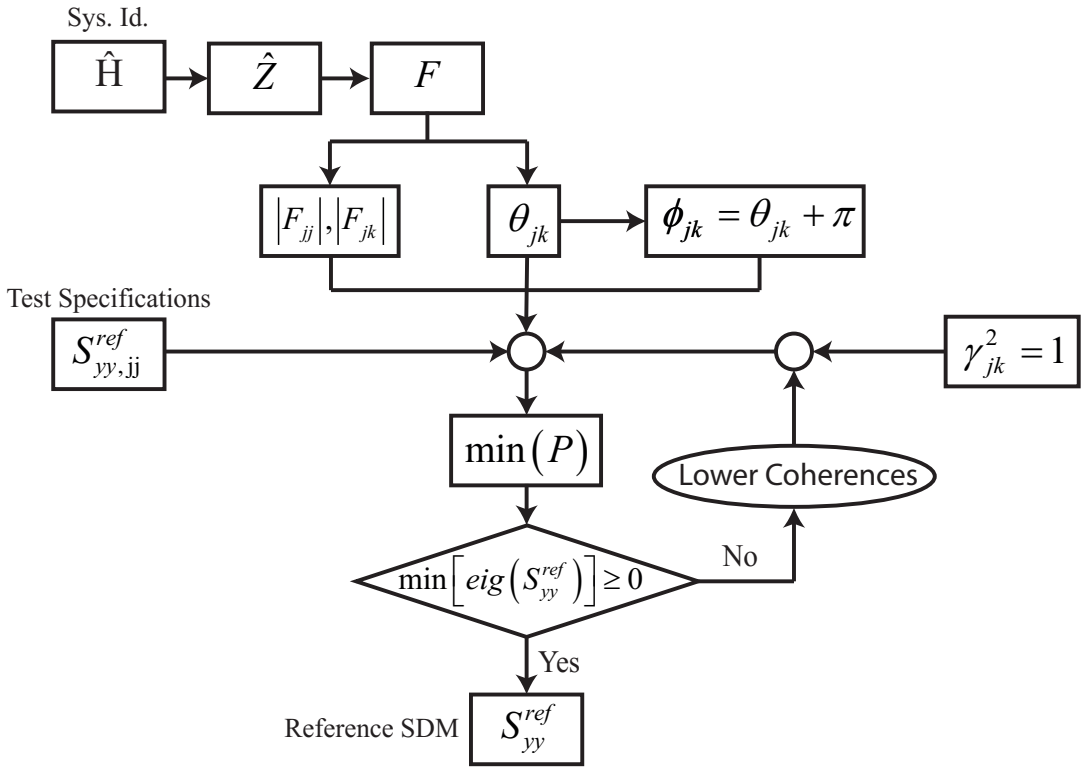

Figure 17: *EIOM* algorithm block scheme.

the biggest negative values and they can eventually overcome in module the fixed and positive term, leading to a negative drives trace. This hypothesis is clearly not allowed: since the matrix trace is the sum of its eigenvalues [60], if the drives trace is negative then one eigenvalue is negative at least. For a matrix, one of the necessary and sufficient conditions in order to be positive (semi)definite is that all its eigenvalues must be (semi)positive (see Section 2.3). By definition, if the input SDM ($\mathbf{S_{uu}}$) is negative definite, the respective reference SDM ($\mathbf{S^{ref}_{yy}}$) is negative definite too [60].

In order to overcome this limitation and to make the *EIOM* suitable for practical control testing, Smallwood proposes the use of a constrained optimization algorithm [57]. The idea is to fix the reference phases in accordance with the *Minimum Trace Conditions* and to find the coherence combination that

minimises the drives trace with the additional constraint that the eigenvalues of the resulting reference SDM are all positive

$$\min\left[P(\gamma_{jk})\right] : \ \min\left[eig(\mathbf{S}_{\mathbf{yy}}^{\mathbf{ref}})\right] \geqslant 0 \tag{30}$$

where

$$P(\gamma_{jk}) = \sum_{j=1}^{\ell} S_{yy,jj}^{ref} F_{jj} - 2 \sum_{j=1}^{\ell-1} \sum_{k=j+1}^{\ell} \gamma_{jk} \sqrt{S_{yy,jj}^{ref} S_{yy,kk}^{ref}} \left|F_{jk}\right| \tag{31}$$

Loosely speaking the optimization algorithm decreases the coherence values iteration by iteration. The cross terms in the double summation of Equation (31) are thus rescaled down until the drives trace is positive. Figure 17 schematically represents the *EIOM* with the constrained optimization procedure.

4.2.2 *Independent Drives Method (IDM)*

This MIMO target generation procedure [58] addresses the issue of reducing the drives power needed to perform a control test with fixed test specifications, by driving the excitation system with a set of uncorrelated inputs (independent drives). By referring to Equation (20), the aim of the *IDM* is thus to find the set of phases and coherences for the reference CSDs which finally results in a diagonal input SDM.

Considering the input-output relation of Equation (20), in case of m inputs and ℓ outputs, the diagonal elements of the output SDM can be computed as

$$S_{yy,jj} = \sum_{i=1}^{m} \sum_{k=1}^{m} S_{uu,ik} H_{ji} H'_{jk} \qquad \forall j = 1 : \ell \tag{32}$$

If the input SDM ($\mathbf{S_{uu}}$) is a diagonal matrix, Equation (32) is reduced to

$$S_{yy,jj} = \sum_{i=1}^{m} S_{uu,ii} |H_{ji}|^2 \qquad \forall j = 1 : \ell \tag{33}$$

Therefore the m independent drives, which are able to replicate the ℓ user defined test specifications, can be computed as

$$X = \tilde{\mathbf{H}}^{\dagger} \, Y_{ref} \tag{34}$$

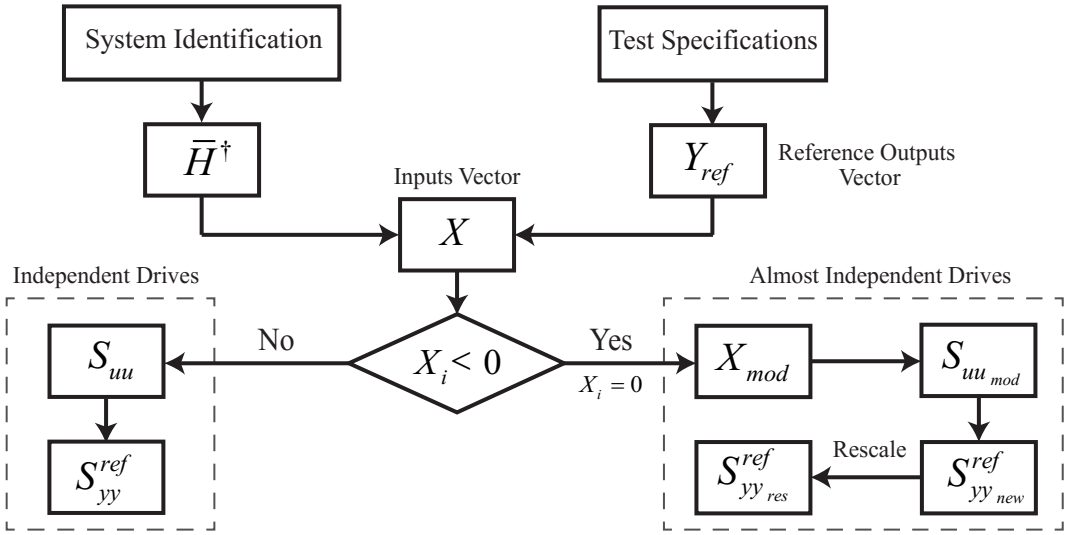

Figure 18: *IDM* algorithm block scheme.

where $Y_{ref} \in \mathbb{R}^{\ell \times 1}$ is the reference PSD vector and $\bar{\mathbf{H}}^{\dagger} \in \mathbb{R}^{m \times \ell}$ is the (pseudo) inverse of $\bar{\mathbf{H}} = [\mathbf{H}. * \mathbf{H}']$.

Finally, by computing the input SDM as $\mathbf{S_{uu}} = \mathtt{diag}(X)$, the full reference SDM with all the information about the cross correlation between the control channels can be easily defined as

$$\mathbf{S^{ref}_{yy}} = \mathbf{H}\mathbf{S_{uu}}\mathbf{H^{H}} \tag{35}$$

It is important noticing that it is not always possible to replicate the user defined test specifications using decorrelated inputs. In some cases, due to the dynamic behaviour of the unit under test or depending on the adopted sensors configuration, a correlation between the drives is strictly needed. It is thus possible that at some frequencies the input vector X, computed from Equation (34), presents negative values suggesting the physical weakness of the process. In order to overcme this limitation, the negative values of X are set equal to zero and a new reference SMD ($\mathbf{S^{ref}_{yy\ new}}$) is obtained from the modified input SDM ($\mathbf{S_{uu\ mod}} = \mathtt{diag}(X_{\mathtt{mod}})$). Clearly, a variation of some values of X is translated into an alteration of the test specifications. Nevertheless it can be possible to rescale the reference PSDs up to the required level

$$\mathbf{S^{ref}_{yy\ res}} = \mathbf{R}\ \mathbf{S^{ref}_{yy\ new}}\mathbf{R} \tag{36}$$

where $\mathbf{R}$ is a diagonal matrix and

$$R_{jj} = \sqrt{\frac{S^{ref}_{yy,jj\,res}}{S^{ref}_{yy,jj\,new}}} \tag{37}$$

$\mathbf{S^{ref}_{yy\,res}}$ is the reference SDM with the user defined reference PSDs on the diagonal and with the CSD phases and coherences deriving from the modified input vector X_{mod} (almost independent drives). The *IDM* algorithm is schematically shown in a block diagram in Figure 18.

4.3 NOVEL SOLUTION: MINIMUM DRIVES METHOD

The following section presents the *Minimum Drives Method* (*MDM*) that is the first MIMO target generation technique provided in this thesis. The *MDM* extends the work of Smallwood [56] and it provides an alternative solution to the *EIOM* flaw which is discussed and critically reviewed in Section 4.2.1. The idea of minimizing the drives trace in order to reduce the total power required by the multiple shakers is an interesting solution. However, the use of a constrained optimization routine inside the procedure inevitably increases the computational cost and the time to target of the process. Moreover, the convergence to a feasible solution also depends to the user experience on tuning the convergence parameters. These factors makes the *EIOM* not practical for performing MIMO random control testing. Therefore, starting from the drives trace formulation of Equation (25), rather than modifying the reference coherence values, the *MDM* tackles the problem by adapting the reference phase of the *Minimum Trace Conditions* shown in Equation (28).

The reason why the *Minimum Trace Conditions* cannot be used to generate a physically realizable target is that the reference phases cannot be independently set. In fact, in case of fully coherent control responses, the phases of the control channel pairs are mutually linked from a strong physical relation. A mathematical proof can be found by analysing the simple case of three control channels. For the reference SDM ($\mathbf{S^{ref}_{yy}}$) to be positive (semi)definite, it is necessary and sufficient that the Sylvester's Criterion holds (see property (c) in Section 2.3) and therefore that

$$\det(\mathbf{S^{ref}_{yy}}) = 1 - \gamma^2_{12} - \gamma^2_{13} - \gamma^2_{23} + 2\cos(\phi_{12} - \phi_{13} + \phi_{23})\sqrt{\gamma^2_{12}\,\gamma^2_{13}\,\gamma^2_{23}} \geqslant 0 \tag{38}$$

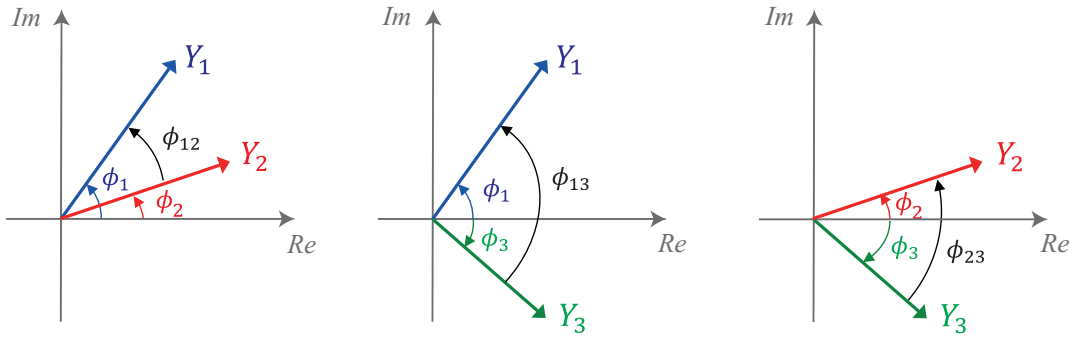

Figure 19: Example of phase relation for three fully coherent control channels. Given the phases ϕ_{12} and ϕ_{13}, the phase ϕ_{23} is unequivocally defined as the difference between the other two.

Thus, in case of fully coherent control channels (unitary coherences), to verify the Sylvester's Criterion the cosine's argument must be nullified

$$\begin{cases} \det(\mathbf{S}_{yy}^{ref}) \geqslant 0 \\ \gamma_{12}^2 = \gamma_{13}^2 = \gamma_{23}^2 = 1 \end{cases} \quad \Rightarrow \quad \phi_{12} - \phi_{13} + \phi_{23} = 0 \tag{39}$$

Equation (39) highlights that a strong deterministic relation needs to exist between the phases to be selected. This can be physically explained by associating these phases to the ones of the respective recorded spectra, as shown in Figure 19. Setting the phases ϕ_{12} and ϕ_{13} means to set a *relative constraint* in the phase information carried by two pairs of recorded signals, i.e. between controls 1 and 2 and between controls 1 and 3, respectively. Therefore, the phase ϕ_{23} between the control channels 2 and 3 is unequivocally defined as the difference between ϕ_{13} and ϕ_{12}.

The mathematical proof of Equation (39) and the physical explanation of Figure 19 point out that, a realizable and controllable target to be used for testing purposes cannot be obtained with the *Minimum Trace Conditions* of Equation (28), unless the $(\theta + \pi)$ angles do not respect the aforementioned relations.

As a general conclusion for ℓ fully coherent control outputs, it is fair to say that just $(\ell - 1)$ reference phases can be freely set using the *Minimum Trace*

Conditions. The remaining ones instead, must be retrieved following a principle that respects the existing relative constraints. This principle will be addressed in the following as *Phase Pivoting Principle*.

On the basis of this need, the objective of the *MDM* is to provide an algorithm, namely *Phase Pivoting Algorithm*, able to automatically choose $(\ell - 1)$ independent terms on which the *Minimum Trace Conditions* can be applied and then, to calculate the remaining terms in accordance with the *Phase Pivoting Principle*. A first version of the proposed algorithm (Version I) and a subsequent development (Version II) will be discussed in the following sections. Moreover, two case studies with simulated results will be shown to point out the limitations of the first version and the improvements achieved with the second version.

4.3.1 *Phase Pivoting Algorithm: Version I*

In the general case of ℓ fully coherent control outputs, to select the $(\ell - 1)$ independent phase terms on which to set the *Minimum Trace Conditions*, the Version I of the *Phase Pivoting Algorithm* proposes three different solutions:

i) *First Row Method* sets the $(\ell - 1)$ phase terms of the first row of the upper triangular part of the reference SDM

$$\phi_{1k} = \theta_{1k} + \pi \qquad \forall k = 2 : \ell$$

ii) *Last Column Method* sets the $(\ell - 1)$ phase terms of the last column of the upper triangular part of the reference SDM

$$\phi_{k\ell} = \theta_{k\ell} + \pi \qquad \forall k = 1 : (\ell - 1)$$

iii) *Second Diagonal Method* sets the $(\ell - 1)$ phase terms of the second diagonal of the upper triangular part of the reference SDM

$$\phi_{jk} = \theta_{jk} + \pi \qquad \forall j = 1 : (\ell - 1) \quad \& \quad k = j + 1$$

Then, all the three solutions complete the upper triangular part of the reference SDM retrieving the remaining reference phases in accordance with the *Phase Pivoting Principle* ($\phi_{jk} = \phi_{ik} - \phi_{ij}$). Of course, the lower triangular

part of the reference SDM is subsequently defined due to the Hermitian form of the matrix ($\phi_{kj} = -\phi_{jk}$).

As one might expect, the three different solutions i), ii) and iii) generate three different reference SDMs, each of which offers a different drives power reduction. Therefore, to guarantee the maximum power reduction, the *Phase Pivoting Algorithm* theoretically runs (Equation 10) the three solutions in series and, for each spectral line, it takes the reference SDM which provides the lowest drives trace result. Loosely speaking, the resulting drives trace is the envelope of the minimum values calculated between the three different solutions (i), ii) and iii)).

In the following section, a case study which simulates a three-drives three-controls random test will be used to validate the novel concepts introduced by the *MDM* and to highlight the applicability of the *Phase Pivoting Algorithm: Version I*.

4.3.2 *Case study: three-drives three-controls simulated test*

This section presents the results of a case study to point out the capabilities of the *MDM* combined with the first version of the *Phase Pivoting Algorithm*. The results shown in the following derive from a simulated test, i.e. the input SDM is directly calculated from the input-output relation of Equation (10). This means that the predicted drives trace and the resulting power reduction are purely theoretical. It is worth to notice that, the final objective of this case study is to compare the drives power results obtained with the *MDM* (*Phase Pivoting Algorithm - Version I*) with respect to the *EIOM* (*Minimum Trace Conditions* - without the constrain optimization routine). As previously explained, the *EIOM* combined with the *Minimum Trace Conditions* generates negative definite matrix that cannot be used in practical MIMO control tests. Therefore, in order to compare the two methods, the only available solution is via simulated test.

However, in order to improve the reality of this simulated case study, the system's mechanical impedance matrix ($\mathbf{Z}$) to be used in Equation (10) comes from real experimental data. In particular, the data refer to a test campaign conducted at the University of Ferrara on a EGR valve. This automotive component has been provided by *VM motori* (Italian company specialized in the development of diesel engines) to the *MechVib*, thanks to the intense collaboration that has been established over the years between the two Groups.

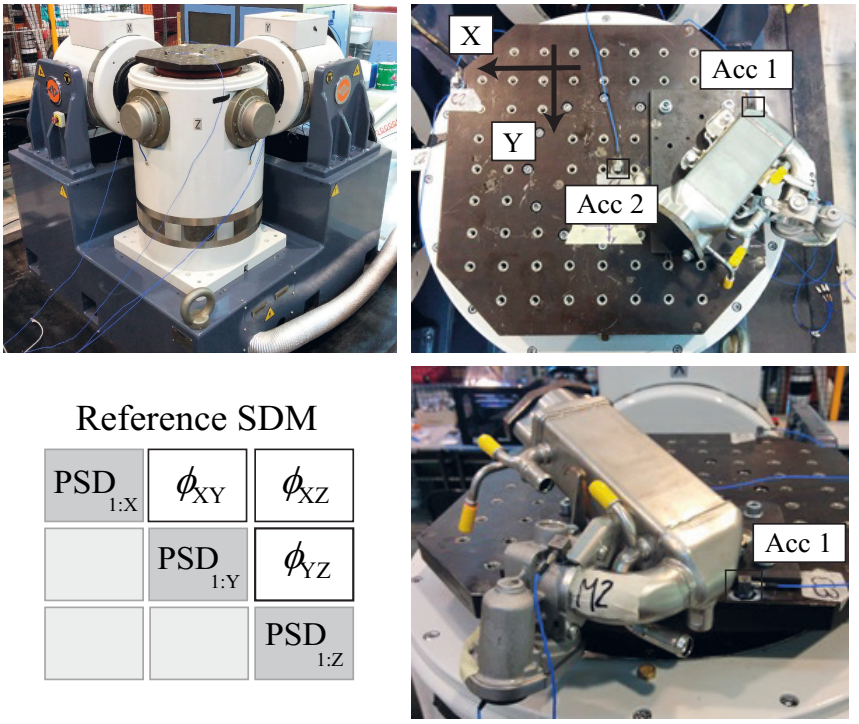

Figure 20: Setup of the three-drives three-controls simulated test. 3 DoF shaker table at the University of Ferrara (left-top); top/side views of the EGR valve mounted on the head expander (right-top/bottom); basic outline of the reference SDM (left-bottom).

The EGR valve has been used as a test specimen for different research activities, such as the one discussed in Chapter 3. Figure 20 shows the setup of the three-inputs three-outputs system adopted to estimate the mechanical impedance matrix of this case study. The 3-DoF shaker table at the University of Ferrara is the three-drives excitation system. The three directions (X, Y and Z) of a three-axial accelerometer are the three outputs. The accelerometer is fixed close to test specimen on the head expander mounting point and it is labelled as *Acc 1* in Figure 20. A low level random test with decorrelated inputs is performed to estimate the FRFs matrix that links the three outputs to the three inputs. The resulting 3x3 FRFs matrix ($\mathbf{H}$) is shown in Figure 21. Finally, the system's mechanical impedance is computed from the FRFs matrix ($\mathbf{Z} = \mathbf{H}^{-1}$)

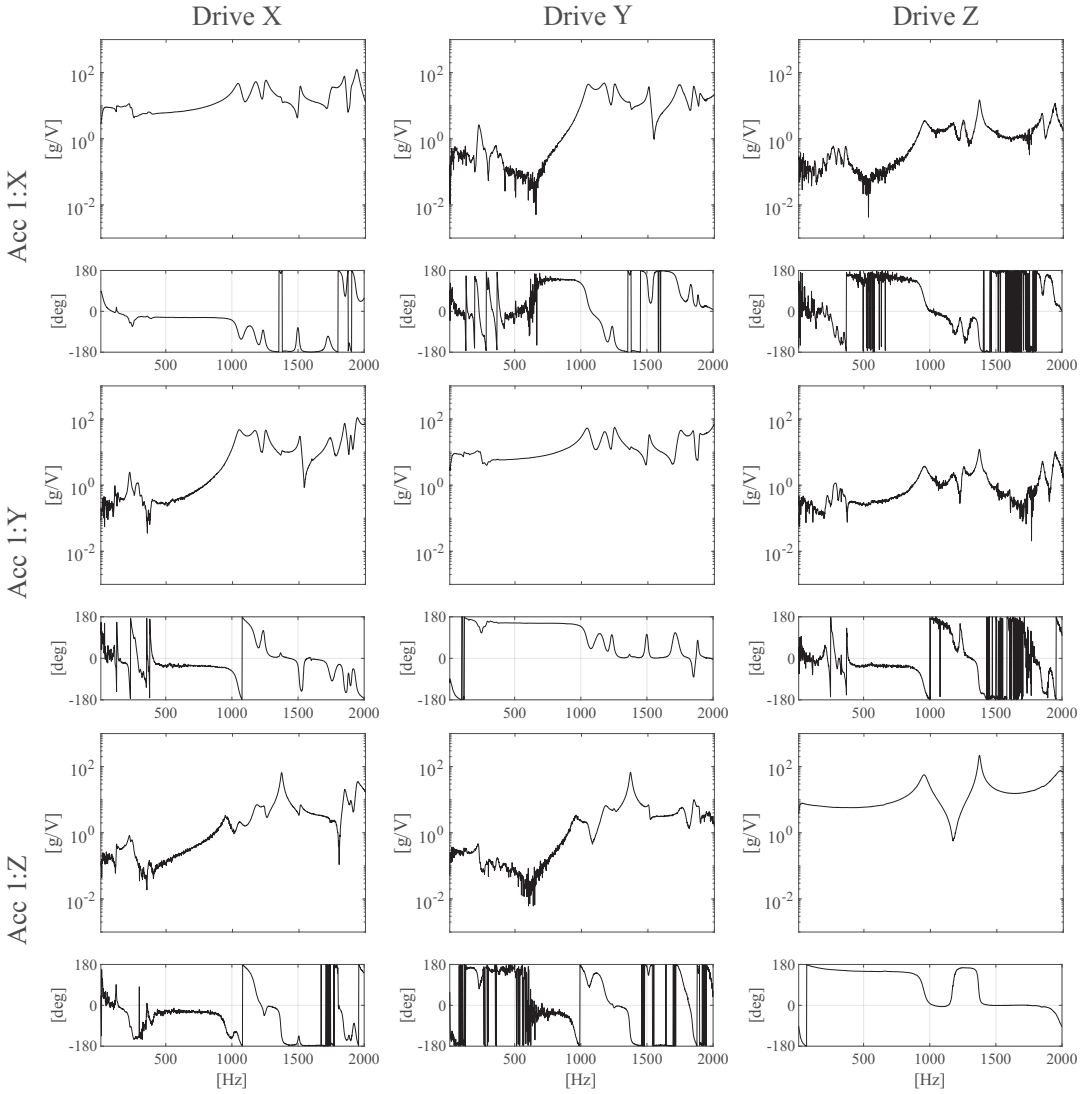

Figure 21: 3x3 FRFs matrix used in the three-drives three-controls simulated test.

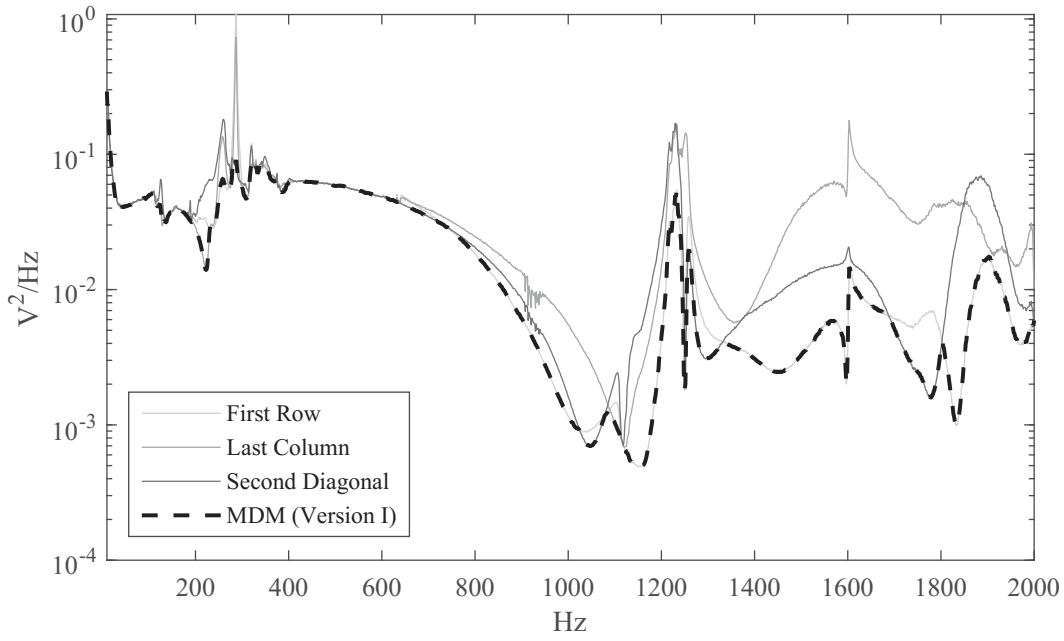

Figure 22: Three-drives three-controls simulated test: drive trace results of the phase-selection methods exploited by the *Phase Pivoting Algorithm - Version I*

and used in Equation (10) to predict the input SDM starting from the reference SDM.

Figure 20 provides the basic outline of the reference SDM used to perform the three-drives three-controls simulated test. The three control channels are the three directions of *Acc 1*. The test specification for all the control channels is a flat PSD with unitary amplitude in the frequency range $[10 - 2000]$Hz. In accordance with the fill order of the control outputs into the reference SDM (see Figure 20), it is possible to summarize the phase selection methods of the *Phase Pivoting Algorithm* (*Version I*)

i) *First Row Method*

$$\begin{cases} \phi_{XY} = \theta_{XY} + \pi \\ \phi_{XZ} = \theta_{XZ} + \pi \end{cases} \Rightarrow \quad \textit{Independent Phase Terms}$$

$$\phi_{YZ} = \phi_{XZ} - \phi_{XY} \quad \Rightarrow \quad \textit{Retrieved Phase Term}$$

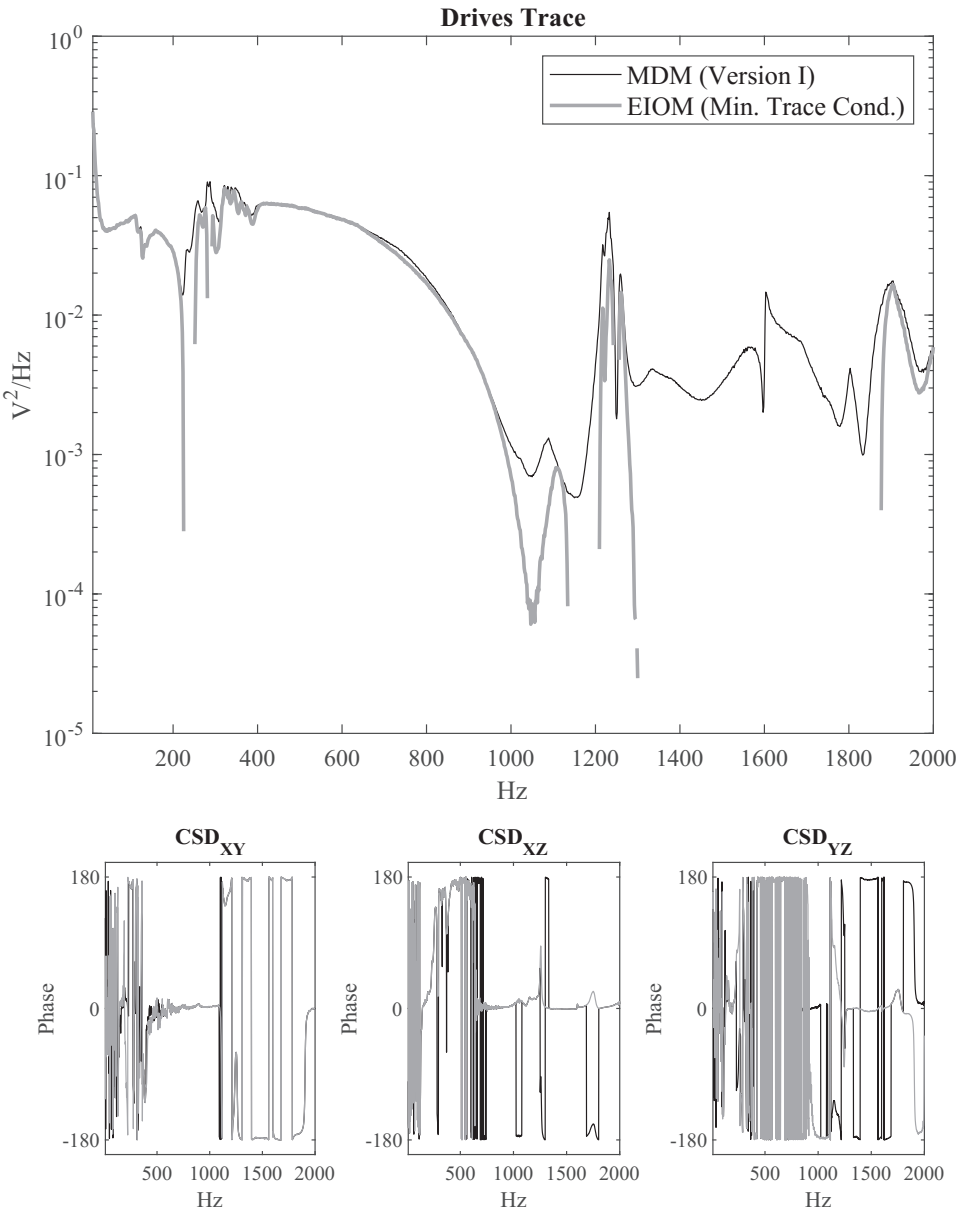

Figure 23: Three-drives three-controls simulated test: comparison between the *MDM* (*Phase Pivoting Algorithm - Version I*) and the *EIOM* (*Minimum Trace Conditions*). Drives trace (top); phases of the reference CSDs (bottom).

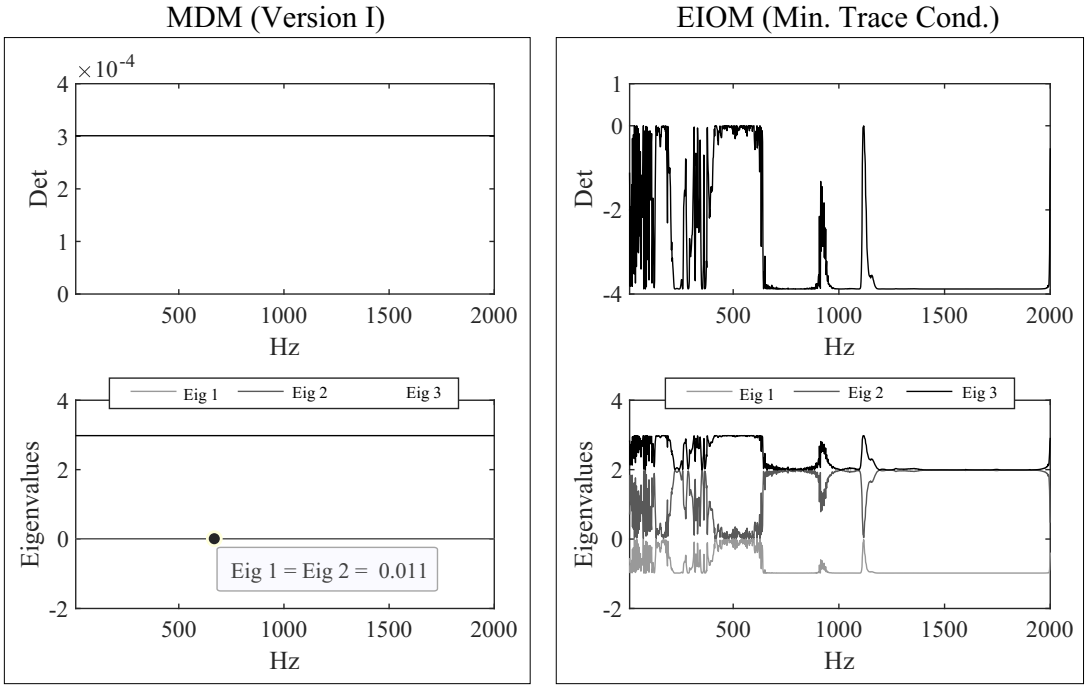

Figure 24: Three-drives three-controls simulated test: comparison between the *MDM* (*Phase Pivoting Algorithm - Version I*) and the *EIOM* (*Minimum Trace Conditions*). Determinant of the reference SDM (top); Eigenvalues of the reference SDM (bottom.)

ii) *Last Column Method*

$$\begin{cases} \phi_{XZ} = \theta_{XZ} + \pi \\ \phi_{YZ} = \theta_{YZ} + \pi \end{cases} \Rightarrow \quad \textit{Independent Phase Terms}$$

$$\phi_{XY} = \phi_{XZ} - \phi_{YZ} \quad \Rightarrow \quad \textit{Retrieved Phase Term}$$

iii) *Second Diagonal Method*

$$\begin{cases} \phi_{XY} = \theta_{XY} + \pi \\ \phi_{YZ} = \theta_{YZ} + \pi \end{cases} \Rightarrow \quad \textit{Independent Phase Terms}$$

$$\phi_{XZ} = \phi_{XY} + \phi_{YZ} \quad \Rightarrow \quad \textit{Retrieved Phase Term}$$

Figure 22 shows the drives trace result obtained by exploiting the *MDM* with the *Phase Pivoting Algorithm* (*Vesrion I*). In particular, the figure graphically explains how the algorithm takes advantage of the three different methods for the selection of the independent phase terms. The light grey, grey and dark grey curves are the drives traces obtained with the reference SDM suggested by the *First Row Method*, the *Last Column Method* and the *Second Diagonal Method*, respectively. It can been seen that, depending of which independent terms are chosen to set the *Minimum Trace Conditions*, the three methods provide different drives trace results. Moreover, there is no method that better performs in the entire frequency band of interest. Therefore, to guarantee the higher drives power reduction at each spectral line, the *Phase Pivoting Algorithm* takes the minimum drive trace solution between the three methods and the corresponding reference SDM. The final MIMO control target will be the reference SDM that generates the dotted black curve of Figure 22 (envelope curve).

Figure 23 finally compares the *MDM* (*Phase Pivoting Algorithm - Version I*) with the *EIOM* (*Minimum Trace Conditions*). It is worth to notice that, this case study does not take into account the use of the constrain optimization routine into the *EIOM*. This aspect will be investigated in Section 4.5. The first notable outcome from the comparison shown in Figure 23 is that the drives trace provided by *EIOM* is negative for large part of the frequency band. Off course, this result would not be physically allowed in a real control test. Moreover, at the remaining spectral lines, the drives trace of the two methods are almost comparable. In some cases the *MDM* offers a slightly higher drives trace, but this is a direct consequence of the resulting reference SDM being positive definite. A negative define matrix indeed, can have a reduced drives trace due to the effect of the negative eigenvalues. As highlighted in Figure 24, the reference SDM of the *EIOM* has a negative eigenvalue and negative determinant for the entire frequency band. As a result, the reference SDM is a negative definite matrix and it cannot be used for a real control test. This result confirms the findings explained in the previous sections, i.e. the *Minimum Trace Conditions* do not respect the relative constraints that mutually link the pairs of control channels. The *MDM* overcomes this limitation by proper selecting the 2 independent terms on which to set the *Minimum Trace Conditions* and by retrieving the phase of the last term. The phase values of the three reference CSDs are shown in the bottom part of Figure 23. The black curves refer to the

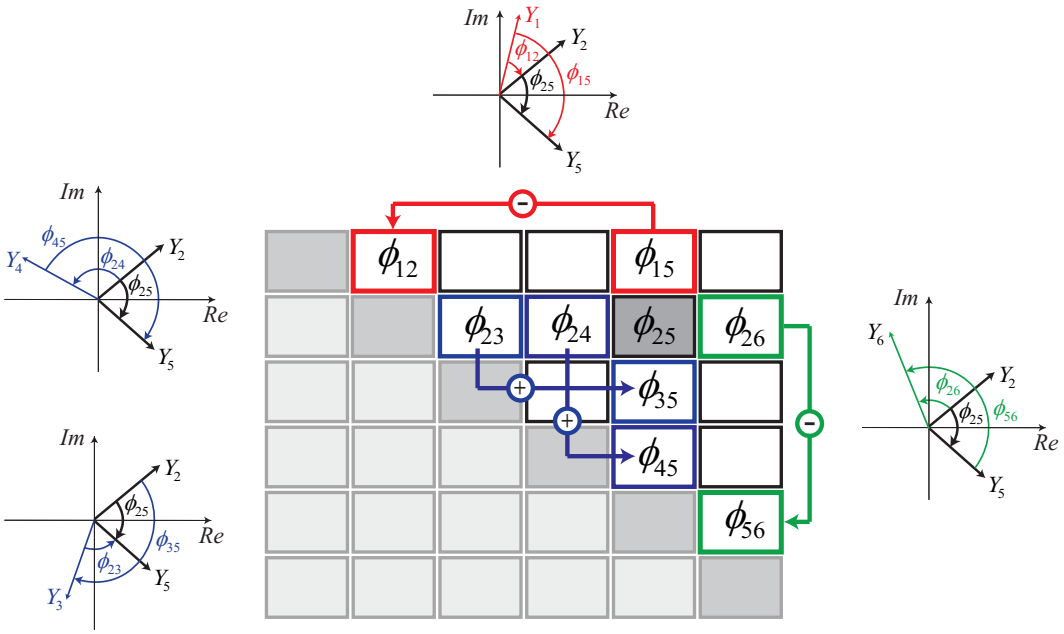

Figure 25: Phase dependencies for cross-term (2,5) of a 6 fully coherent control channel system: row dependency (red line), column dependency (green line) and cross dependency (blue lines).

MDM and the grey curves to the *EIOM*. At each spectral line, the methods exhibit the same phase values just for 2 cross-terms. These two terms can eventually change for each spectral line because of the *Phase Pivoting Algorithm* adopted by the *MDM*, which selects the better solution among the available three (i), ii) and iii)). With this procedure, the *MDM* always provides positive definite and full-rank reference SDM, as proved in Figure 24. The determinant of the matrix and all its eigenvalues are positive, meaning that the resulting control target will be physically realizable and controllable by the modern vibration controllers to successfully perform a MIMO random vibration control test.

4.3.3 *Phase Pivoting Algorithm: Version II*

The results of the previously described case study point out the evident benefits that the first version of the *Phase Pivoting Algorithm* offers to generate

physically realizable MIMO control targets. Moreover, in case of three control outputs, it guarantees the maximum possible drives power reduction thanks to the combination of the three different methods used to set the independent reference phases. However, when the control outputs increase, the algorithm reaching its limitations. In the general case of ($\ell > 3$) control outputs the three phase-selection methods exploited by the algorithm cannot cover all the existing combinations of ($\ell - 1$) independent phase terms to set the *Minimum Trace Conditions*. Due to the combinations not included in the process, which may be the ones with the highest impact on the drives trace minimization, the first version of the *Phase Pivoting Algorithm* is not able to always guarantee an adequate drives power reduction. This drawback is finally addressed by a novel implementation of the algorithm, i.e. *Phase Pivoting Algorithm - Version II*.

The main objective of the second version of the *Phase Pivoting Algorithm* is to make the *MDM* high-performing independently on the number of control channels. However, the valuable features of the previous version must remain preserved, i.e the algorithm must be fully automated and it must provide positive (semi)definite reference SDM, so that it can be used for practical MIMO control testing.

Therefore, in the general case of (ℓ) control outputs, the idea of the novel algorithm is to choose the ($\ell - 1$) independent terms as the ones that contribute the most to the drives trace reduction. Specifically, referring to Equation (25) and Figure 16, the ($\ell - 1$) independent terms should be the ones that have the biggest amplitude $\left|F_{jk}\right| \sqrt{S^{ref}_{yy,jj} S^{ref}_{yy,kk}}$. Of course, the ($\ell - 1$) terms with the biggest amplitude can be found in random order in the matrix and they may eventually change at each spectral line without following a precise pattern. Moreover, the selected ($\ell - 1$) terms must be independent, i.e. they must respect the relative constraints that mutually link the phase terms.

On the basis of this needs, the second version of the *Phase Pivoting Algorithm* formally extends to the general case of (ℓ) control outputs, the phase dependencies that link each term with the other ones. For each term, three dependencies must be considered to fulfil a realizable reference SDM:

i) Row dependency (rows upwards)

$$\phi_{jk} = \phi_{ik} - \phi_{ij} \qquad \forall i = 1 : (j - 1)$$

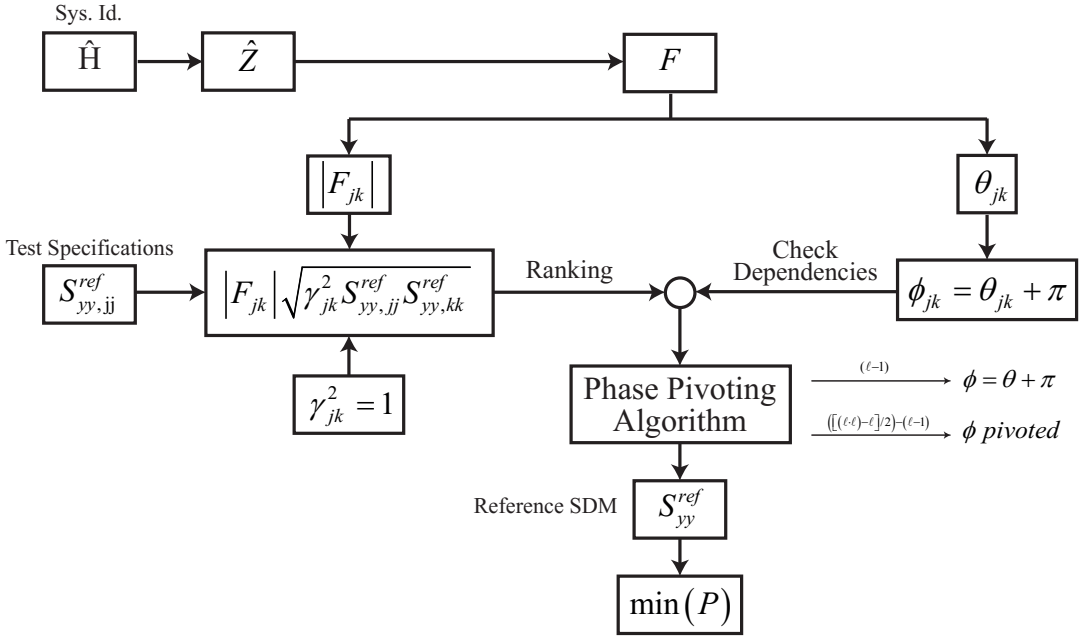

Figure 26: *MDM* algorithm block scheme.

ii) Column dependency (columns to the right)

$$\phi_{jk} = \phi_{ji} - \phi_{ki} \qquad \forall i = (k+1) : \ell$$

iii) Cross dependency (bottom semi-rows and left semi-columns)

$$\phi_{jk} = \phi_{ji} + \phi_{ik} \qquad \forall i = (j+1) : (k-1)$$

An example for a 6 fully coherent control channel system is given in Figure 25. The example graphically explains the phase dependencies under which cross term (2,5) has to be subjected. The figure underlines that the cross term (2,5) is linked to 4 different pairs of cross-terms. It means that, by simply selecting one cross-term, 8 more terms are mutually linked in the process.

Therefore, by exploiting the generalized phase dependencies (i), ii), iii)), the novel *Phase Pivoting Algorithm* is able to randomly select any cross-term of the matrix and to automatically known (and record) all the existing physical constraints.

In conclusion, the block diagram of the entire *MDM* is schematically represented in Figure 26 and the steps of the *Phase Pivoting Algorithm - Version II* can be summarised as

1. Rank the cross-terms according to the magnitude $\left|F_{jk}\right| \sqrt{S^{ref}_{yy,jj} S^{ref}_{yy,kk}}$
2. Check and record the phase dependencies
3. Set the *Minimum Trace Conditions* for the biggest $(\ell - 1)$ cross-terms that simultaneously respect the phase dependencies (independent terms)
4. Retrieve the remaining $(\ell^2 - \ell)/2 - (\ell - 1)$ phases in accordance with the *Phase Pivoting Principle*

4.3.4 *Case study: three-drives six-controls simulated test*

The objective of this case study is to compare the two versions of the *Phase Pivoting Algorithm* (*Version I* and *Version II*), in order to point out the benefits in term of total power reduction achieved with the Version II.

As detailed above, the *Version I* has some drawbacks on deal with more than three controls. To highlight this limitation and the advantageous of the *Version II*, this case study presents the results of a three-drives six-controls simulated test. The procedure to simulate the control test is the same of the one proposed in Section 4.3.2. Therefore, Equation (10) is used to predict the input SDM, starting from the reference SDM and the corresponding system's mechanical impedance matrix. Moreover, the impedance matrix comes from real data in order to increase as much as possible the test realism. The setup used to estimate the impedance matrix from real data is shown in Figure 20. It is the same setup of the previous case study, with the main different that the three directions (X, Y and Z) of both the two three-axial accelerometer are considered as six-output responses. The two accelerometers are shown in Figure 20 with the label *Acc 1* and *Acc 2*, respectively. The FRFs matrix, shown in Figure 27, is estimated via H_1 estimator by performing a low level random test with decorrelated drives. The figure shows how the estimated FRFs matrix is rectangular (6-outputs x 3-inputs), therefore a pseudo-inverse operation is performed to calculate the impedance matrix ($\mathbf{Z} = \mathbf{H}^{\dagger}$).

For all the six control channels, the specification of the simulated test is a flat PSD with unitary amplitude in the frequency range $[10 - 2000]$ Hz. Figure

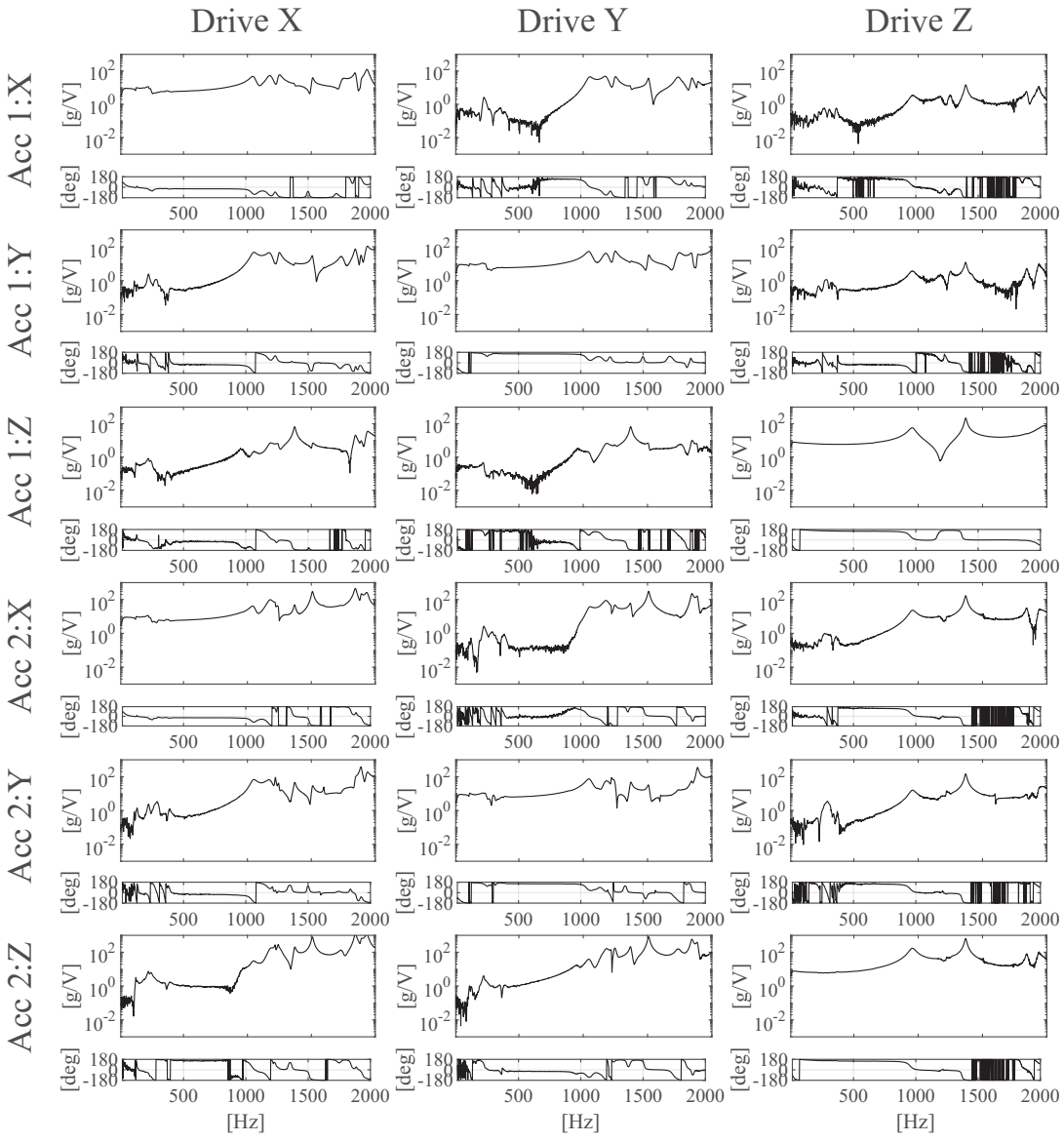

Figure 27: 6x3 FRFs matrix used in the three-drives six-controls simulated test.

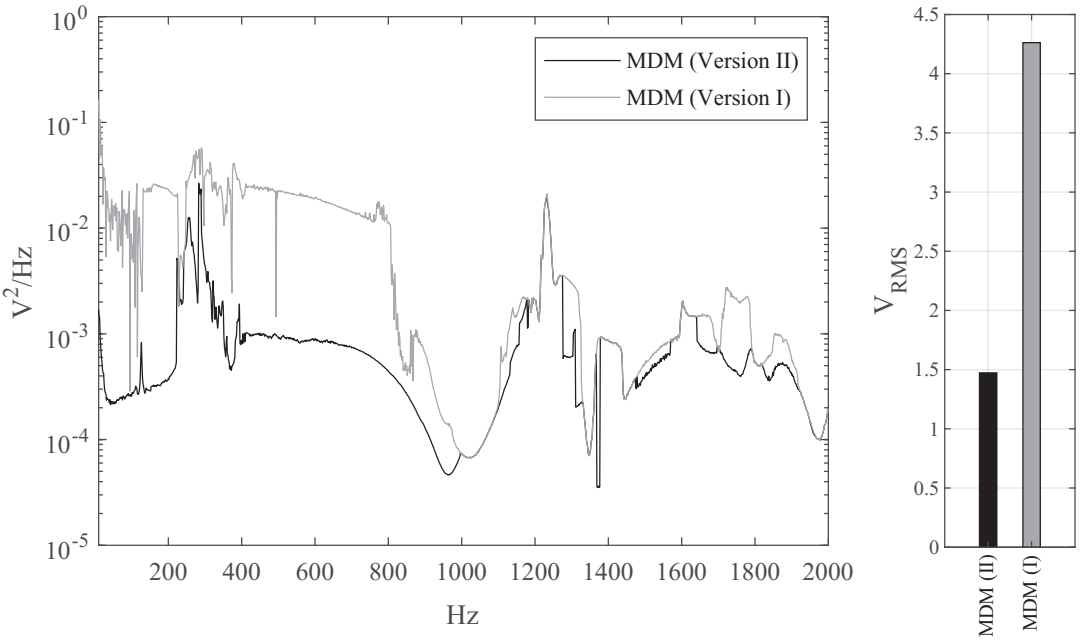

Figure 28: Three-drives six-controls simulated test: comparison between the *MDM* (*Phase Pivoting Algorithm - Version II*) and the *MDM* (*Phase Pivoting Algorithm - Version I*). Drives trace (left); RMS value (right)

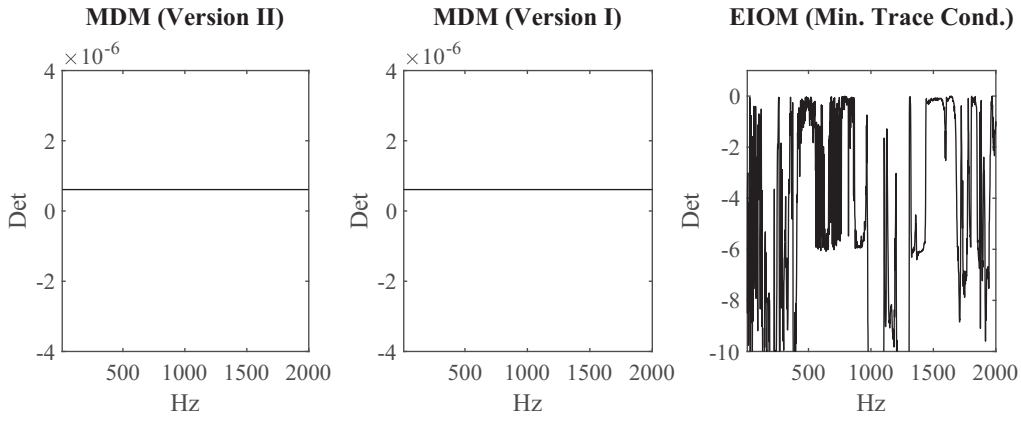

Figure 29: Three-drives six-controls simulated test: determinant of the reference SDM obtained with the *MDM* (*Phase Pivoting Algorithm - Version II*) (left), the *MDM* (*Phase Pivoting Algorithm - Version I*) (center) and the *EIOM* (*Minimum Drives Conditions*) (right).

28 shows the results in terms of drives power reduction obtained by the *MDM* with the two version of the *Phase Pivoting Algorithm*. The figure clearly highlights the benefits of the *Version II*. The drives trace provided by the Version II is orders of amplitude lower with respect to the Version I, especially up to 1000 Hz. In addition, Figure 28 shows the RMS values of the drives traces in a bar plot. *Version I* has an RMS value almost three times higher. Considering the RMS value as a global indicator of the total power reduction over the entire frequency bandwidth, these results point out the evident potential of the *Version II*. The novel method to select the independent terms, as the ones that contribute the most to minimize the drives trace, generates significant advantageous. Moreover, both the algorithms return positive definite reference SDM, as shown in Figure 29. The determinant of the reference matrices are both positive.

In conclusion, it is fundamental to notice that the only information needed for *MDM* is FRFs matrix, anyhow required for the vibration control algorithm and estimated during the System Identification, and the PSD profiles representing the test specifications. The target definition process is fully automated. Furthermore, the generated control targets incorporate information coming from the system identification, that could result in exciting the system in agreement with its dynamic behavior.

In the following of this thesis the *MDM* is intended with the integration of the *Phase Pivoting Algorithm - Version II*.

4.4 NOVEL SOLUTION: MINIMUM SINGLE DRIVE METHOD

The following section presents the *Minimum Single Drive Method* (*MSDM*) that is the second novel technique provided in this thesis to generate MIMO control targets.

The previously discussed procedure *MDM* takes the sum of the drives power as an indicator for the overall power required by the system and therefore it focuses the method on the drives trace minimisation. In this way, this technique tries to avoid DACs overloads by equally reducing all drives. However, due to the dynamic of the unit under test, it is possible that the power required by the excitation system for replicating the desired test specifications is mostly exploited by a single drive. In these cases, the strategy of equally reducing all the drives is not effective for preserving the excitation system. It is more

advantageous a method that better balances the overall power by pushing as much as possible the lightly stressed drives and relieving the overworked drive. The total power equally distributed between all the drives guarantees to fully exploit the excitation system capabilities in the safest way. Starting from the user defined test specifications, the aim of the *MSDM* is to find the proper values to be set for the cross-correlation between the reference channels that are able to minimise the power required by the overworked drive of the multi-input excitation system.

In the general case of m inputs and ℓ outputs, the PSDs of the input SDM are [60]

$$S_{uu,ii} = \sum_{j=1}^{\ell} \sum_{k=1}^{\ell} \hat{Z}_{ij} S^{ref}_{yy,jk} \hat{Z}'_{ik} \qquad \forall i = 1 : m \tag{40}$$

According to the (i-th) overworked drive to be minimised, Equation (40) can be rewritten as

$$S_{uu,ii} = \sum_{j=1}^{\ell} \sum_{k=1}^{\ell} S^{ref}_{yy,jk} \, G^{i}_{kj} \qquad \forall i = 1 : m \tag{41}$$

where matrix $\mathbf{G^i}$ is defined as

$$\mathbf{G^i} = \hat{\mathbf{Z}}^{\mathbf{H}}(:, i) \, \hat{\mathbf{Z}}(i, :) \qquad \forall i = 1 : m \tag{42}$$

Due to the Hermitian form of both $\mathbf{S^{ref}_{yy}}$ and $\mathbf{G^i}$, Equation (41) can be expressed as

$$S_{uu,ii} = \sum_{j=1}^{\ell} S^{ref}_{yy,jj} G^{i}_{jj} + 2 \sum_{j=1}^{\ell-1} \sum_{k=j+1}^{\ell} \mathrm{Re}\{S^{ref}_{yy,jk} G^{i}_{kj}\} \tag{43}$$

Therefore, the PSD of the overworked drive can be finally defined in terms of coherences and reference phases between the control channels as

$$S_{uu,ii} = \sum_{j=1}^{\ell} S^{ref}_{yy,jj} G^{i}_{jj} + 2 \sum_{j=1}^{\ell-1} \sum_{k=j+1}^{\ell} \gamma_{jk} \sqrt{S^{ref}_{yy,jj} S^{ref}_{yy,kk}} \left| G^{i}_{jk} \right| \cos(\phi_{jk} - \psi_{jk}) \tag{44}$$

PSD	
Hz	g^2/Hz
10	$1.04e^{-4}$
100	$1.04e^{-4}$
300	$5e^{-6}$
500	$2.08e^{-4}$
2000	$2.08e^{-4}$
$0.582\ g_{RMS}$	

Table 5: Breakpoints of the PSD profile used for test case A.

where

$$G^i_{jk} = \left|G^i_{jk}\right| e^{i\psi_{jk}} \tag{45}$$

Hence, the PSD of the (i-th) overworked drive is the minimum if

$$\begin{cases} \phi_{jk} = \psi_{jk} + \pi \\ \gamma^2_{jk} = 1 \end{cases} \qquad \forall j = 1:\ell,\ \forall k = 1:\ell,\ j \neq k \tag{46}$$

As previously explained, Equation (46) does not guarantee that the resulting reference SDM is positive (semi) definite. To overcome this limitation, the *MSDM* can be completed following the *phase pivoting principle* proposed by the *MDM*: the minimum (i-th) drive conditions are applied for the $(\ell - 1)$ independent terms with the biggest amplitude $|G^i_{jk}|\sqrt{S^{ref}_{yy,jj} S^{ref}_{yy,kk}}$ and the remaining terms must be retrieved by respecting the existing phase dependencies.

4.5 TEST CAMPAIGN

A test campaign is carried out by using the three-axial electrodynamic shaker Dongling 3ES-10-HF-500 at the University of Ferrara. The advanced excitation system is described in detail in Chapter 3. The Siemens SCADAS Mobile SCM202V (V8 input and DAC4 output modules) is used as data acquisition system and MIMO Random of Simcenter Testlab as vibration control software.

Figure 30: Test campaign setup: three-axial electrodynamic shaker at the University of Ferrara (left); bare head expander sensor configuration (right-top); Siemens SCADAS Mobile SCM202V (right-bottom).

The test campaign is performed on the bare HE with the sensor configuration shown in Figure 30, i.e. two tri-axial accelerometers named 1 and 2. In order to compare and to better highlight the capability of each procedure, three test cases are carried out considering different test set-up (different number of the control channels, different test specifications). The test specifications are provided in terms of PSDs coming from Standards and the reference SDM is fulfilled by applying the previously described methods. Furthermore, the test results are compared with the results obtained from the most commonly practised target generation procedure in MIMO random control testing: the *Independent References Method (IRM)*. When no information about the CSD terms is known, the common option is to specify the reference SDM as a diagonal matrix by simply setting low coherence ($\gamma_{jk} = 0.05$) for all the cross terms [4]. It is worth noticing that all the results are shown for normal end tests, i.e. full level successfully run for 1 min within the abort limits.

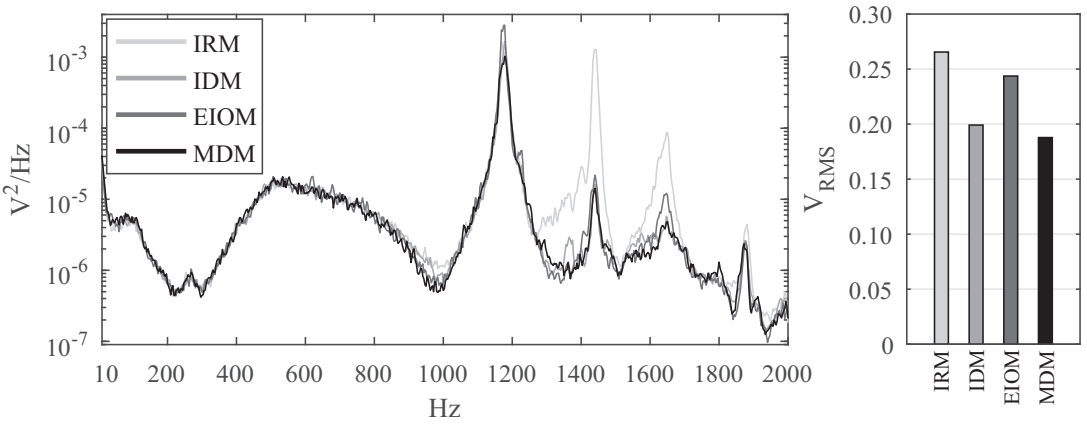

Figure 31: Test case A: drive trace results for the state-of-the-art solutions.

4.5.1 *Test case A*

Test case A is a three-drives three-controls test case. The reference control channels are the X, Y and Z axes of the tri-axial accelerometer 1 shown in Figure 30. The PSD shape comes from single axis test specification [11] with the breakpoints reported in Table 5 has a frequency range of [10-2000] Hz and a frequency resolution of 3.125 Hz. The same PSD profile is considered as test specification for all the reference control channels.

A first analysis addresses the comparison of the state-of-the-art drives power reduction procedures (*IDM, EIOM* and *IRM*) with respect to the proposed *MDM*. The drive traces resulting from the normal end tests are shown in Figure 31. As expected, the *IRM* is the method that requires the highest power level to reach the test specifications. This procedure, by simply setting low coherence between the reference channels, very often turns to be overly conservative near frequencies dominated by a single mode. The result is a overly large drives trace in some frequency bands with the danger of over-stressing the test excitation system. The results of the drive traces in terms of V_{RMS} give a useful insight of the drives power reduction capability of each procedures. The gap between the *EIOM* and the *MDM* is significant: a power reduction of 8% and 29% compared to the *IRM*, respectively. This difference derives from the different approaches adopted by the two procedures to fix the problem of obtaining a positive (semi)definite reference SDM starting

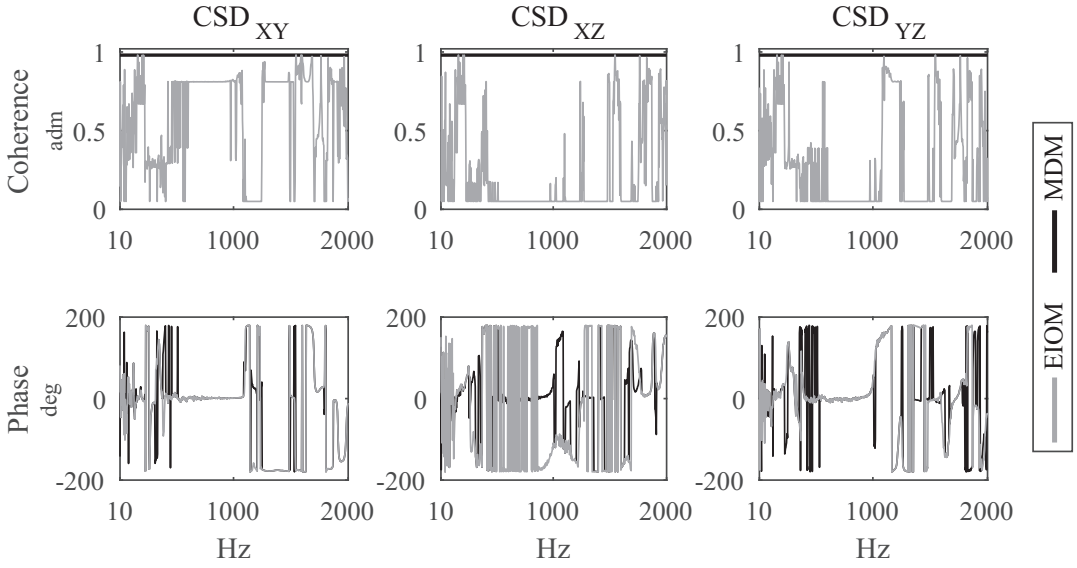

Figure 32: Test case A: reference coherences and reference phases obtained from the *MDM* (black curves) and from the *EIOM* (gray curves).

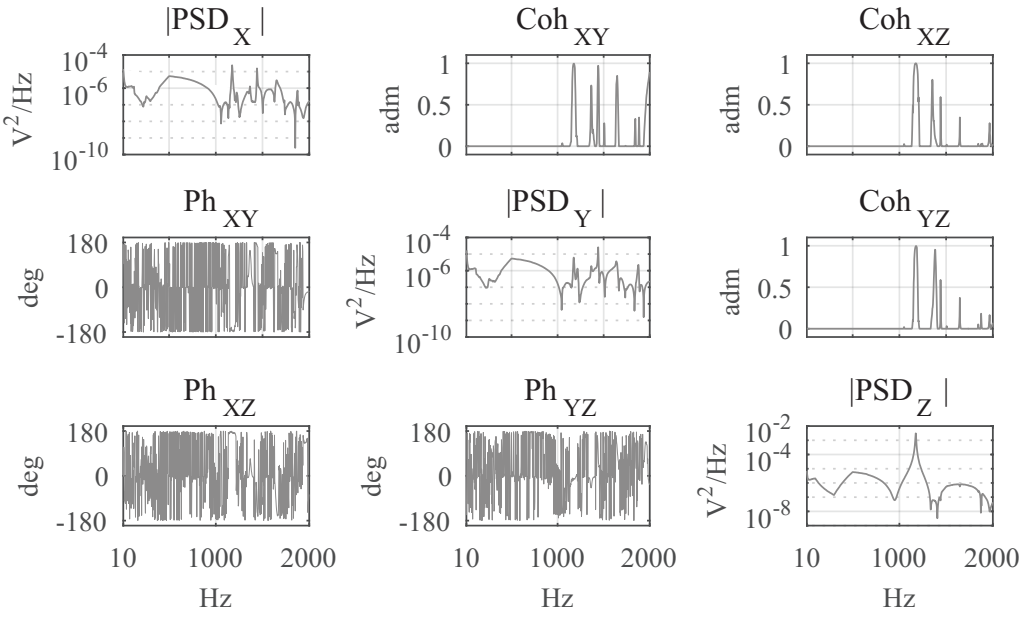

Figure 33: Test case A: input SDM obtained from the IDM.

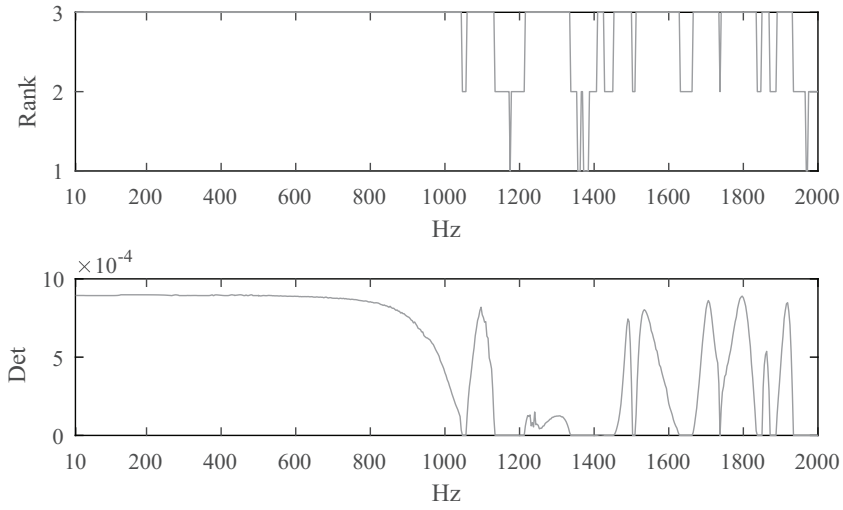

Figure 34: Test case A: rank of the reference SDM obtained from the IDM (top); determinant of the reference SDM obtained from the IDM (bottom).

from the minimum drives trace conditions of Equation (28). The two different approaches are outlined in Figure 32 that shows the reference coherences and the reference phases obtained from the two procedures. The *EIOM* fixes the reference phases in accordance with the conditions of Equation (28) and decreases the coherence values with the constrained optimization routine until the reference SDM is positive (semi)definite. In some cases, in order to verify the constrain, the coherences are forced to low values that nullify the phases role. In these cases, the CSD terms have no beneficial effect on the drives power reduction. On the contrary, the *MDM* keeps fully coherent controls and adapts one of the three phases resulting from Equation (28) by following the *phase pivoting principle*. For each spectral line, by properly choosing the phase to be adapted, the *MDM* is able to take full advantage of the minimum drives trace conditions and it guarantees the highest drives power reduction possible.

Figure 31 also highlights the excellent results obtained from the *IDM*: a power reduction of 25% compared to the *IRM*. The input SDM used to drive the excitation system is shown in Figure 33. The input SDM corresponds to the drives from the MIMO controller to the amplifiers setted with the same gain factor. Figure 33 highlights that at some frequencies it is not possible to replicate the test specifications with decorrelated inputs. The peaks in the

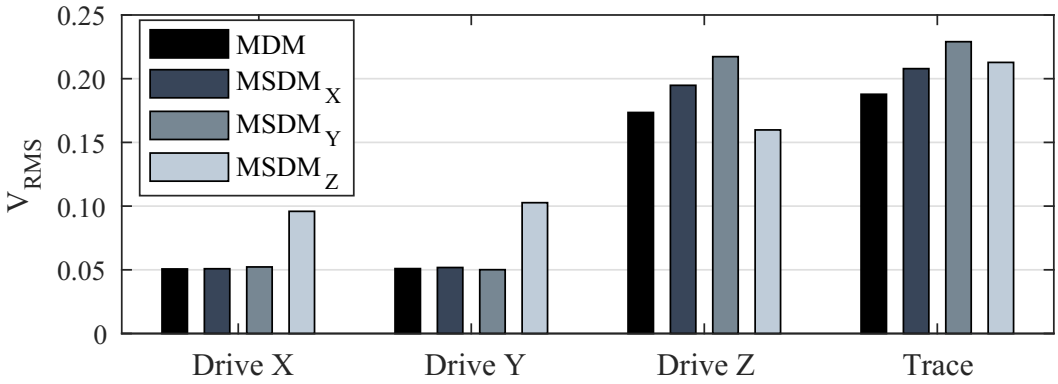

Figure 35: Test case A: RMS drives power comparison between the *MDM* and the *MSDM*.

coherence sub-plots underline that the correction of the negative values of input vector X (Equation (36)) has been done (almost independent drives). However, it is worth underlining that the correction of the negative values of input vector X with zero, inevitably generates a diagonal matrix with at least one zero on the diagonal. This implies that the column vectors (or the row vectors) of the matrix are linearly dependent. The determinant of the input SDM is zero and the matrix is rank deficient. Then, the rank of the reference SDM computed via Equation (35) is [60]

$$\operatorname{rank}(\mathbf{S}_{\mathbf{yy}}^{\mathbf{ref}}) \leqslant \min\left[\operatorname{rank}(\mathbf{H}), \operatorname{rank}(\mathbf{S}_{\mathbf{uu}})\right] \tag{47}$$

Figure 34 confirms that, at some frequencies, the reference SDM is rank deficient and positive semi-definite ($\det(\mathbf{S}_{\mathbf{yy}}^{\mathbf{ref}}) = 0$).

Finally, the proposed procedure on the single drive power minimisation (*MSDM*) is compared to the *MDM*. Figure 35 shows the resulting RMS power levels for each drive and for the drives trace when the *MSDM* is applied for minimising the power of Drive X (dark-gray bars), of Drive Y (gray bars) and of Drive Z (light-gray bars). For this particular test case, the $MSDM_Z$ is certainly the most interesting application because about 60% of the total power required by the excitation system is spent for driving the Drive Z. In this sense, the $MSDM_Z$ that minimises the overworked drive by fairly spreading the drives power is more advantageous than the *MDM* that equally minimises the power

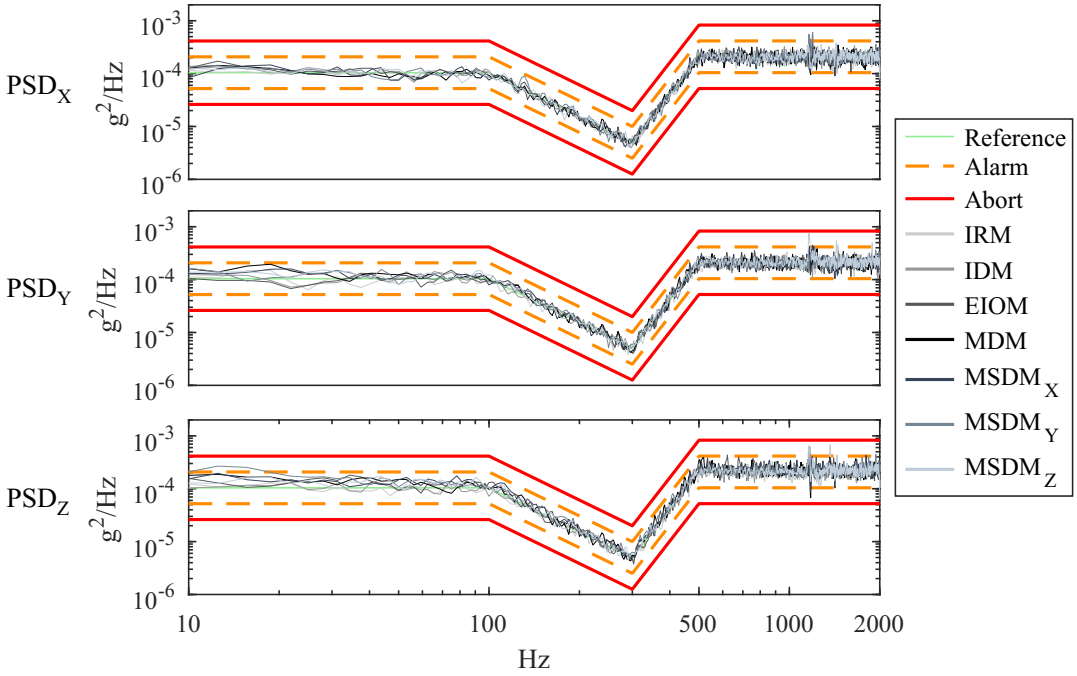

Figure 36: Test case A: MIMO random control results. The solid red lines and the dashed orange lines are the abort and the alarm thresholds fixed at ±6dB and ±3dB from the reference, respectively

of each drive. By comparing the two procedures, the power reduction on the Drive Z is 8%.

Figure 36 shows the control channel results for all the procedures. All the runs are normal end tests, i.e. no spectral line exceeds the abort thresholds (red lines) fixed at ±6dB from the reference.

4.5.2 *Test case B*

In order to better highlight the applicability field of the studied methods, test case B is intended to be an example where no MIMO target generation procedure has beneficial effects on reducing the drives power. It is a three-drives three-controls test case, where the reference control channels are the X, Y and Z axes of the triaxial accelerometer 2 shown in Figure 30. The test specifications come from single axis Standard [4] with the breakpoints

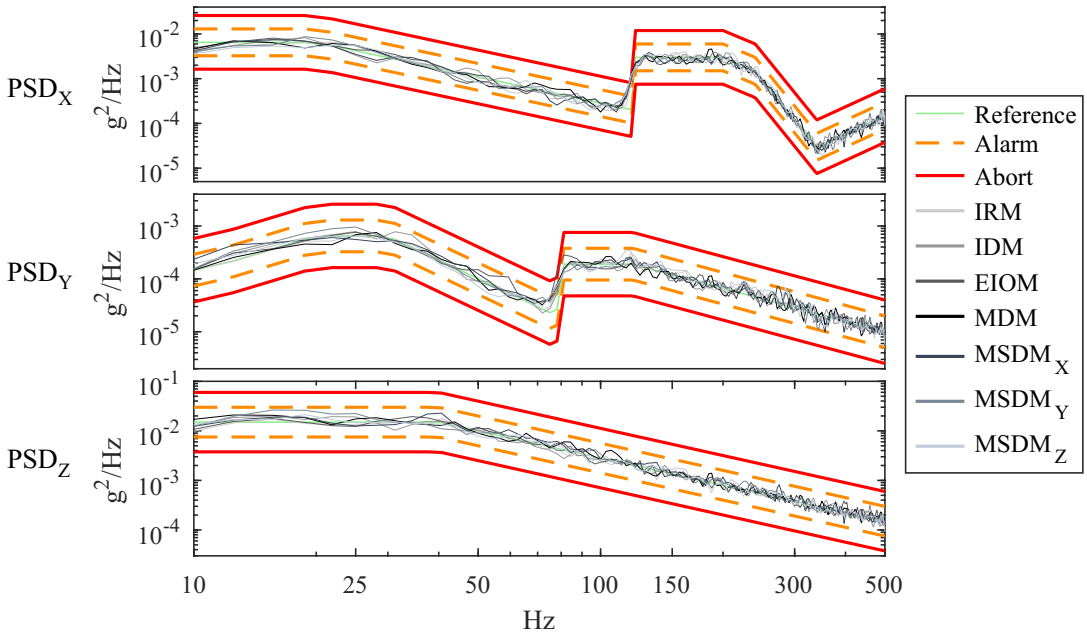

Figure 37: Test case B: MIMO random control results. The solid red lines and the dashed orange lines are the abort and the alarm thresholds fixed at ±6dB and ±3dB from the reference, respectively.

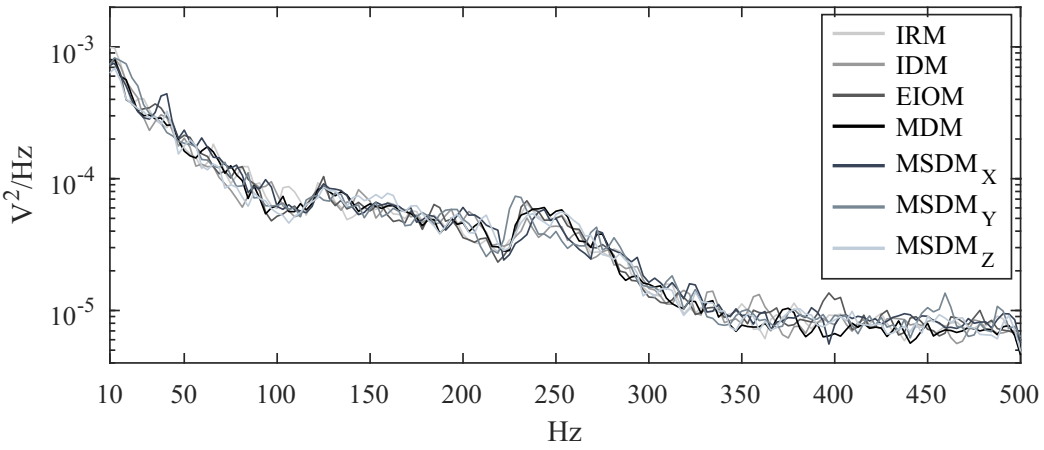

Figure 38: Test case B: drives trace results.

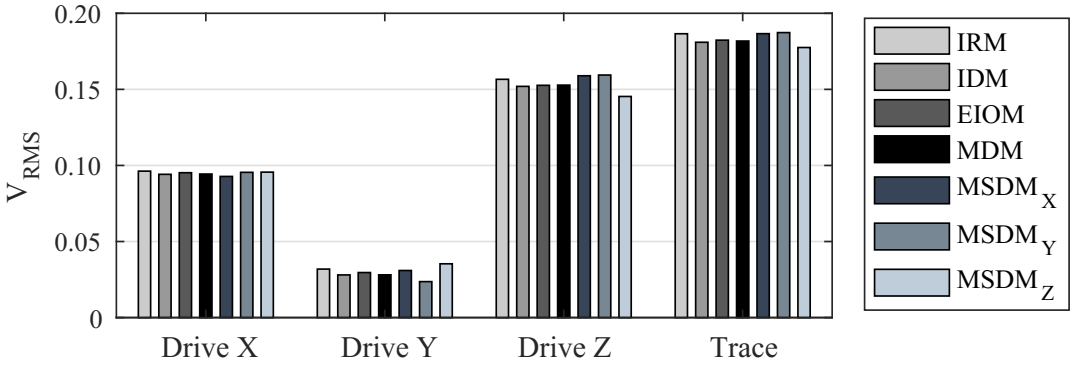

Figure 39: Test case B: RMS drives power comparison.

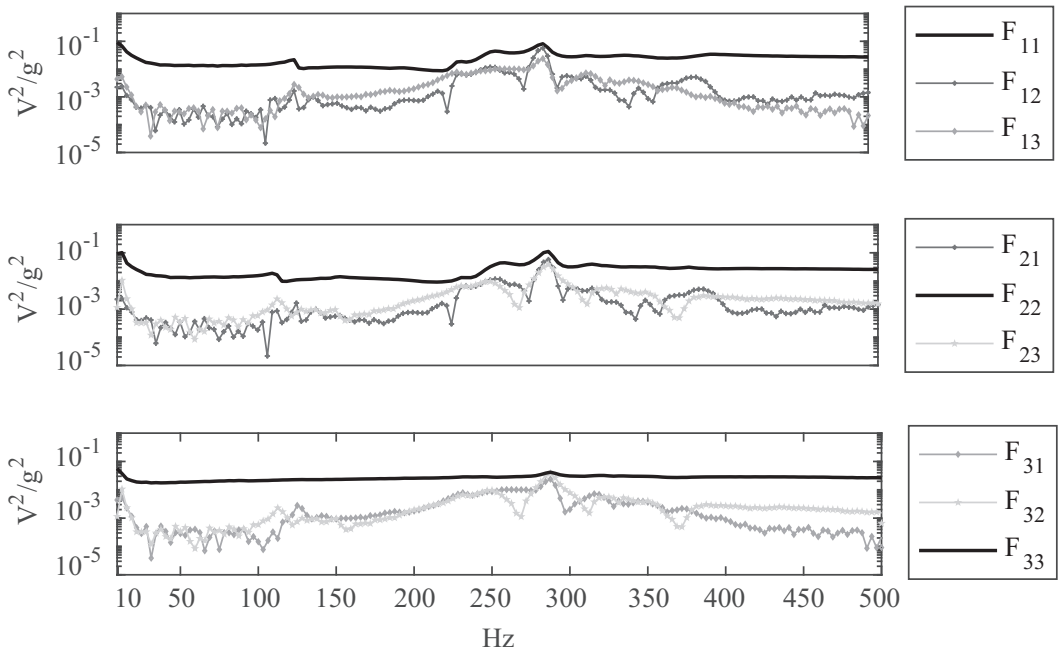

Figure 40: Test case B: matrix $\mathbf{F} = \hat{\mathbf{Z}}^{\mathbf{H}}\hat{\mathbf{Z}}$.

Table 6: Breakpoints of the PSD profiles used for test case B.

PSD_X		PSD_Y		PSD_Z	
Hz	g^2/Hz	Hz	g^2/Hz	Hz	g^2/Hz
10	$6.5e^{-3}$	10	$1.3e^{-4}$	10	$1.5e^{-2}$
20	$6.5e^{-3}$	20	$6.5e^{-4}$	40	$1.5e^{-2}$
120	$2.0e^{-4}$	30	$6.5e^{-4}$	500	$1.5e^{-4}$
121	$3.0e^{-3}$	78	$2.0e^{-5}$		
200	$3.0e^{-3}$	79	$1.9e^{-4}$		
240	$1.5e^{-3}$	120	$1.9e^{-4}$		
240	$3.0e^{-5}$	500	$1.0e^{-5}$		
500	$1.5e^{-4}$				
0.74 g_{RMS}		0.20 g_{RMS}		1.04 g_{RMS}	

reported in Table 6. The PSD profiles have a frequency range of [10-500] Hz and a frequency resolution of 3.125 Hz.

The control channels results for the normal end tests are shown in Figure 37. The resulting drive traces and the RMS drives power comparison are reported in Figure 38 and Figure 39, respectively. It can be noted that there is no significant differences in terms of power reduction between the adopted procedures. The power required by the excitation system for replicating the test specifications is essentially the same, independent the applied method. This can

Table 7: Breakpoints of the PSD profile used for the test case C.

PSD	
Hz	g^2/Hz
10	$2.60e^{-5}$
50	$1.51e^{-4}$
2000	$1.51e^{-4}$
0.547 g_{RMS}	

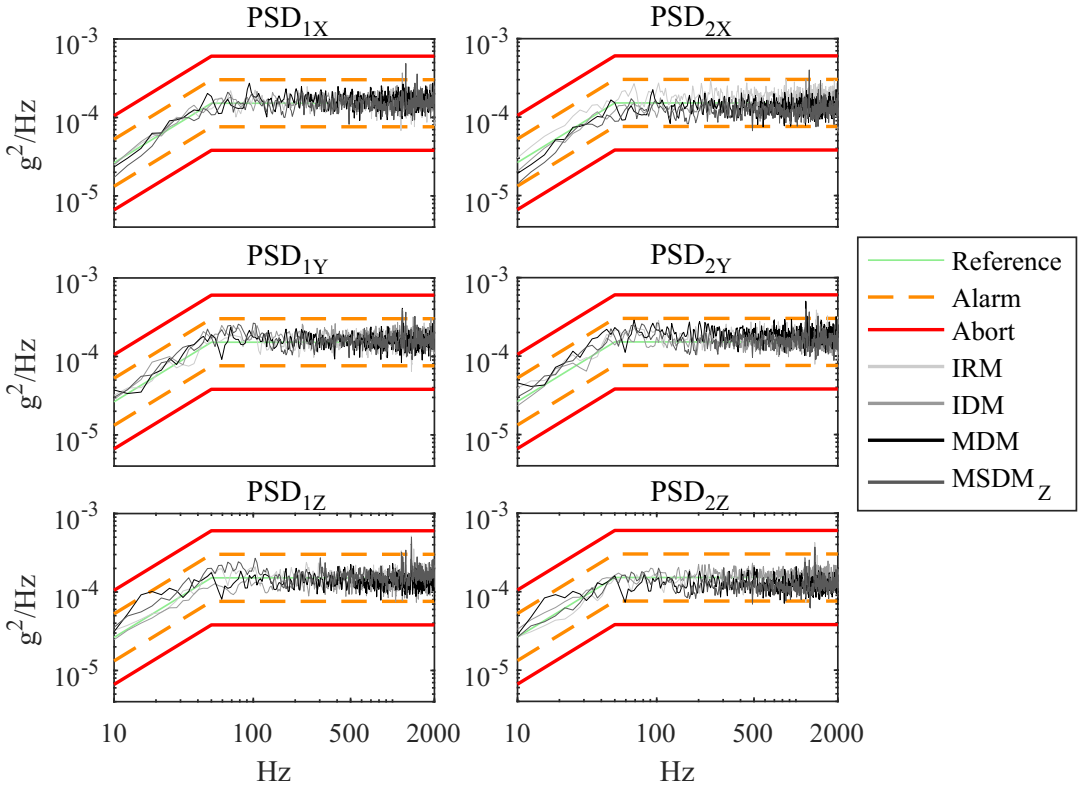

Figure 41: Test case C: MIMO random control results. The solid red lines and the dashed orange lines are the abort and the alarm thresholds fixed at ±6dB and ±3dB from the reference, respectively.

be explained by looking at the amplitudes of the **F** matrix terms plotted in Figure 40. Except for the narrowband around 300 Hz, in the entire bandwidth the diagonal terms of the matrix (black curves) are orders of magnitude above the off diagonal ones, meaning that $\hat{\mathbf{H}}$ is almost diagonal. Therefore, by referring to Equation (25), the cross terms hold a negligible role and the overall power required by the exciters is not affected by the choice of coherences and phases.

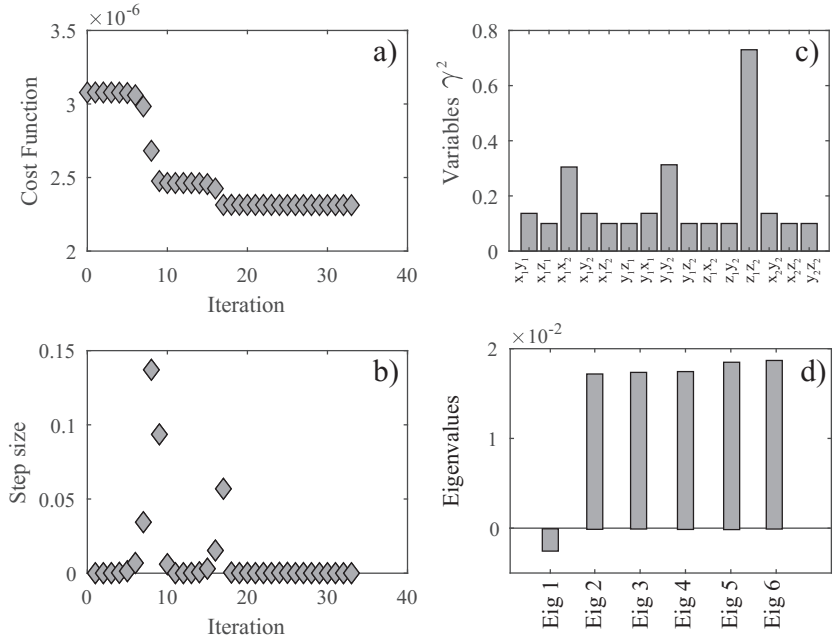

Figure 42: Test case C: results of the constrained optimization routine adopted in the *EIOM* at 600 Hz. a) cost function values; b) step size values; c) coherence values obtained at the 34th iteration; d) eigenvalues of the reference SDM obtained at the 34th iteration.

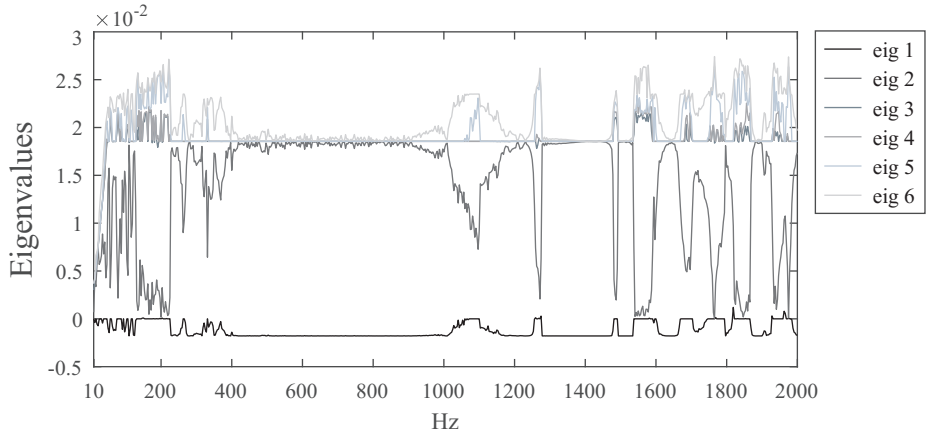

Figure 43: Test case C: eigenvalues of the reference SDM obtained from the *EIOM*.

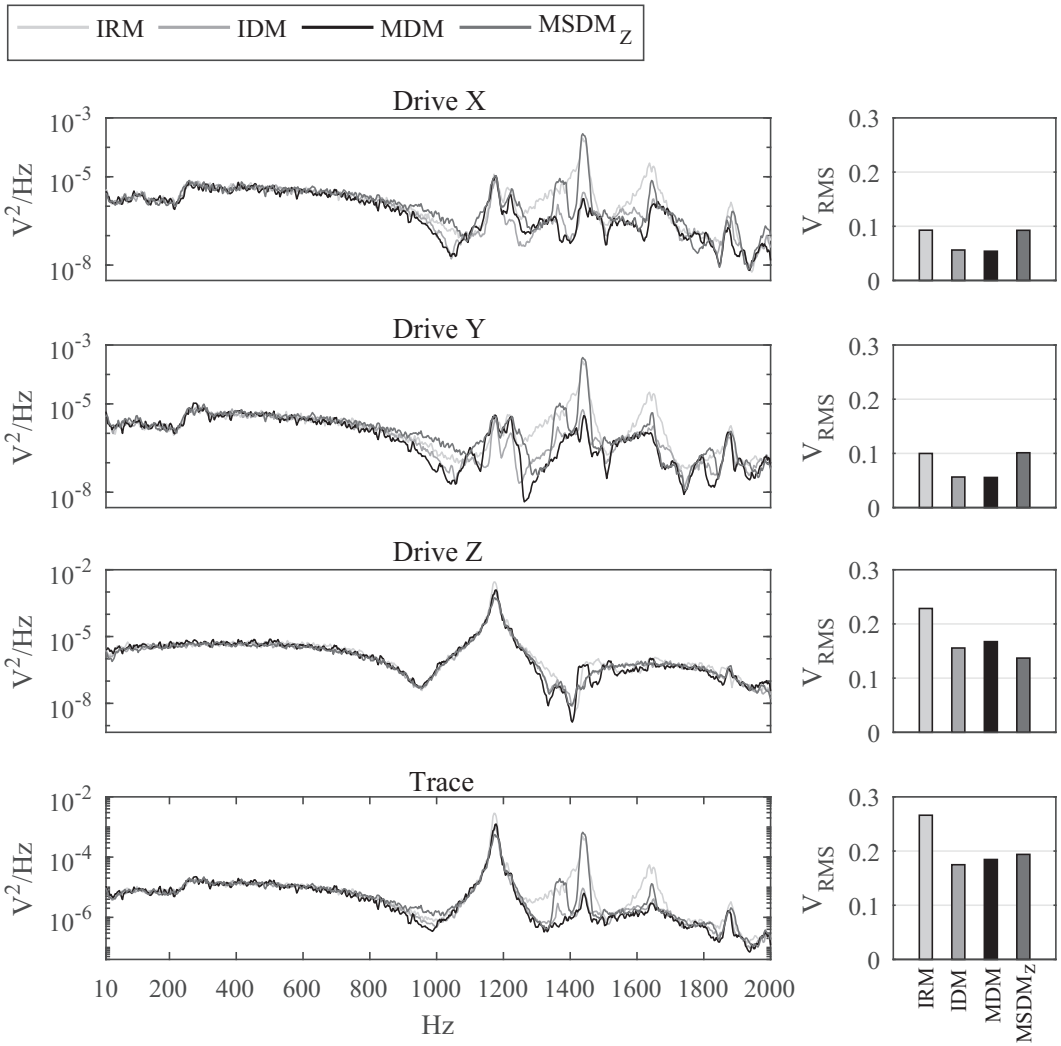

Figure 44: Test case C: comparison on the drives power reduction.

4.5.3 *Test case C*

Test case C is a three-drives six-controls test case. The reference control channels are X, Y and Z axes of the triaxial accelerometers 1 and 2 shown in Figure 30. A standard "blue-white noise" PSD profile, reported in Table 7, is considered as test specification for all the reference control channels. The frequency range is [10-2000] Hz and the frequency resolution is 3.125 Hz.

Figure 41 shows the control results of the six reference channels for the normal end tests. It can be noted that no results are presented for the *EIOM*. Due to the high complexity of the six controls test case, the basic optimization routine adopted in the *EIOM* at some frequencies does not converge to a feasible solution and the resulting reference SDM cannot be used for the actual control test. A practical example is given in Figure 42 that shows the results of the constrained optimization routine at 600 Hz. In particular, Figure 42 a) and b) illustrate the values of the cost function per iteration and the corresponding step size; Figure 42 c) and d) show the coherence values and the eigenvalues of the reference SDM obtained at the last iteration. As can be seen, after 34 iterations the optimization converges to a solution that does not satisfy the constraint, i.e. the minimum eigenvalue of the resulting reference SDM is negative. Since the sizes of the reference SDM quadratically increase with the number of controls, the constrained optimization algorithm has to manage a 6x6 matrix by matching the 15 coherence variables in countless combinations per spectral line. As also highlighted in Figure 43, the minimum eigenvalue of the reference SDM (black curve) results negative for most of the bandwidth. Therefore, the control target is negative definite and it cannot be use for the actual control test. This test case clearly highlights the *EIOM* limitations when the number of control channels increases.

The comparison with respect to the drives power reduction is illustrated in Figure 44. The test results confirm the outcomes obtained in test case A. Considering the RMS values of the drives trace as an indicator for the global power reduction, both the *IDM* and the *MDM* have significant beneficial effects: a power reduction of 34% and 31% with respect to the standard *IRM*, respectively. It is also worth emphasising that, for this particular application, the *MDM* cannot fully exploit its potential. In case of fully coherent control responses, since the excitation system is a 3 DOF shaker, the control channels pairs along the same axis need to be set in phase. This physical constraint on

the reference phases setting, inevitably affects the choice of the independent terms on which the minimum drives trace conditions (Equation 28) can be applied.

Concerning the proposed procedure on the single drive power minimisation, the $MSDM_Z$ guarantees an extra power reduction on the overstressed Drive Z of 9% and 14% compared to the *IDM* and the *MDM*, respectively. Moreover, since the Drive Z spends over half of the total power required by the excitation system, the $MSDM_Z$ also ensures remarkable results on the drives trace power reduction.

4.6 CONCLUDING REMARKS

This chapter compares and critically analyses the currently available procedures for reducing the drives power in multi-axis random control testing. Moreover, two novel solutions are proposed (*MDM* and *MSDM*). Both are innovative fully automatic target definition procedure which can be adopted in cases where the set of operational measurements is missing and/or test specifications are provided in terms of PSDs only. With the developed procedures, it is possible to generate the missing CSDs in such a way that the reference SDM is positive semi-definite in the whole test bandwidth and the resulting drives power is minimally reduced.

These advantages have been shown through a series of tests with different number of control channels (three and six) and different test specifications. The test campaign has been carried out using a three-axial electrodynamic shaker, highlighting significant differences on the capabilities of each MIMO target generation algorithm. In particular, the *EIOM* has shown inherent limitations due to the integration of a constrained optimization routine inside the algorithm. The strategy of lowering the coherence values to verify the constrain, results to be ineffective in terms of drives power reduction. Moreover, the convergence to a feasible solution is not always guaranteed and the user experience could be strictly needed to tune the converge parameters. Additionally, since an iterative routine is involved in the process, the computational costs and the computational time significantly increase with the number of variables in the process, making the *EIOM* not suitable when the number of control channels increases.

The present *MDM* overcomes the *EIOM* flaws. By keeping high coherent control responses and by adapting the reference phases, this fully automatic procedure quickly provides a reference SDM that guarantees high control performances and typically the best drives power reduction results. It is important to point out that the *MDM* can fully exploit its potential if there is one to one correspondence between the directions of the control responses and the DOFs of the excitation system.

The *IDM* instead, drives the excitation system with uncorrelated inputs and it ensures drives power reduction results mostly comparable to the *MDM* ones. However, in order to overcome the problem of test specifications not reachable with uncorrelated inputs, the solution adopted by the *IDM* generates rank deficient reference SDM.

Finally, when the power required by the excitation system is mostly exploited by a single drive, it is disadvantageous to equally minimise all the drives. In this sense, the *MSDM* is able to guarantee an extra power reduction on the overworked drive by better balancing the overall power.

It can be concluded that, with the *Minimum Drives Method* the drives power needed to reach the test specifications is globally reduced with respect to other possible state-of-the-art solutions. With the *Minimum Single Drives Method* instead, the overstressed drive of the multi-input excitation system is reduced. For both the methods, the requirement of acceptable narrowband control performance is fulfilled, incorporating information about the system dynamics directly in the control target (without additional measurement effort). Compared to standard choices or methods currently used to fill in the CSDs, the added value of reducing the total drives power is undoubtedly advantageous: for fixed test response levels, it guarantees that the delicate and expensive excitation hardware (shakers and amplifiers) is driven with reduced voltages. In case the test levels need to be increased, the methods would allows a maximum scale factor. These features open the possibility to candidate the proposed methodologies as attractive solutions to the problem of meeting *the minimum drives criteria* and therefore to be included in the current standard practice for multi-axial testing.

5

MIMO TARGET GENERATION TECHNIQUE FOR DYNAMIC RESPONSE MAXIMIZATION

5.1 INTRODUCTION

Industrial products are subjected to extreme conditions of the surrounding environment throughout their entire life. Severe environment conditions may seriously deteriorate the components durability, therefore the environmental effects must be taken into account from the early stages of development. The capability to withstand such adverse conditions is assessed during the product design process by means of laboratory testing that aims to reproduce the characteristics of the real environment.

Typically, the laboratory tests force the specimen to work in high severity environmental conditions that are accelerated in order to speed up the testing process. Within this framework, accelerated random vibration tests represent a powerful testing procedures to evaluate the fatigue life characteristics of the specimens, overcoming the time cost limitations. The most widely used techniques to correlate the laboratory test condition to the operational one, is the so-called inverse power law [64, 65]

$$\frac{T_2}{T_1} = \left(\frac{a_1}{a_2}\right)^b \tag{48}$$

where the left-hand side is the ratio between the desired duration of the accelerated test and the expected life of the component in the operative environment; the right-hand side addresses the ratio between the RMS value of

the acceleration in the operative conditions and the one to be applied in the laboratory to accelerate the test. Theoretically, the exponent b should represent the slope of the material *S-N* curve in logarithmic coordinates. However, the scaling law of Equation (48) is a simple approximation of the fatigue behaviour of complex structures and therefore it includes some limitations. To overcome these inherent uncertainties, the exponent b is actually an empirical factor. Typical values of the exaggeration factor b are provided by Standards [4, 5] as a function of the severity of the environment to which the item must undergo. As widely explained in the previous chapters, such Standards promote the test tailoring practice, consisting of guidelines to synthesize a vibration profile starting from experimental measurement of the excitation present in the operational environment. It worth noticing that although they may provide useful indication, there is still a consistent risk to obtain an unrepresentative test [66]. Nowadays, the most accredited tailoring procedure is the one proposed by Lalanne in [67], based on the adoption of two frequency spectra, namely the *Extreme Response Spectrum* (ERS) and the *Fatigue Damage Spectrum* (FDS), as metrics to compare the damage introduced by the synthesized excitation to the vibration acting in working conditions. Basically, the excitation applied on the test specimen should be the one capable to reproduce the same level of damage to which the specimen would undergo in its life-cycle [68].

The accuracy of the inverse power law has been investigated in several works, since its relevance is pivotal to synthesize reliable test specifications [69]. The theoretical foundations were addressed by Allegri and Zhang [70] that proposed an extended formulation of the law capable to address the effects of multi-axiality of the stress state. The feasibility of the law, aroused the interest of many authors, which experimentally verified the limits of the actual formulation [71]. Despite Equation (48) is nowadays widely applied in the industrial practice, the methodology is still affected by limiting hypotheses. As the strongest assumption, the device under test is approximated as a single degree of freedom system where the stress is considered proportional to the relative displacement between base and mass. Such an assumption totally neglects the possibility of multi-axis excitation testing and thus the current standards on accelerated dynamic tests are commonly intended to be implemented on single-axis shakers.

Within this context, the main objective of this chapter is to investigate the impact that simultaneous multi-axis excitations can cause on the specimen's

fatigue life. More specifically, the research activity presented in this chapter point out the relevance of the adopted MIMO target generation technique for performing the multi-axis accelerated fatigue test. The work clearly highlights that different combinations of the multiple test specifications can drastically alter the fatigue behaviour and the failure mode of the specimen under test. In this sense, the chapter presents a novel MIMO target generation technique, namely *Extreme Dynamic Response Method* (*EDRM*). This technique can be exploited when the test specifications are provide in terms of PSDs only and no information about the CSDs is available. The *EDRM* combines the test specifications in order to get out the maximum dynamic responses from the specimen under test by fully exploiting the total energy used for exciting the structure. This MIMO target technique guarantees to excite the specimen with the most adverse and extreme multi-axis vibration conditions, thus it assurances the minimum Time to Failure (TtF).

The *EDRM* is theoretically explained in Section 5.3 and experimentally compared with respect to the other available MIMO target generation techniques in Section 5.4.2. In order to reach the purpose of the study, a dedicated experiment has been designed and performed on the 3 DoF electrodynamic shaker at the University of Ferrara, involving 48 tests on custom aluminium alloy specimens. Section 5.4.1 is devoted to the description of the experimental setup. Section 5.4.3 present the results and the discussion of the entire fatigue test campaign. Eventually, Section 5.5 is devoted to concluding remarks.

5.2 FATIGUE DAMAGE IN FREQUENCY DOMAIN: BASIC THEORY

5.2.1 *Damage model for Gaussian random stress*

The fatigue strength curve of a material may be represented by the S-N curve, where the finite life region is well described by the Basquin's law [72]

$$N\sigma^k = C \tag{49}$$

In the framework of variable amplitude fatigue, the well-known Palmgren-Miner's rule [73] estimates the accumulation of damage until the occurrence of failure

$$D = \sum_i \frac{n_i}{N_i} \tag{50}$$

where n_i are the number of cycles actually imposed to the material with a stress amplitude σ_i. Conventionally, failure occurs when $D = 1$, that is when the number of applied cycles n_i equals the maximum acceptable number of cycles N_i for the material.

The substitution of Equation (49) into Equation (50) leads to the following expression of damage accumulation

$$D = \sum_i \frac{n_i \sigma_i^k}{C} \tag{51}$$

which can be further reworked for a time-invariant time history in the following integral form [74]

$$D = \frac{n_a T}{C} \int_0^{+\infty} \sigma^k p_a(\sigma)\, d\sigma \tag{52}$$

The formula describes the damage accumulation observable, on average, for a random stress time history for which it is known its duration T and the probability density distribution of the counted cycles $p_a(\sigma)$. The probability distribution depends upon the cycle counting method considered, where the rainflow has demonstrated itself to be the most suitable one in a wide variety of usage cases [75]. Unfortunately, the complexity of the algorithm is such that an exact expression does not exist yet, but several approximations have been obtained.

If the random stress is represented in the frequency domain (e.g. by means of its PSD), the approximations of p_a can be distinguished by the bandwidth involved. For the particular case in which the stress can be considered time-invariant, Gaussian and narrowband, the probability density distribution associated to the rainflow counting assumes the following form

$$p_a(u) = \frac{u}{\lambda_0} \exp\left(-\frac{u^2}{2\lambda_0}\right) \tag{53}$$

where λ_0 is the zeroth order moment of the PSD. In general, coefficients λ_i are the statistical moments of a PSD and are calculated as

$$\lambda_i = \int_0^{+\infty} (2\pi f)^i S_{xx}(f)\, df \tag{54}$$

in which index $i \in \mathbb{N}$. PSD moments are linked to the statistical properties of a stochastic process: for example the zeroth moment previously introduced for the stress PSD corresponds to the variance of the stress distribution.

Other useful parameters, frequently encountered in fatigue analysis of random loads, are obtainable from PSD moments [76]. The expected number of zero up-crossing per second is calculable as

$$n_0^+ = \sqrt{\frac{\lambda_2}{\lambda_0}} \tag{55}$$

rather the expected number of peaks per second is

$$n_p^+ = \sqrt{\frac{\lambda_4}{\lambda_2}} \tag{56}$$

and the spectral width parameter is

$$\alpha_i = \frac{\lambda_i}{\sqrt{\lambda_0 \lambda_{2i}}} \tag{57}$$

By substituting Equation (53) into Equation (52), and noting that for a narrowband process the average number of stress cycles per second n_a equals the average number of zero crossings with positive slope n_0^+, the expression of damage accumulation [77] may be obtained:

$$D = \frac{n_0^+ T}{C} \left(\sqrt{2\lambda_0}\right)^k \Gamma\left(1 + \frac{k}{2}\right) \tag{58}$$

where Γ is the gamma function introduced by Euler. The expression is the exact solution of Equation (52) for the particular case of a narrowband stress process. In the case of wideband stress process the most commonly used frequency domain counting methods are *Dirlik* [78] and *Tovo-Benasciutti* [74].

5.2.2 *Multi-axial fatigue criteria*

In accordance with the frequency domain transfer function relationship shown in Chapter 2 that links the inputs and the outputs in the the general case of

MIMO linear systems, it is always possible to relate the MIMO control target with the stress responses of the specimen under test as

$$\mathbf{S}_{\sigma\sigma} = \hat{\mathbf{H}}_{\sigma a}\, \mathbf{S}_{yy}^{ref}\, \hat{\mathbf{H}}_{\sigma a}^{H} \tag{59}$$

where $\mathbf{S}_{\sigma\sigma}$ is the 6x6 stress SDM of the stress-tensor ($\sigma = [\sigma_{xx}, \sigma_{yy}, \sigma_{zz}, \tau_{xy}, \tau_{xz}, \tau_{yz}]$) defined in frequency domain as

$$\mathbf{S}_{\sigma\sigma} = E[\sigma\sigma^{T}] = \begin{bmatrix} S_{\sigma\sigma,xx} & \cdots & S_{\sigma\sigma,xx/yz} \\ \vdots & \ddots & \vdots \\ S_{\sigma\sigma,yz/xx} & \cdots & S_{\sigma\sigma,yz} \end{bmatrix} \tag{60}$$

Objective of any multi-axial fatigue criterion is to convert the multi-axial stress state of Equation (60) to an equivalent uni-axial one to be used as input of the fatigue damage model of Equation (58) or as equivalent stress level for defining the S-N curve. Several multi-axial fatigue criteria have been proposed in the recent past [79, 80]. Mršnik et al. in [25] theoretically and experimentally compares some of them, i.e. *maximum normal and shear stress* [81], *Preumont and Piefort* [82], *Carpinteri-Spagnoli* [83] and *Projection-by-Projection* [84].

In the following of this chapter the *Preumont and Piefort* approach will be used to define the equivalent uni-axial stress state. The method is based on the von Mises stress concept. In frequency domain, the von Mises PSD can be defined in the matrix form as [85, 86]

$$S_{vM} = Tr[\mathbf{Q}\mathbf{S}_{\sigma\sigma}] \tag{61}$$

were matrix $\mathbf{Q}$ is given by

$$\mathbf{Q} = \begin{bmatrix} 1 & -0.5 & -0.5 & 0 & 0 & 0 \\ -0.5 & 1 & -0.5 & 0 & 0 & 0 \\ -0.5 & -0.5 & 1 & 0 & 0 & 0 \\ 0 & 0 & 0 & 3 & 0 & 0 \\ 0 & 0 & 0 & 0 & 3 & 0 \\ 0 & 0 & 0 & 0 & 0 & 3 \end{bmatrix} \tag{62}$$

Even if the von Mises equivalent stress contains some inherent limitations [87], it is one of the most widely used multi-axial fatigue criteria due to its

simplicity. Moreover, it is worth to notice that the objective of the presented work is to point out the impact of the MIMO target generation techniques on the fatigue life of mechanical components. Therefore, the requirement for the criterion is not to be accurate in absolute terms, but only to provide a consistent representation in the physics of fatigue damage accumulation in order to compare the effects of different excitation methodologies.

5.2.3 *Inverse power law*

Allegri and Zhang in [70] provide the theoretical foundations of the inverse power law, proposing an extended formulation of the law capable to address multi-axial stress state. In the hypothesis of narrowband dynamic responses, let consider an item exposed to the excitation of its usual operational environment (e) and the same item undergoing the excitation of an accelerated test (t). Being T_e and $\sigma_{vM,e}$ the expected life and the RMS level of equivalent von Mises stress responsible of the fatigue failure respectively, and T_t and $\sigma_{vM,t}$ the same quantities pertaining to the accelerated test, the Basquin's law of Equation (49) can be rewritten as

$$\frac{N0_t}{N0_e} = \left(\frac{\sigma_{vM,e}}{\sigma_{vM,t}}\right)^k \tag{63}$$

where $N0_i = n^+_{0,i} T_i$ is the total number of cycles counted in the time-to-failure (T_i), thus

$$\frac{T_t}{T_e} = \frac{n^+_{0,e}}{n^+_{0,t}} \left(\frac{\sigma_{vM,e}}{\sigma_{vM,t}}\right)^k \tag{64}$$

corresponding to the exact formulation for the law that links different levels of stress to their related expected life. Expanding Equation (64) in terms of spectral moments yields

$$\frac{T_t}{T_e} = \sqrt{\frac{\lambda_{2,e}}{\lambda_{2,t}}} \left(\frac{\lambda_{0,e}}{\lambda_{0,t}}\right)^{\frac{k-1}{2}} \tag{65}$$

Noting that the spectral moments are referred to the PSD of the equivalent von Mises stress of Equation (61), the previous expression returns the general scaling law suggested in [70]

$$\frac{T_t}{T_e} = \sqrt{\frac{\mathrm{Tr}[\mathbf{Q}\int_0^{+\infty}(2\pi f)^2\mathbf{S}_{\sigma\sigma,e}(f)\,df]}{\mathrm{Tr}[\mathbf{Q}\int_0^{+\infty}(2\pi f)^2\mathbf{S}_{\sigma\sigma,t}(f)\,df]}}\left(\frac{\mathrm{Tr}[\mathbf{Q}\int_0^{+\infty}\mathbf{S}_{\sigma\sigma,e}}{\mathrm{Tr}[\mathbf{Q}\int_0^{+\infty}\mathbf{S}_{\sigma\sigma,t}}\right)^{\frac{k-1}{2}} \tag{66}$$

Allegri and Zhang also demonstrated that Equation (66) returns the inverse power law of Equation (48) under special assumptions: i) the structure layout and the constraints of the testing setup perfectly replicate the operational conditions, ii) the reference SDM (MIMO control target) of the accelerated test is simply scaled with respect to the acceleration SDM measured in the real vibration environment

$$\mathbf{S}_{yy,t}^{ref} = K\mathbf{S}_{yy,e} \qquad K > 1 \tag{67}$$

Under these hypothesis and considering the frequency domain transfer function relationship of Equation (59), also the stress SDM of the accelerated test is simply scaled with respect to the operational one

$$\mathbf{S}_{\sigma\sigma,t} = K\mathbf{S}_{\sigma\sigma,e} \tag{68}$$

Therefore, substituting Equation (68) into Equation (66) yields

$$\frac{T_t}{T_e} = \left(\frac{1}{K}\right)^{\frac{k}{2}} \tag{69}$$

Finally, if the control target is just a single-axis test specification, Equation (67) can be simplified with the RMS values of the reference PSD and its corresponding operative one ($a_t^2 = Ka_e^2$). As a result, Equation (69) leads to the following expression of the inverse power law

$$\frac{T_t}{T_e} = \left(\frac{a_e}{a_t}\right)^k \tag{70}$$

Equation (70) demonstrates that, under specific assumptions, the widely used inverse power law (Equation (48)) is just a particular simplification of Equation (66) that provides the exact solution to the scaling problem.

5.3 NOVEL SOLUTION: EXTREME DYNAMIC RESPONSE METHOD (EDRM)

This section is devoted to provide the mathematical implementation of the novel MIMO target generation technique proposed in this research activity, namely *Extreme Dynamic Response Method (EDRM)*. The basic concepts of the algorithm are exactly the same of the *MDM* shown in Section 4.3 of the previous chapter. Despite the methodology of combining the phases and the coherences of the MIMO control target is identical, the final goal of the two methods are totally different. The objective of the *EDRM* is to fully exploit the total energy coming from the test specifications for exciting the test specimen with the most extreme vibration environment possible. Therefore, the *EDRM* correlates the multiple test specifications in order to get out the maximum responses from the specimen dynamic. This technique could be useful in multi-axis accelerated fatigue test where the goal of the control test is to damage the specimen minimising the time-to-failure.

The dynamic to be maximized could be the accelerations or the strain/stress responses of the specimen at some crucial points, e.g the measured accelerations of a cantilever point or the measured strain/stress at the crack location. It is worth to notice that the *EDRM* will be show in the following for the acceleration responses application, however it cloud be easily adapted for the stress/strain application by changing the initial transfer function relationship.

The MIMO transfer function relationship that links the reference SDM to the acceleration SDM of a generic point of the specimen under test is

$$\mathbf{S}_{xx} = \hat{\mathbf{H}}_{aa}\, \mathbf{S}_{yy}^{ref}\, \hat{\mathbf{H}}_{aa}^{H} \tag{71}$$

Therefore, the idea of the *EDRM* is to find the proper values of coherences and phases to be set in the reference SDM ($\mathbf{S}_{yy}^{ref}$) in order to maximise/minimise the trace of the acceleration SDM ($\mathbf{S}_{xx}$). Maximise/minimise the trace of the acceleration SDM means to equally maximise/minimise the acceleration PSDs of all the response channels.

In the general case of m channels of acceleration responses and ℓ control channels of reference accelerations, the closed form expression of the responses trace is

$$P = Tr(\mathbf{S_{xx}}) = \sum_{i=1}^{m} \left(\sum_{j=1}^{\ell} \sum_{k=1}^{\ell} \hat{H}_{aa,ij} S_{yy,jk}^{ref} \hat{H}'_{aa,ik} \right) \tag{72}$$

By introducing the Hermitian matrix $\mathbf{T} = \hat{\mathbf{H}}_{\mathbf{aa}}^{\mathbf{H}} \hat{\mathbf{H}}_{\mathbf{aa}}$, Equation (72) can be written in terms of reference coherences and phases between the pairs of control channels

$$P = \sum_{j=1}^{\ell} S_{yy,jj}^{ref} T_{jj} + 2 \sum_{j=1}^{\ell-1} \sum_{k=j+1}^{\ell} \sqrt{\gamma_{jk}^2 S_{yy,jj}^{ref} S_{yy,kk}^{ref}} \left| T_{jk} \right| \cos(\phi_{jk} - \xi_{jk}) \tag{73}$$

where

$$S_{jk}^{ref} = \left| S_{jk} \right| e^{i\phi_{jk}} = \sqrt{\gamma_{jk}^2 S_{yy,jj}^{ref} S_{yy,kk}^{ref}} \, e^{i\phi_{jk}} \tag{74}$$

$$T_{jk} = \left| T_{jk} \right| e^{i\xi_{jk}} \tag{75}$$

The definition of the trace of Equation (75) is very practical and useful because the only unknowns of the formula are ϕ_{jk} and γ_{jk}^2, that are the reference phases and the reference coherences of the control target, respectively. The other terms of the formula are known quantities: the PSD terms ($S_{yy,jj}^{ref}$ $\forall jj = 1 : \ell$) are the test specifications and the matrix $\mathbf{T}$ can be computed during the system identification pre-test phase when the control algorithm have to estimate the FRFs matrix between the drive inputs and the control outputs for performing the actual control test.

Therefore, the responses trace of Equation (75) has a maximum (minimum) when the reference coherences are all unitary and the cosine all equal to 1 (-1). This observation leads to the following conditions, addressed as *Extreme Dynamic Conditions*

$$P \text{ is minimum} \iff \begin{cases} \gamma_{jk}^2 = 1 \\ \phi_{jk} = \xi_{jk} + \pi \end{cases} \qquad \forall j, k = 1 : \ell, j \neq k \tag{76a}$$

$$P \text{ is maximum} \iff \begin{cases} \gamma_{jk}^2 = 1 \\ \phi_{jk} = \xi_{jk} \end{cases} \qquad \forall j, k = 1 : \ell, j \neq k \tag{76b}$$

As widely explained for the *MDM* in the previous chapter, the *Extreme Dynamic Conditions* of Equation (76) do not guarantee that the resulting reference SDM is positive (semi)definite. To overcome this limitation, the *EDRM* can be completed following the *phase pivoting principle* (Section 4.3.3). The principle

ensures the compliance with all the exiting phase dependencies and it always provides physically realizable control target.

It is worth to notice that the maximum condition (76b) is the one which deserves to be investigated due to its possible application in the field of multi-axis durability testing. The minimum condition (76a) instead, is here quoted to demonstrate in the following sections that all the other possible combinations of coherences and phases return responses traces that fall in the range between the minimum and the maximum value.

5.4 TEST CAMPAIGN

In order to asses the capabilities of the proposed MIMO target generation technique, an experimental campaign has been carried out by exploiting the three-axial electrodynamic shaker Dongling 3ES-10-HF-500 at the University of Ferrara. The technical characteristics and the performances of this advanced excitation system are described in detail in Chapter 3. SIEMENS' products for vibration testing analysis are used as data acquisition hardware and vibration control software, i.e. SCADAS Mobile SCM202V (V8 input and DAC4 output modules) and MIMO Random of Simcenter Testlab, respectively.

In particular, this experimental activity is divided in two main tasks: a short-testing campaign and a fatigue-testing campaign, described in the following Sections 5.4.2 and 5.4.3, respectively. In the short-testing campaign, the same specimen is subjected to multiple random vibration control tests of a duration of two minutes each. For each short-test, the MIMO control target is defined in accordance with different techniques, i.e. the same reference PSDs with different combinations of phases and coherences for the CSDs. The main objective of the short-testing campaign is indeed to investigate the impact of different MIMO control target procedures on the dynamic response of the specimen under test. In this sense, the short-testing analysis ensures a more representative and critical comparison of the available methods always examining the transfer function of the same structure. Of course, the PSD levels of the multiple test specifications are kept low enough to guarantee the resulting stress state, at the most stressed zone of the specimen, is below the material endurance limit. As a consequence, the dynamic response of the specimen can be compared throughout the entire test campaign because no

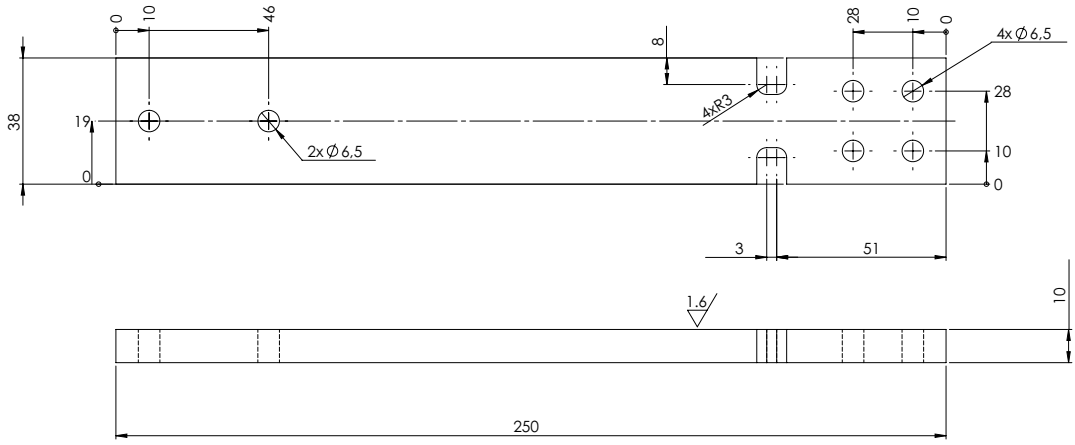

Figure 45: Detailed geometry of the test specimen (dimensions in mm).

Table 8: Basic mechanical properties of EN AW 6082 aluminium alloy [88]

Yield Strength	Fracture Strength	Young's Modulus	Poisson's Ratio	Elongation A12.5
365 MPa	385 MPa	77 GPa	0.32	27.2%

fatigue damage accumulation is detected and the structure transfer function remains unaltered.

In the fatigue-testing campaign instead, 48 specimens are tested until rupture by combining the test specifications with different target generation techniques. In this case, the objective of the test campaign is to experimentally establish the S-N curves in order to compare the effect of the target generation techniques in terms of fatigue damage and time-to-failure.

5.4.1 *Experimental setup*

The common approach followed in the specialized literature is to execute accelerated fatigue tests on specimens with simple shape, because of the greater control of the stress state. A widely adopted geometry consists of a cantilever beam shape, carrying a lumped mass on the free-end with the

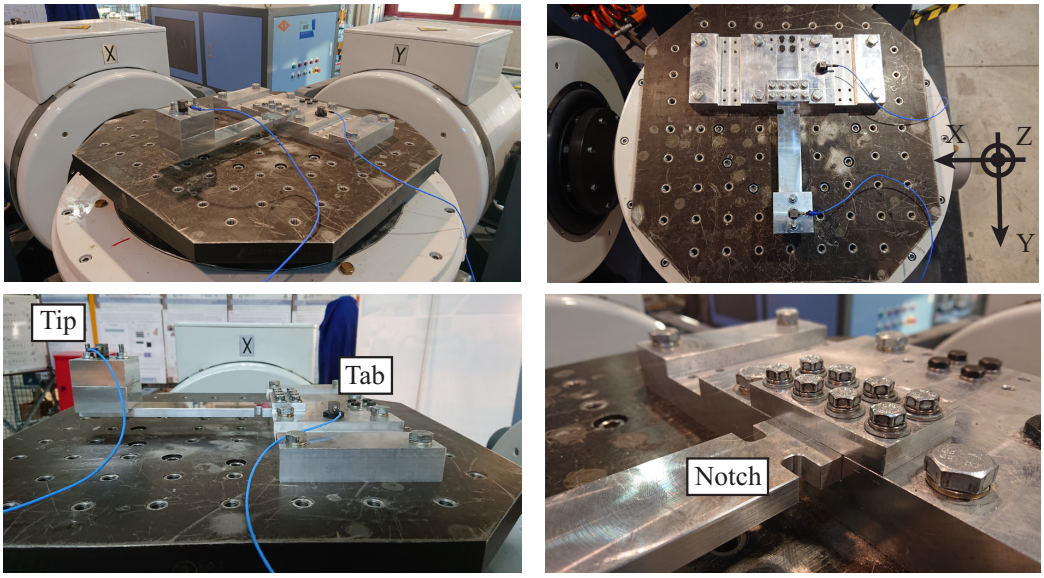

Figure 46: Experimental setup: top views of the specimen (left/right top); side view of the specimen (left-bottom); detail of the notch (right-bottom).

purpose to tune the most excited resonant frequencies [43, 89, 90]. Therefore for this experimental campaign, a cantilever beam with rectangular section has been chosen as a suitable geometry. In particular, the specimen is made of aluminium alloy, milled from a bar and mounted on the head expander by means of an ad-hoc designed fixture. The material used is the EN AW 6082, selected for its wide commercial availability. Its mechanical properties were inferred from literature [88] and reported in Table.8. U-shaped notches, placed near the location of maximum bending moment, identify the zones of prevalent damage accumulation, furthermore, a lumped mass of 0.47 kg screwed on the

Table 9: Comparison of the SN curve parameters

Base material sinusoidal loading		Notched specimen sinusoidal loading		Notched specimen random loading	
k	C	k_{spec}^{sin}	C_{spec}^{sin}	k_{spec}^{rnd}	C_{spec}^{rnd}
8	$6.3 * 10^{23}$	5.4	$1.46 * 10^{17}$	5.4	$5.34 * 10^{15}$

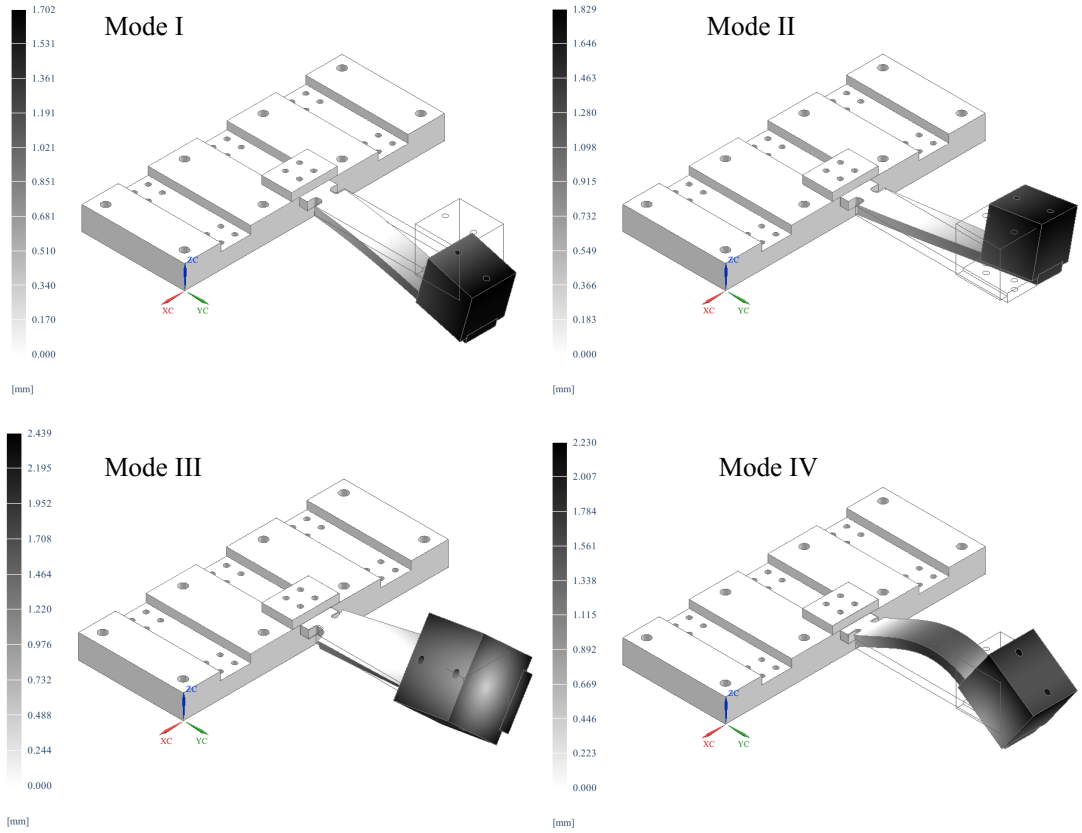

Figure 47: Mode shapes of the numerical modal analysis.

free-end has been used to accurately tune the resonant frequencies under the maximum working frequency of the shaker. Figure 45 reports the details of the specimen geometry and Figure 46 shows the specimen mounted on the head expander of the shaker. Labels *Tab* and *Tip* shown in Figure 46 denote the locations of the two tri-axial accelerometers utilized during the entire test campaign: *Tab* is the control accelerometer and it is fixed on the fixture close to the specimen mounting point; *Tip* is the measuring accelerometer and it is attached at the specimen's free-end on top of the counterweight.

At the preliminary stage of the project, a Finite Element Model (FEM) allowed the refinement of the system dynamics and the ability to set the test specifications levels for the fatigue tests as a function of the test durations. In this regard, it is fundamental to optimally estimate the parameters of the

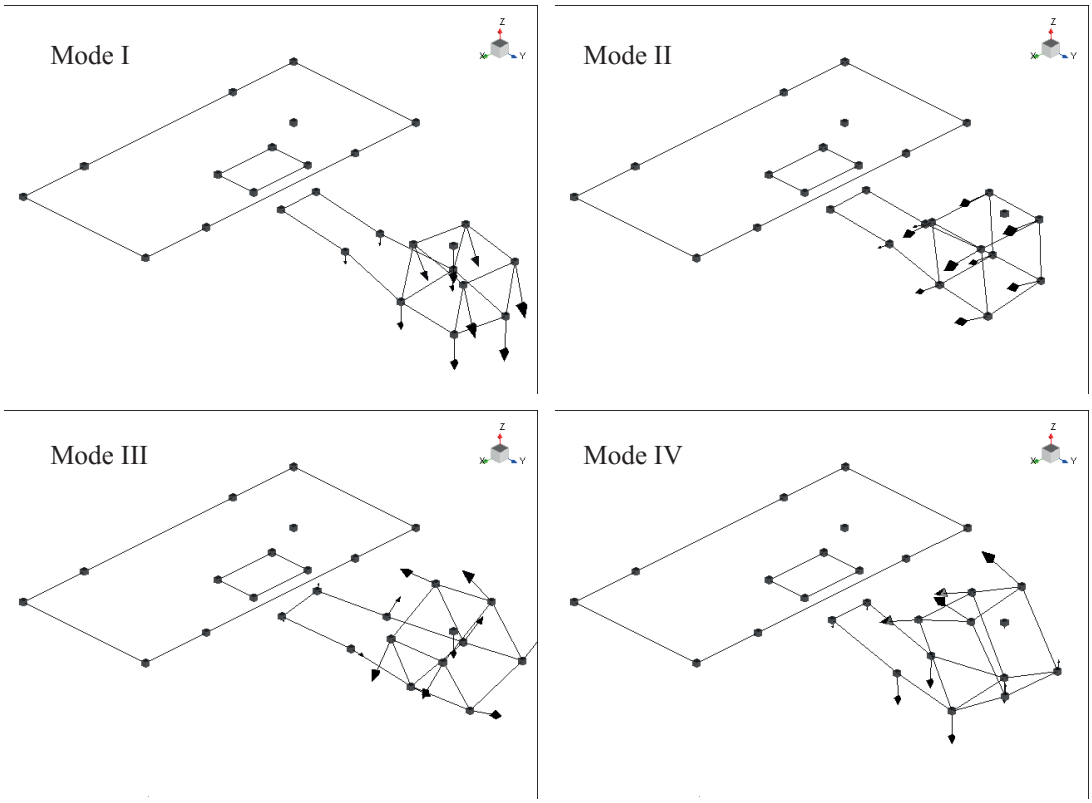

Figure 48: Mode shapes of the experimental modal analysis.

S-N curve which better approximate the actual test case. The geometrical parameters (scale, shape, notches, etc.) and the condition of the surface are critical factors which effect the fatigue behaviour of the specimen under test. Specifically, these factors reduce the fatigue limit thus changing the slope of the S-N curve. From the literature there are several empirical relationships to modify the S-N curve through the use of the penalty coefficients [91]. Moreover, it has been demonstrated [92, 93] that the S-N curve exponent (k) changes sharply passing from sinusoidal loading (standard fatigue testing) to random loading. In particular, the S-N curve under random stress histories appears to be shifted and rotated clockwise with respect to the sinusoidal load conditions, thus resulting in a faster accumulation of fatigue damage [94]. This is due to the fact that random load histories are deeply affected by load interaction and sequence effect [70]. Unfortunately, there are no mathematical relationships

Table 10: Comparison between modal parameters obtained with FEM and EMA.

	f_{FEM}	f_{EMA}	ζ	MAC	Freq. Error
Mode I	62.0 Hz	55.5 Hz	0.28%	0.98	11.7%
Mode II	131.7 Hz	118.0 Hz	0.22%	0.99	11.6%
Mode III	401.9 Hz	350.0 Hz	0.18%	0.90	14.8%
Mode IV	503.6 Hz	436.7 Hz	1.32%	0.97	15.3%

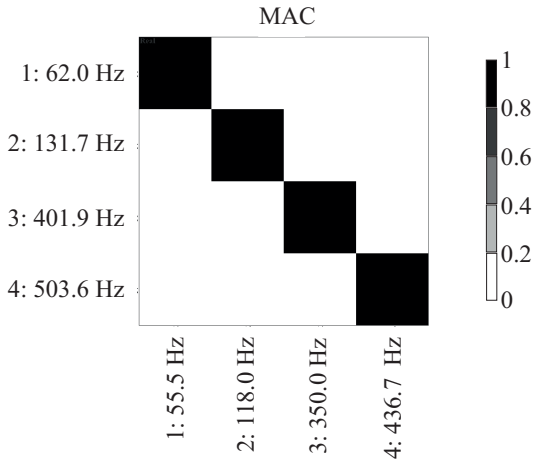

Figure 49: Correlation Modal Assurance Criteria (MAC) results: numerical (rows) and experimental (columns).

which calculate the S-N curve parameters under random loading, starting from the ones experimentally obtained during standard fatigue tests, i.e. under constant amplitude conditions. For this purpose, Root in [95] provides an analytical expression (also mentioned by Lalanne in [68])

$$C^{rnd} = \frac{C}{2^{\frac{k}{2}}\Gamma\left(1+\frac{k}{2}\right)} \tag{77}$$

where the S-N curve evaluated for random loading has smaller ordinate at the origin with respect to that obtained under sinusoidal stress, but the same slope. It is known that this assumption is not correct, however it is an acceptable approximation at the preliminary phases of the specimen design. Table 9 shows the comparison of the S-N curve parameters of the base material [88], of the

notched specimen under sinusoidal loading [91] and the approximation to random stress histories [68].

The FE model comprises also the ensemble of specimen and the countermass mounted on the fixture. Therefore the results of the FEM have been used to design the fixture with the purpose to avoid interference with the dynamics of the specimen. Based on the simulated results of the numerical modal analysis shown in Figure 47, the first four mode shapes of the specimen are below the 500 Hz, which is a frequency value less than three times the first bending mode of the fixture.

The mode shapes resulting from the FE model have been confirmed from the subsequent Experimental Modal Analysis (EMA), carried out with an ICP instrumented impact hammer by *PCB Piezotronics*. The EMA has been performed on the specimen constrained with the fixture to the head expander of the shaker, in order to simulate the boundary conditions of control test. The mode shapes of the first four natural frequencies of the specimen are shown in Figure 48. Mode I and Mode IV are the first two bending modes in the YZ plane. Mode II is the first bending mode in the XY plane. Mode III is a torsional mode. Table 10 summarizes and compares the modal parameters obtained with the EMA and the numerical analysis. It can be noted mismatching between the resonance frequencies detected by the two analysis. However, this gap may be attributed to the modeling of the specimen connections in the FE model. The continuity of the mesh nodes has been imposed on the interface between the specimen and the fixture. The approximation to a perfect joint connection makes the FE model stiffer with respect to the test configuration. The nearly constant frequency error over the four modes (11% ÷ 15%) confirms this assumption. Moreover, Figure 49 exhibits the results of the Modal Assurance Criteria (MAC) performed on the numerical and the experimental mode shape vectors. MAC values always greater than 90% point out the excellent correlation between the two modal models.

5.4.2 *Short-test analysis*

As mentioned at the beginning of this chapter, the main purpose of the short-testing campaign is to critically compare the effects of the MIMO target generation techniques on the dynamic response of the specimen under test. Thus the same specimen, hereinafter named *spec-0*, is subjected to multiple random

control tests of two minutes each. The MIMO target generation techniques compared throughout this experimental campaign are:

i) *Extreme Dynamic Response Method (EDRM)*. It is the novel technique specifically designed in this thesis for this application. The *EDRM-max* and *EDRM-min* should provide the extreme limits of the range in which all the other possible solutions fall.

ii) *0ph-Hcoh Method*. This technique set in-phase ($\phi_{jk}^2 = 0^o$) and fully coherent ($\gamma_{jk}^2 = 0.98$) control outputs. As explained in Chapter 3, this procedure generates a sort of single-axis test inclined along the bisector of the control axes, i.e. the directions of the reference PSDs.

iii) *Independent References Method (IRM)*. It is the standard procedure [32] when no information about the CSD terms is known. This procedure defines the reference SDM as a diagonal matrix by simply setting low coherence ($\gamma_{jk}^2 = 0.05$) for all the cross-terms. This technique will be addressed in the following of this chapter as *0ph-Lcoh Method*.

iv) *Minimum Drives Method (MDM)*. It is the novel solution proposed in Chapter 4 of this thesis which guarantees the conduct of the MIMO control test by exploiting the minimum power from the shaker drives.

v) *Independent Drives Method (IDM)*. It is the solution proposed in [58] and mentioned in the US Military Standard [32] to overcome the problem of meeting the *minimum drive criteria*. This technique performs the control test by driving the excitation system with a set of uncorrelated inputs (independent drives).

It is worth to notice that the main objective of the last two MIMO target generation techniques, i.e. the *MDM* and *IDM*, is to minimize the total power required by the shakers to run the control test. However, they are both included in this experimental comparison because it could be interesting also to highlight the effects on the specimen dynamic of procedures that are just focused on preserving the excitation test equipments.

The configuration of the two tri-axial accelerometers used during this short-testing campaign is the one shown in Figure 46 and described in the previous section. Moreover, in order to extend the study also to the stress/strain analysis

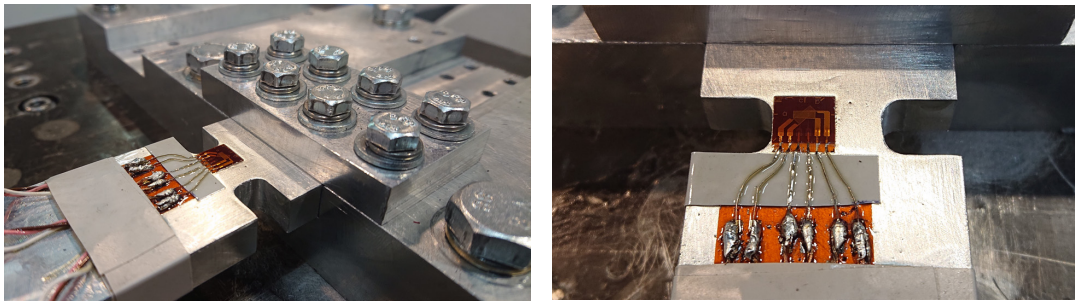

Figure 50: Strain gauge rosette applied on *spec*-0 in the short-test campaign.

and to obtain the dynamic stress response of the specimen, a strain gauge rosette is bonded at the notch as close as possible to the most stress zone of *spec*-0. Figure 50 illustrates the strain gauge installation. The adopted strain gauge is the 3/120-RY93 by *HBM*, that is a stacked rectangular rosette with axes crossed at 0°/45°/90°. The angular values refer to the directions of the measuring grids. The strain gauges have a resistance of 120Ω and a measuring grid length of 3mm. Thanks to the strain gauge rosette, it is possible to determine the biaxial stress state of the notch. The normal stress and the shear stress can be computed from the strain measurements of the rosette as [96]

$$\sigma_{xx} = \frac{E}{(1+\nu)(1-2\nu)}\left[(1-\nu)\varepsilon_{xx} + \nu\varepsilon_{yy}\right] \tag{78a}$$

$$\sigma_{yy} = \frac{E}{(1+\nu)(1-2\nu)}\left[(1-\nu)\varepsilon_{yy} + \nu\varepsilon_{xx}\right] \tag{78b}$$

$$\tau_{xy} = G\gamma_{xy} \tag{78c}$$

where

$$\gamma_{xy} = 2\varepsilon_{45} - \varepsilon_{xx} - \varepsilon_{yy} \tag{79}$$

Therefore the stress SDM ($\mathbf{S}_{\sigma\sigma}$) of Equation (60) con be reduced to a 3x3 matrix which fully describes the biaxial stress state of the notch in frequency domain.

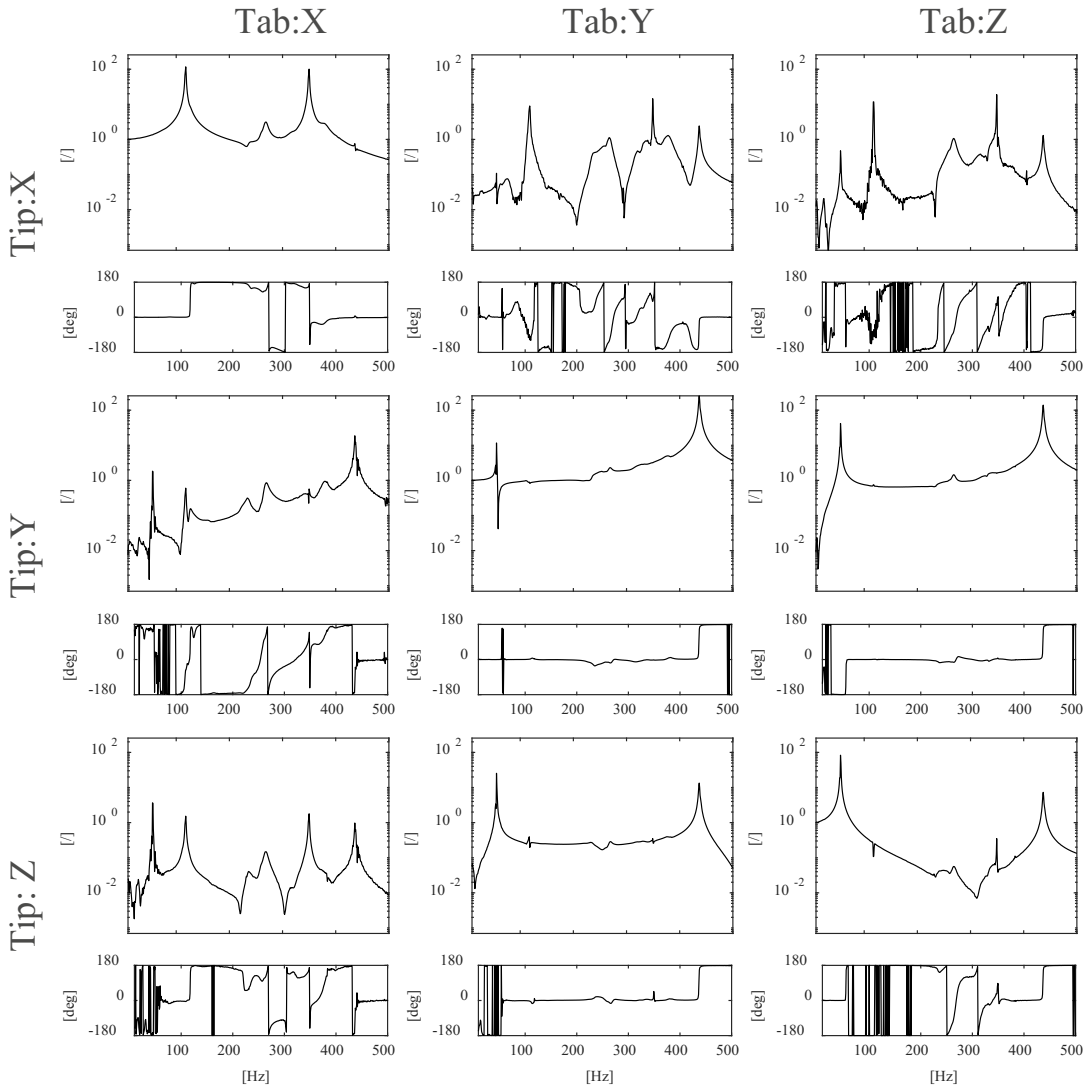

Figure 51: 3x3 Transfer Functions matrix ($\hat{\mathbf{H}}_{aa}$) between *Tab* accelerometer (inputs) and *Tip* accelerometer (outputs).

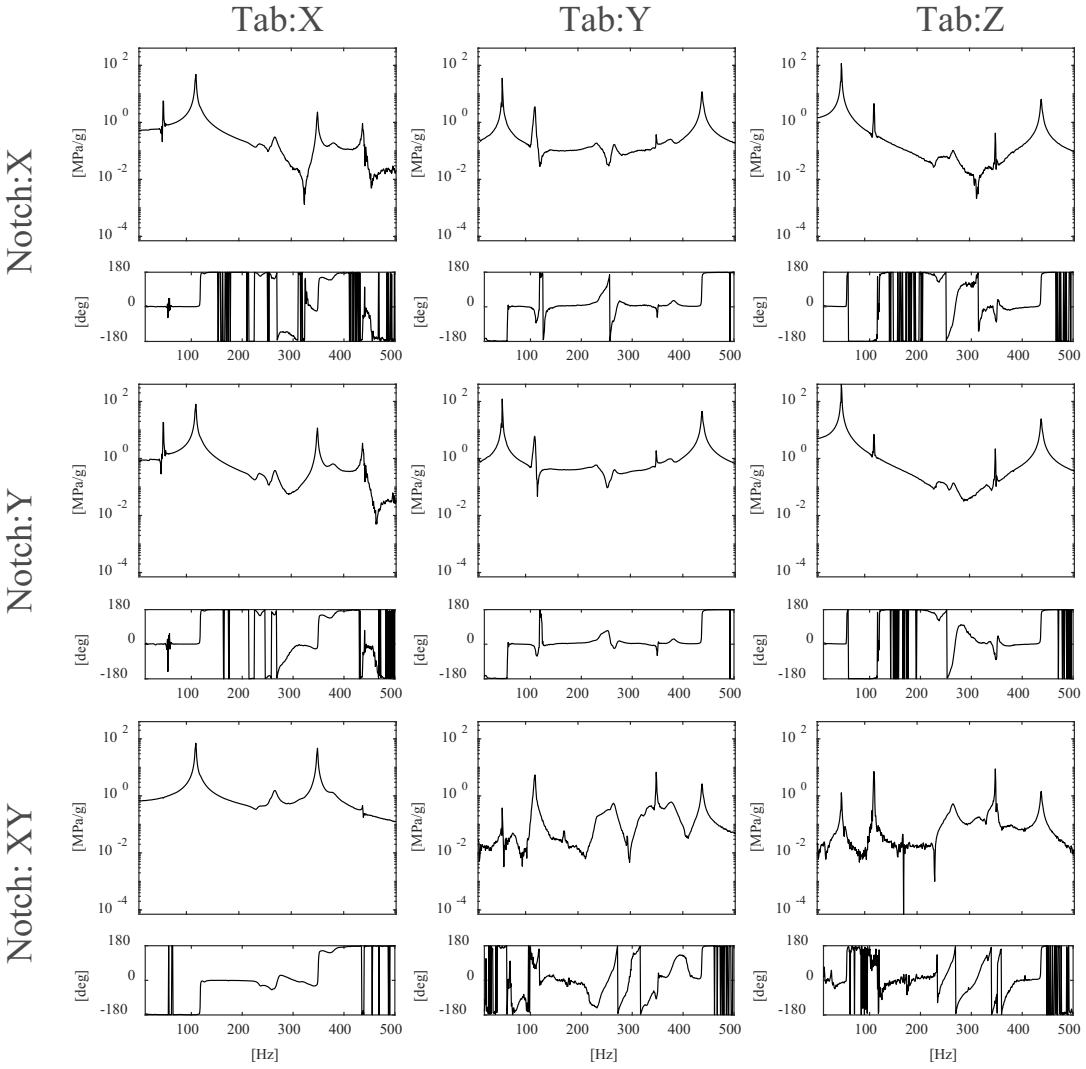

Figure 52: 3x3 Transfer Functions matrix ($\hat{\mathbf{H}}_{\sigma a}$) between *Tab* accelerometer (inputs) and *Notch* strain gauge rosette (outputs).

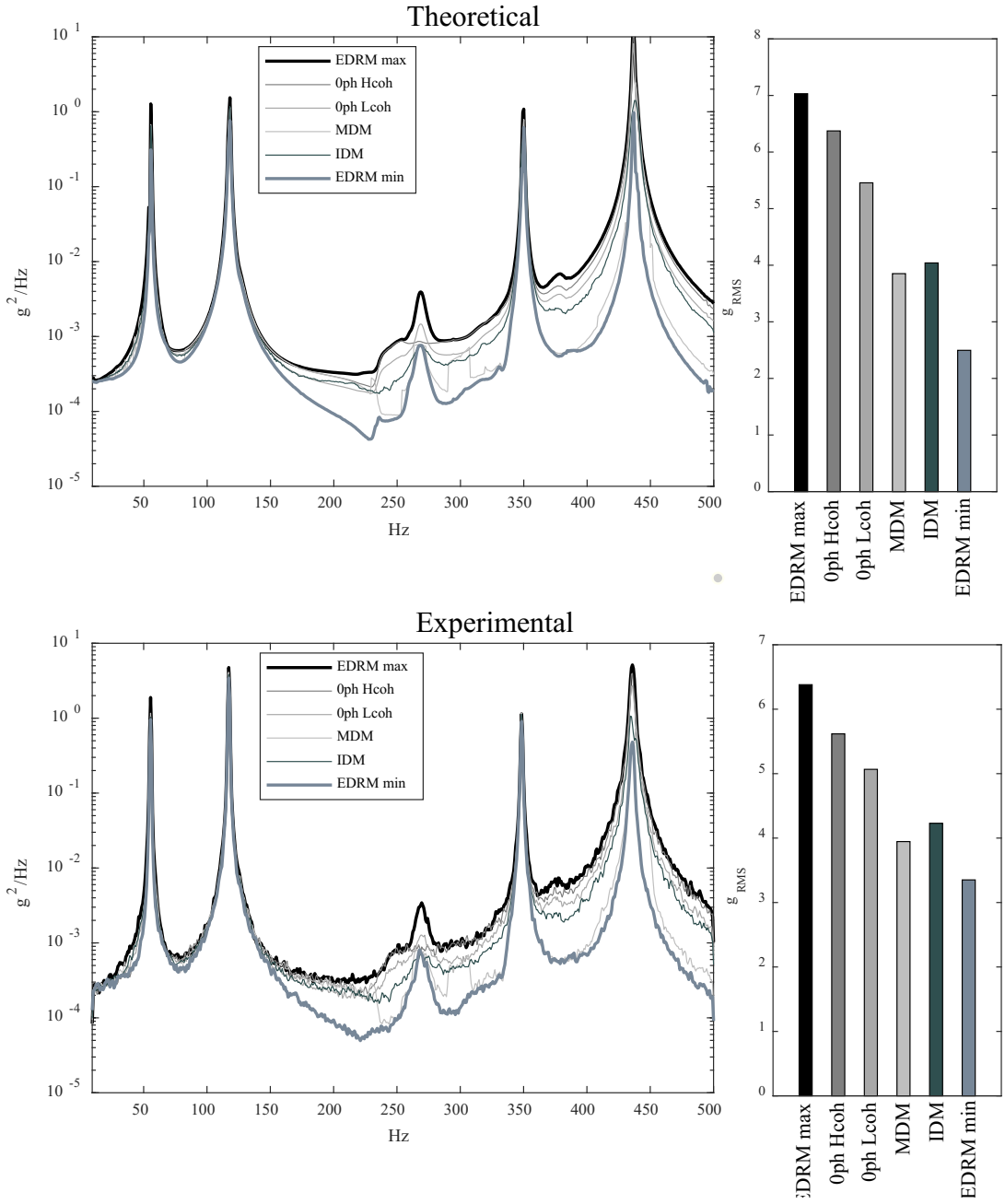

Figure 53: Short test campaign: tip traces comparison. Theoretical results (top), test results (bottom).

Figure 51 presents the Transfer Functions (TFs) matrix ($\mathbf{H}_{aa}$) that links the three-control channels of accelerometer *Tab* to the three-response channels of the accelerometer attached on top of the counterweight, *Tip*. Furthermore, Figure 52 shows the TFs matrix ($\mathbf{H}_{\sigma a}$) between the control accelerometer *Tab* and the three channels of the strain gauge rosette *Notch*. Both the MIMO TFs matrices are obtained during the pre-test phase by performing a low level random test with decorrelated inputs.

With regards to the definition of the test specifications, a flat profile of 0.2 gRMS in the frequency range [10 - 500] Hz has been chosen as reference PSD for all the three directions of the control accelerometer *Tab*. These levels for the reference PSDs induce in the notch a low-value von Mises stress ($\sigma_{vM} = 4.5\ MPa_{RMS}$). This value theoretically guarantees more than 10k hours of time-to-failure, in accordance with the data reported in Table 9. Working below the endurance limit is important in order to preserve the specimen structure and to be able of comparing its dynamic response throughout the entire short-testing campaign.

The results of the series of short-tests are depicted in Figure 53. In particular, the figure shows the trace of the *Tip* SDM, i.e. the dynamic response of the specimen in terms of accelerations measured on top of the counterweight ($P = Tr[\mathbf{S}_{Tip}]$). Being the trace of the *Tip* SDM the summation of the acceleration responses, its representation offers an overview of the global dynamic of the specimen. In fact, Figure 53 clearly highlights four peaks which are representative of the first four natural modes of the specimen. Furthermore, on the right of Figure 53, the RMS values of the responses trace are specified with the bar plots, in order to provide a further remarkable information on the overall capabilities of each target generation technique. Figure 53 compares the results in both the theoretical and the experimental form. The theoretical results derive from simulated tests, i.e. the *Tip* SDM is directly calculated from the input-output relation of Equation (71). The experimental data are instead the results of the actual control tests. It can be noted that the theoretical and the experimental data offer comparable results, sign that the control tests have been properly performed and the control algorithm has accurately replicated the test specifications. In terms of RMS values, the gap between the extreme values is less emphasized in the experimental results with respect to the theoretical ones. This is probably due to the randomness of the control process which cannot always replicated perfectly the user-defined reference SDM, thus flattening

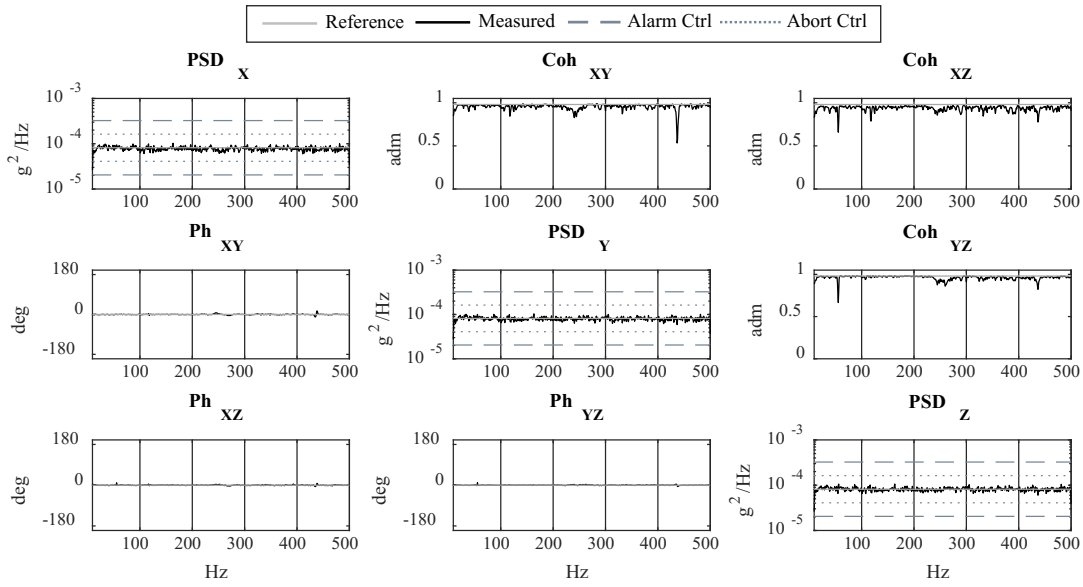

Figure 54: Short test campaign: *Tab* SDM. Control results of the *0ph-Hcoh Method*.

the final result. However, the different capabilities of each target generation procedure are well-highlighted also from the experimental results. First of all, the results of the proposed technique *EDRM max/min* clearly represent the extreme levels reachable by the dynamic response of the specimen when it is subjected to the multiple test specifications. All the other possible MIMO target generation techniques provide results that fall into the range between the minimum and the maximum specimen dynamic solution. In this context, it is worth to notice that in term of RMS value, the experimental solution of the *EDRM-max* is almost 2 time higher than the *EDRM-min* (2.8 times higher, theoretically). These results definitely point out that the combinations of the multiple test specifications heavily effect the dynamic response of the specimen. As a consequence, the capability of the specimen to withstand the actual vibration environment can extremely vary depending on the adopted MIMO target technique. Finally, it is possible to conclude that the two techniques which aim to minimize the total drives power (*MDM* and *IDM*) tend to less stress also the specimen dynamic, with results which get closer to the *EDRM-min*.

In addition, in the remaining part of this section, a deeper analysis will be performed focusing the study just on three MIMO target generation techniques.

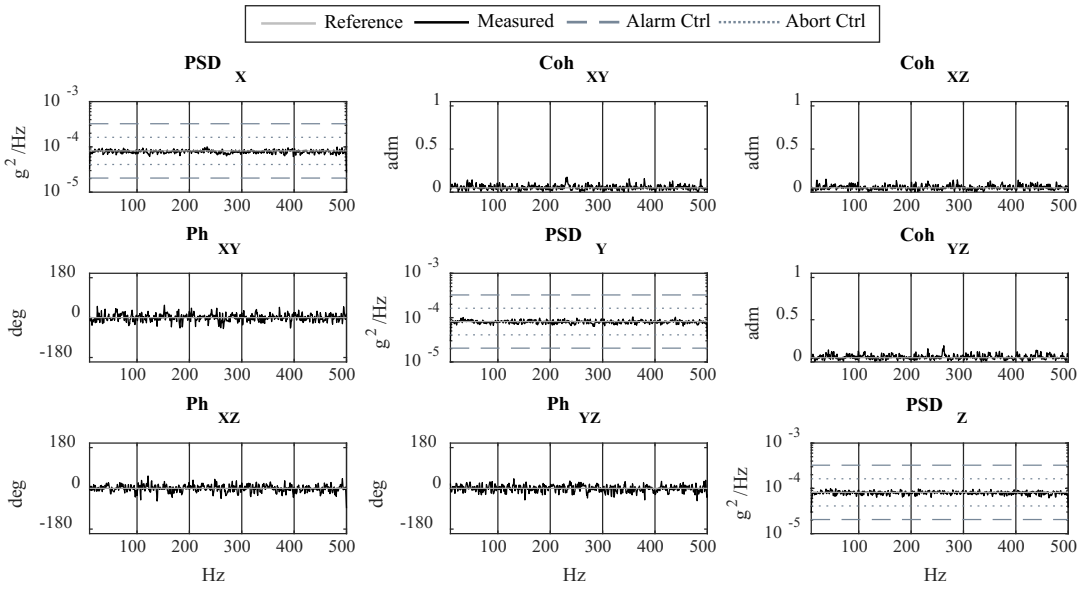

Figure 55: Short test campaign: *Tab* SDM. Control results of the *0ph-Lcoh Method*.

This choice was made to guarantee a clearer investigation of the phenomena, nevertheless the following outcomes can be extend to all the other MIMO target procedures.

Therefore, Figures 54, 55 and 56 show the control results of the *Tab* SDM by adopting the *0ph-Hcoh Method*, the *0ph-Lcoh Method* and the *EDRM-max*, respectively. These results are illustrated in a matrix subplot fashion. The subplots on the diagonal show the replication of the test specifications. In particular the black curves are the measured PSDs along the three control directions, the dotted-gray lines and the dashed-gray lines are the alarm and the abort control limits fixed at $\pm$3dB and $\pm$6dB from the references (gray lines). In the upper and lower triangular parts of the matrix the coherences and phases (in degrees) of the upper triangular CSDs are reported, respectively. Since the matrices are Hermitian, the subplots are also representative for the lower triangular CSDs (complex conjugates). The figures show normal end tests, meaning that the full level (0.2 gRMS) has been successfully run for 2 min and no spectral lines overcome the abort thresholds.

Moreover, Figure 57 exhibits the three-dimensional scatter plots of the recorded acceleration signals along the three control directions of accelerom-

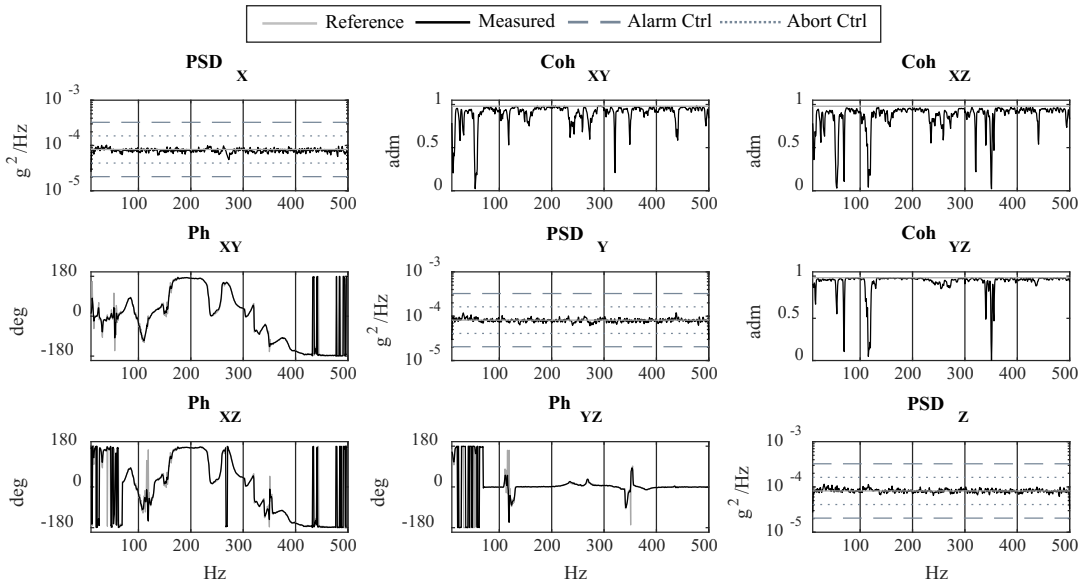

Figure 56: Short test campaign: *Tab* SDM. Control results of the *EDRM-max*.

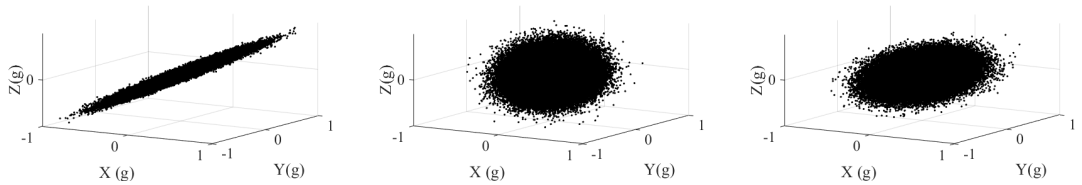

Figure 57: Short test campaign: 3D scatter plots of the acceleration signals measured on the *Tab*. 0ph-Hcoh (left), 0ph-Lcoh (middle), EDRM-max (right).

eter *Tab*. The three different data distribution undoubtedly described three different methodologies of combining the test specifications, resulting in three distinct ways of moving the shaker table for exciting the test specimen.

Despite the specimen is excited in three different manners by using the three MIMO target techniques, some interesting outcomes can be inferred from the comparison of the *Tip* SDMs of Figure 58, where the results of the *0ph-Hcoh Method*, the *0ph-Lcoh Method* and the *EDRM-max* are the gray, light-gray and black curves, respectively. It is worth to notice that, at the resonance frequencies, the three recorded responses of the *Tip* are equally phased and correlated, independently of the adopted MIMO target generation technique.

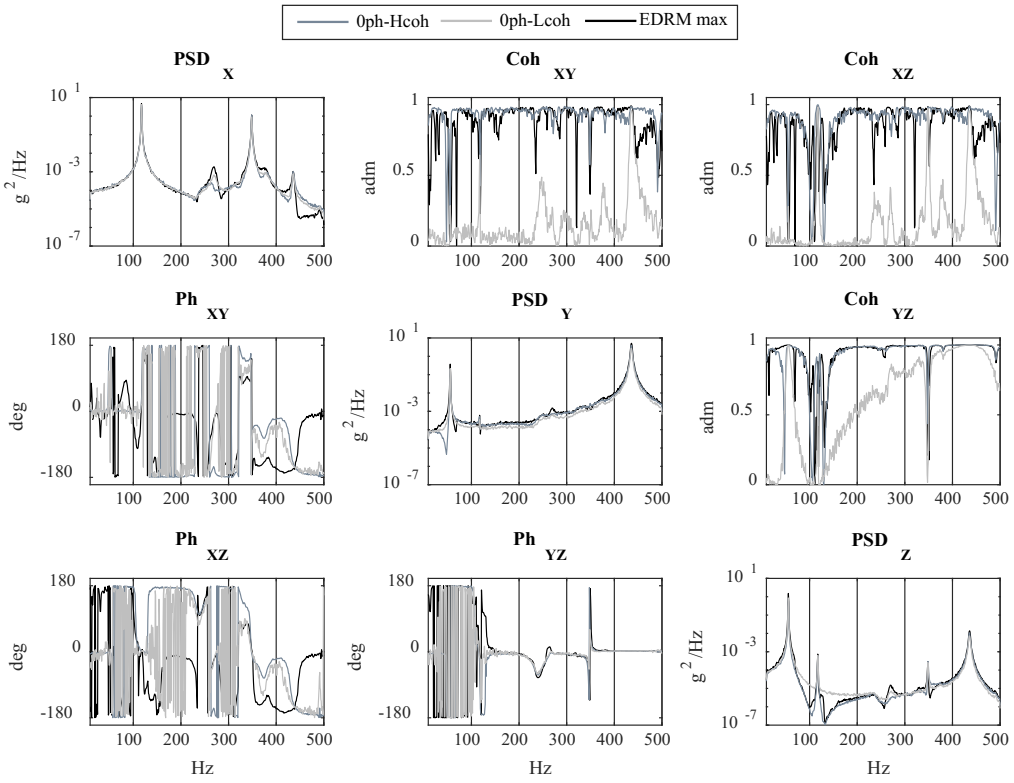

Figure 58: Short test campaign: *Tip* SDM.

This phenomenon is even more evident when looking at the curves behavior of the *0ph-Lcoh Method*: out of the resonances frequencies, decorrelated test specifications generate decorrelated acceleration responses of the *Tip*; at the resonance frequencies instead, the coherence values increase until they reach the same values provided by the other MIMO target procedures. The same applies to the phase values.

To better investigate this phenomenon, Figure 59 shows the *Tip* SDMs in the narrowband around *Mode IV* (436 Hz), where the PSD terms along the diagonal are represented in linear scale. Figure 59 certainly underlines the CSDs behavior at resonance frequency. Despite the methodology adopted for combining the test specifications and thus, despite the different excitation imposed on the specimen, the tip acceleration responses at the resonance frequency result to be phased and correlated always in the same manner. This

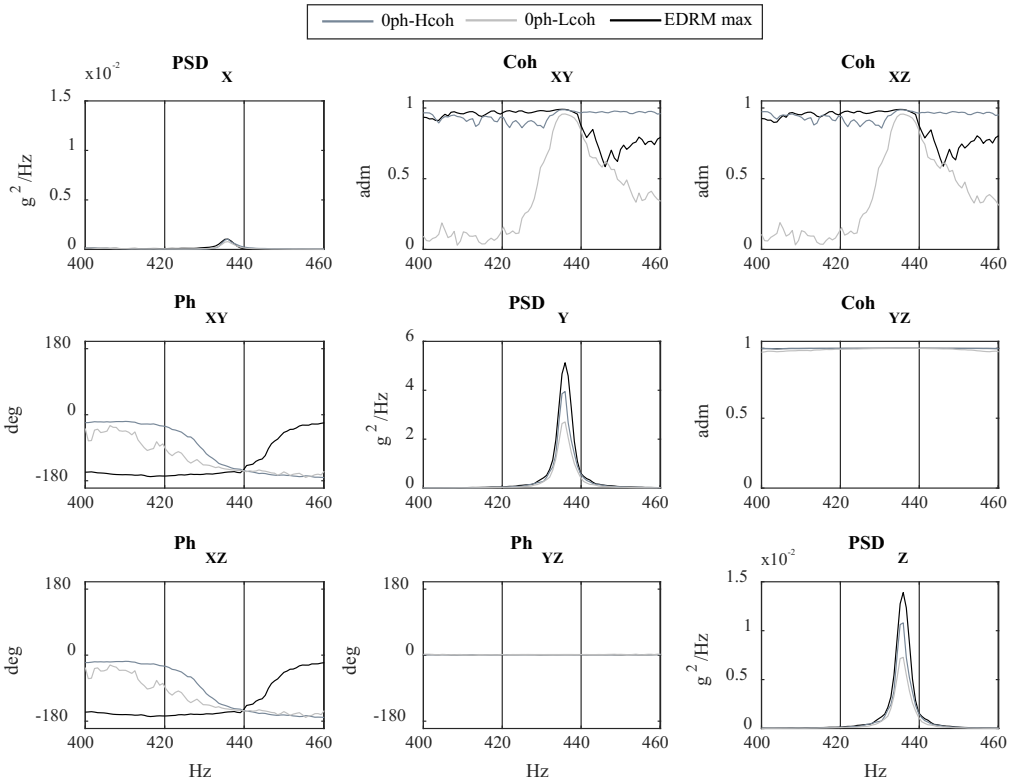

Figure 59: Short test campaign: *Tip* SDM. Zoom around Mode IV (436 Hz).

is due to the fact that, at the resonance frequency, the dynamic response of the specimen is fully driven by its natural mode shape and it is independent on the correlation of the multiple input excitations. The phenomenon can be proved by considering the CSD_{YZ} of the *Tip* SDM of Figure 59, which will be addressed in the following as $S_{TIP,23}$. It is worth to notice that the statement can be demonstrated for all the CSD terms, without loss of generality. Referring to the MIMO transfer function relationship of Equation (71), the analytical formulation of the output cross-term can be rewritten as

$$S_{TIP,23} = \sum_{j=1k=1}^{3} \left| S_{TAB,jk} T_{jk}^{23} \right| e^{i(\phi_{jk}+\xi_{jk})} \tag{80}$$

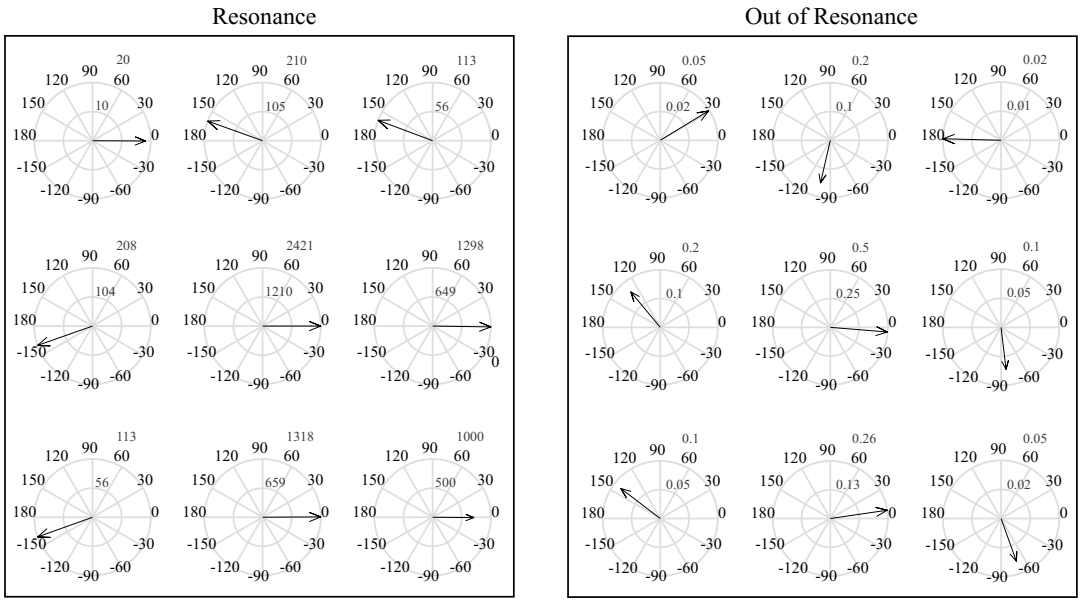

Figure 60: Short test campaign: matrix $\mathbf{T^{23}}$. At the resonance frequency of Mode IV, 436 Hz (left); at a generic frequency out of resonance, 130 Hz (right).

where $\mathbf{T^{23}}$ is a special 3x3 matrix obtained by the rearrangement of the 2nd and 3nd rows of the TFs matrix ($\mathbf{H_{aa}}$ shown in Figure 51)

$$\underset{(3\times 3)}{\mathbf{T^{23}}} = \underset{(3\times 1)}{\hat{\mathbf{H}}_{\mathbf{aa}}(2,:)^{\mathsf{T}}}\ \underset{(1\times 3)}{\hat{\mathbf{H}}^{\mathbf{H}}_{\mathbf{aa}}(:,3)^{\mathsf{T}}} \tag{81}$$

It can be noted that this special matrix, at the resonance frequency, becomes an Hermitian matrix ($T^{23}_{ij} = T^{23'}_{ji}$), since the resonance condition makes linearly dependent the rows of the TFs matrix from which it derives [60, 62]. Figure 60 compares the featuring of matrix $\mathbf{T^{23}}$ at the resonance frequency of *Mode IV* (436 Hz), with respect to a generic frequency distant from the resonance condition (130 Hz). In Figure 60, matrix $\mathbf{T^{23}}$ is illustrated by means of 3x3 subplots which show each element of the matrix as a vector distributed in the space according to its amplitude and phase. It can be seen that, at the resonance frequency matrix $\mathbf{T^{23}}$ is Hermitian, i.e. the lower triangular part is the complex conjugate of the upper triangular part. Therefore, since the control

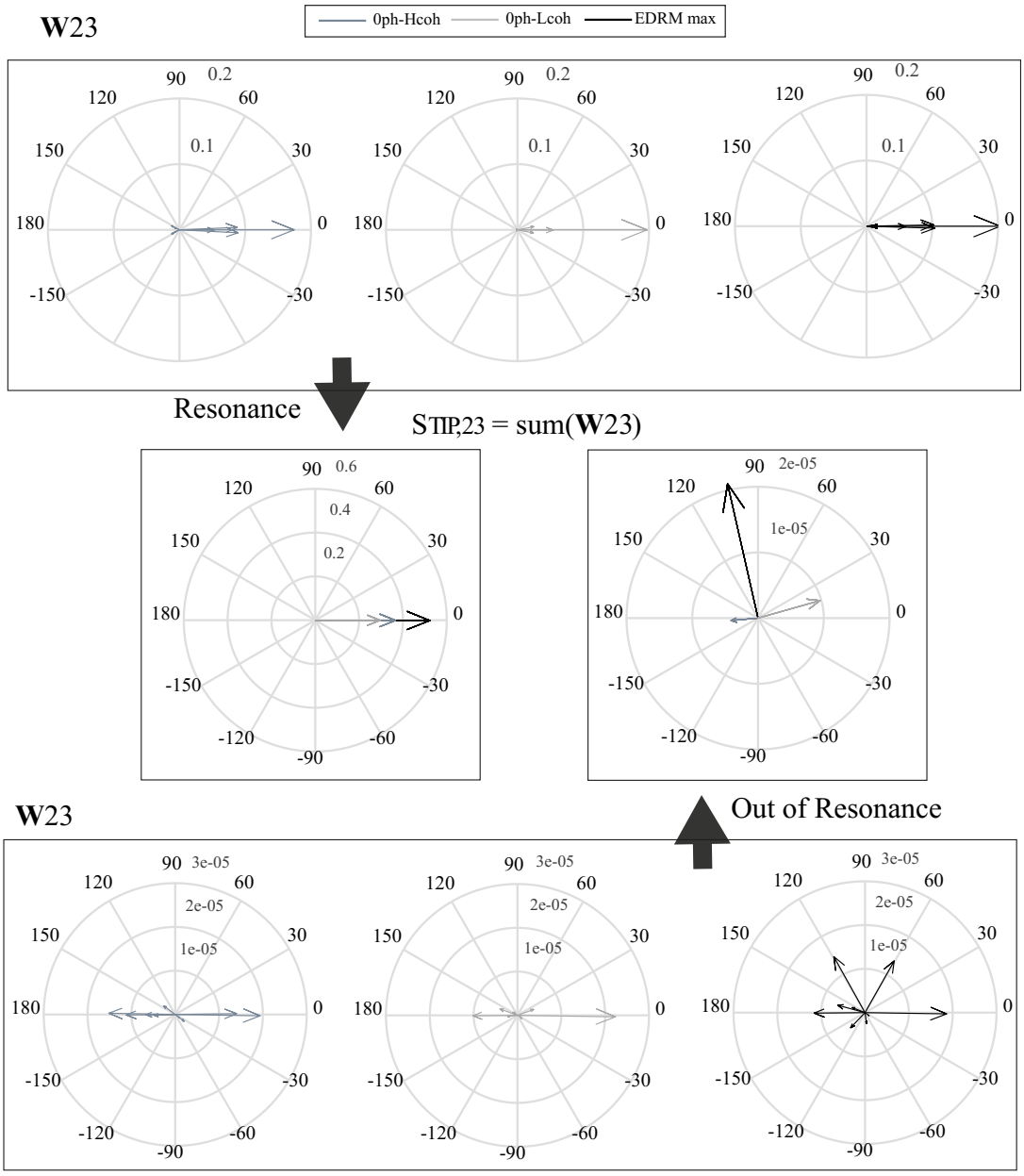

Figure 61: Short test campaign: graphical explanation of the effects of the resonance condition on the CSD control terms. Matrix $\mathbf{W^{23}}$ and corresponding CSD term $S_{TIP,23}$ at resonance frequency of Mode IV, 436 Hz (top box and middle-left box, respectively). Matrix $\mathbf{W^{23}}$ and corresponding CSD term $S_{TIP,23}$ out of resonance frequency, 130 Hz (bottom box and middle-right box, respectively).

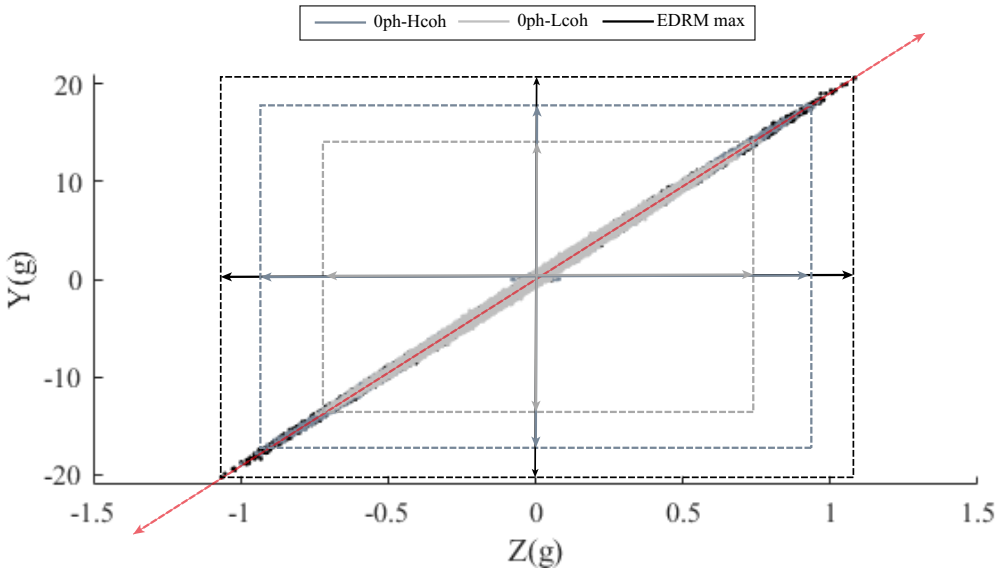

Figure 62: Short test campaign: scatter plots of the acceleration signals measured on the *Tip* along Y and Z directions ($X \simeq 0$). The signals are filtered in the narrowband of Mode IV (436 Hz).

SDM ($\mathbf{S}_{TAB}$) is Hermitian too, just for the resonance condition Equation (80) can be rewritten as

$$S_{TIP,23} = \sum_{j=1}^{3} \left| S_{TAB,jj} T_{jj}^{23} \right| e^{i(\xi_{jj})} + 2 \sum_{j=1}^{2} \sum_{k=j+1}^{3} \left| S_{TAB,jk} T_{jk}^{23} \right| \cos(\phi_{jk} - \xi_{jk}) \quad (82)$$

Equation (82) point out that, at the resonance frequency, the CSDs of the control SDM ($S_{TAB,jk}$) do not effect the imaginary part of $S_{TIP,23}$, providing a contribution just for the real part. Thus, the phase result of the response CSD ($S_{TIP,23}$) only depends on the phases of the diagonal terms of matrix $\mathbf{T^{23}}$ (ξ_{jj}). Figure 61 graphically visualizes the phenomenon. In the top and in the bottom of the figure, the result of matrix $\mathbf{W^{23}}$ (where $W_{jk}^{23} = S_{TAB,jk} T_{jk}^{23}$) are shown at the resonance frequency and out of the resonance condition, respectively. The comparison is between the *0ph-Hcoh Method*, the *0ph-Lcoh Method* and the *EDRM-max* which are depicted in gray, light-gray and black vectors, respectively. Moreover, in the middle of the figure the various CSD terms ($S_{TIP,23} = \sum_{j,k=1}^{3} W_{jk}^{23}$) resulting from the respective techniques, are shown in the same plot in order to better highlight the result of the analysis.

It is noticeable that, far away from the resonance condition, the phase and the coherence of the CSD term strictly depend on the technique adopted for combining the test specifications. At the resonance frequency instead, Figure 61 confirms the outcomes of Equation (82). In this case, it is possible to conclude that the coherence and phase relationships between the responses of the specimen, do not depend on the adopted MIMO target generation technique, but they only depend on the phase relationships of the TFs matrix, which are ruled by the resonance condition and thus by the inherent dynamic properties of the specimen.

The adopted MIMO target generation technique, even if it does not effect the correlation and the phase shift between the responses, it can however effect the amplitude of responses, as highlighted in Figure 59. The amplitude of the response PSDs of the *EDRM-max* (black curves) are 1.91 times higher than the *0ph-Lcoh Method* (light-gray curves), and 1.29 times higher that the *0ph-Hcoh Method* (gray curves). Thanks to the procedure explained in Section 5.3 in fact, the *EDRM* is capable of combining in a more efficient way the total energy offered by the test specifications in order to better excite the natural modes of test specimen. Figure 62 supports this statement by showing the scatter plot of the recorded acceleration signals along directions Y and Z of accelerometer *Tip*. In particular the signals are filtered in the narrowband of *Mode IV* in order to point out the data dispersion corresponding to this particular mode shape. It is worth to notice that, in the narrowband of *Mode IV* the contribution of the acceleration signal along the X-axis is negligible, as also highlighted in Figure 59, and thus it has not been considered into the scatter plots analysis. Figure 62 clearly highlights the different capabilities of the various MIMO target generation techniques on proper exciting the dynamic response of the specimen. Furthermore, the data distributions resulting from the three compared techniques are equally oriented along the same direction, i.e. they have the same resultant of accelerations (red-dotted arrow). This result finally confirms that different MIMO target generation techniques do not change or alter the dynamic response of specimen under test, but they can eventually scale up/down its intensity by better exciting all the existing mode shapes.

It is worth to notice that, the above analysis focused on *Mode IV* can be extend also to the other mode shapes. In particular, Figure 63 and Figure 64 refer to the narrowband around *Mode I* (56 Hz) and they are the *Tip* SDMs and the scatter plots of the acceleration signals along the Y and Z directions

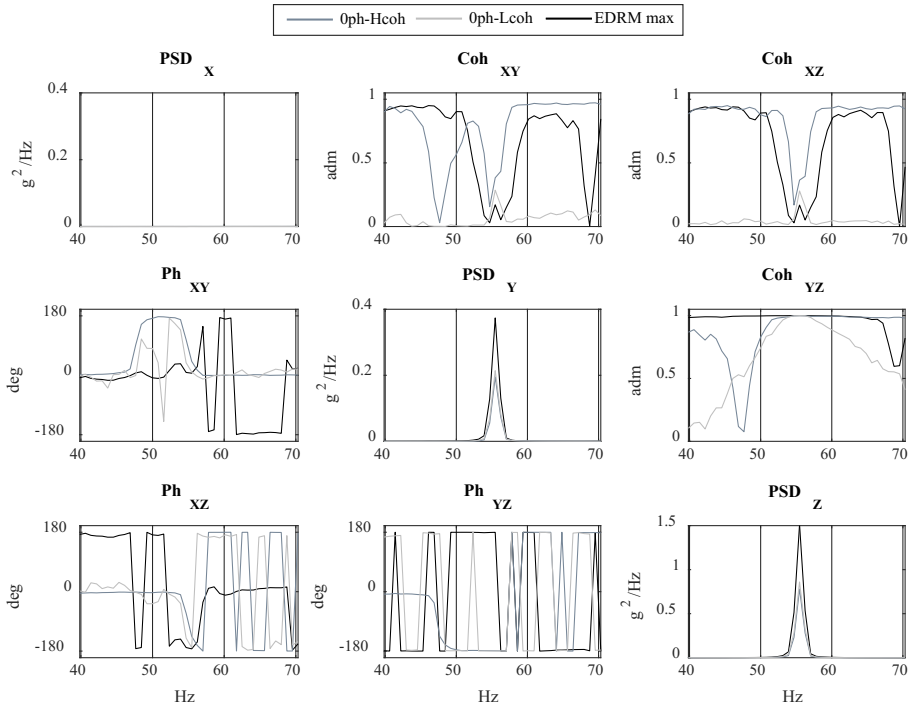

Figure 63: Short test campaign: *Tip* SDM. Zoom around Mode I (56 Hz).

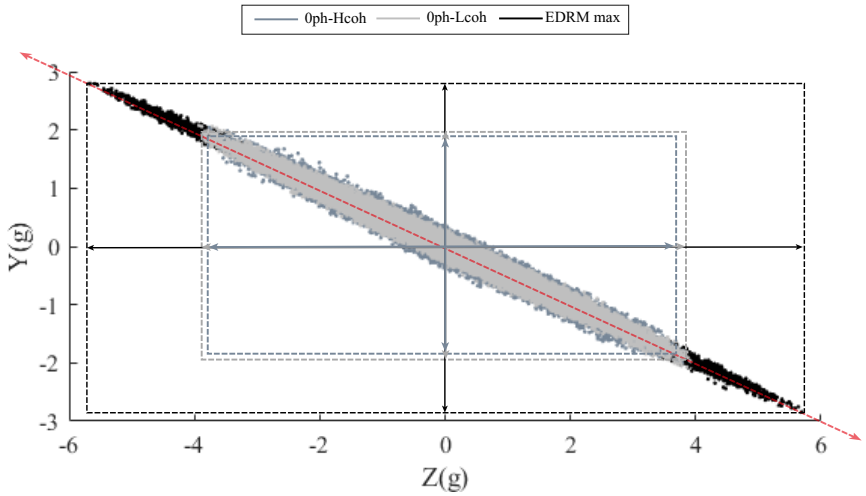

Figure 64: Short test campaign: scatter plots of the acceleration signals measured on the *Tip* along Y and Z directions ($X \simeq 0$). The signals are filtered in the narrow band of Mode I (56 Hz).

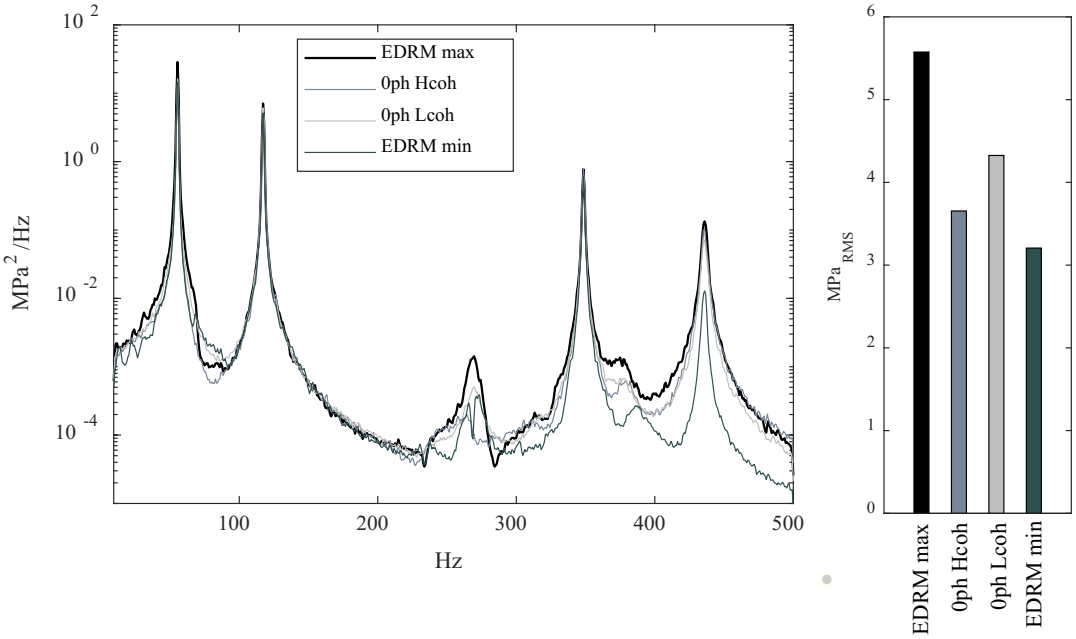

Figure 65: Short test campaign: von Mises stress.

of accelerometer *Tip*, respectively. Both the figures compare the results of the *0ph-Hcoh Method*, the *0ph-Lcoh Method* and the *EDRM-max*, which are always the gray, light-gray and black curves, respectively. The comparison of Figure 63 point out that the responses which actively participate to *Mode I* (Y and Z directions), at the resonance frequency are perfectly correlated (same coherence and same phase shift). Moreover, once again the amplitude PSDs of the *EDRM-max* result to be higher with respect to the *0ph-Lcoh Method* and the *0ph-Hcoh Method*, more specifically the scale factor is 1.76 and 1.94, respectively. Finally, Figure 64 validates the analysis by showing the three data distributions identically oriented along the same accelerations resultant, but ellipses with different diameter lengths corresponding to the different capabilities of the various techniques on exciting the specific mode shape.

Finally, to conclude the short-tests analysis Figure 65 shows the PSD of the resulting von Mises stress and its corresponding RMS value (S_{vM} and σ_{vM}). For this comparison, the result of the *EDRM-min* has been included to highlight the two extreme values, which define the range of the possible solutions obtainable by the combination of the actual test specifications. In particular, the RMS

value of the *EDRM-max* is 1.72 times higher with respect to the *EDRM-min*. Considering the S-N curve parameters under random loading of Table 9 and applying the Dirlik' fatigue damage model for wideband process [78], an increment of the 70% of the equivalent stress RMS causes an estimated time-to-failure almost 5 times shorter. Despite this result is just an approximation that contains many uncertainties on the real fatigue-life durations, it provides a first evidence of the relevance of the MIMO control target definition on multi-axis accelerated fatigue testing.

The von Mises stress comparison of Figure 65 highlights an other remarkable outcome. The RMS value of the *0ph-Lcoh Method* is higher with respect to the *0ph-Hcoh Method*. Thus, the stress result is in contrast with the acceleration result depicted in Figure 53, which exhibits higher RMS value for the *0ph-Hcoh Method*. Theoretically, as explained in Section 5.2 with Equations (67) and (68), stress and acceleration SDMs are linked by the same amplification factor (K) because of the TFs relationships. However, this statement is frequency dependent. Thus, the acceleration and the stress RMS values of Figure 53 and Figure 65 can provide comparable results only if the amplification factor (K) between the two methods is constant for the entire frequency band of interest. As already documented above, the amplification of the specimen' dynamic response, provided by different MIMO target generation techniques, significantly changes depending on the excited mode shape. For instance, defining the scale factor between two different techniques (1) and (2) as

$$K^{(1)}_{(2)} = \frac{S^{(1)}_{TIP,jj}}{S^{(2)}_{TIP,jj}} \tag{83}$$

thus, the scale factor corresponding to *Mode I* of Figure 63 is $K^{Lcoh}_{Hcoh} = 1.10$, meaning that the *0ph-Lcoh Method* is slightly higher. For *Mode IV* of Figure 59 instead, $K^{Lcoh}_{Hcoh} = 0.67$ indicates acceleration responses 33% higher for the *0ph-Hcoh Method*. Of course, the same scale factors can be obtained by comparing the stress SDMs around *Mode I* and *Mode IV*. However, it should be considered that in the strain/stress analysis, slightly different scale factors at low frequencies can be more relevant with respect to larger differences at high frequencies. This is because the RMS value of the *0ph-Lcoh Method* is higher than the *0ph-Hcoh Method*.

Therefore, referring to the previous outcomes, it can be concluded that different MIMO target generation techniques provide different scale factors

between the dynamic responses of the specimen, depending on the excited mode shape. This fact implies that, if two different MIMO target techniques are used for performing a fatigue test which involves the excitation of multiple natural modes, thus the dynamic response of the specimen under test will not be equally scaled in the entire frequency band of interest. Indeed, the natural modes will be excited with different intensity in accordance with the capability of each technique. This means that each mode shape provides a different contribution in the fatigue damage accumulation of the specimen, leading to a different fatigue failure mode.

5.4.3 *Fatigue-test analysis*

In order to validate the outcomes of the short-test analysis and to assess the impact of the MIMO control target on the fatigue-life of the specimen, a series of multi-axial random control tests has been carried out until the total breakage of the test specimens. The objective of the fatigue-testing campaign is thus to experimentally establish the S-N curve under different MIMO target generation techniques. In particular, the analysis compares the novel proposed *EDRM-max* and the *0ph-Lcoh Method*, that is the most commonly used procedure in standard practice.

The setup configuration is the same used for the short-testing campaign, shown in Figure 46. For each control test, the accelerations of the table and of the lumped mass are measured by means of the two tri-axial accelerometers *Tab* and *Tip*, respectively. However, strain measurements cannot be carried out for all the fatigue tests, due to cost reasons. Therefore, the stress SDM and the corresponding von Mises PSD are numerically calculated starting from the *Tip* SDM (measured during the actual fatigue test) and with the TFs matrix of Figure 66 (estimated on *Spec-0* during the pre-test phase of the short-testing analysis by means of the strain gauge rosette).

In accordance with the standard guidelines [97], to reasonably approximate the S-N curve by a straight line in the high-cycles fatigue region, the total number of specimens to be tested and the number of stress levels should be properly choosen. Table 11 classifies the resulting type of test in accordance

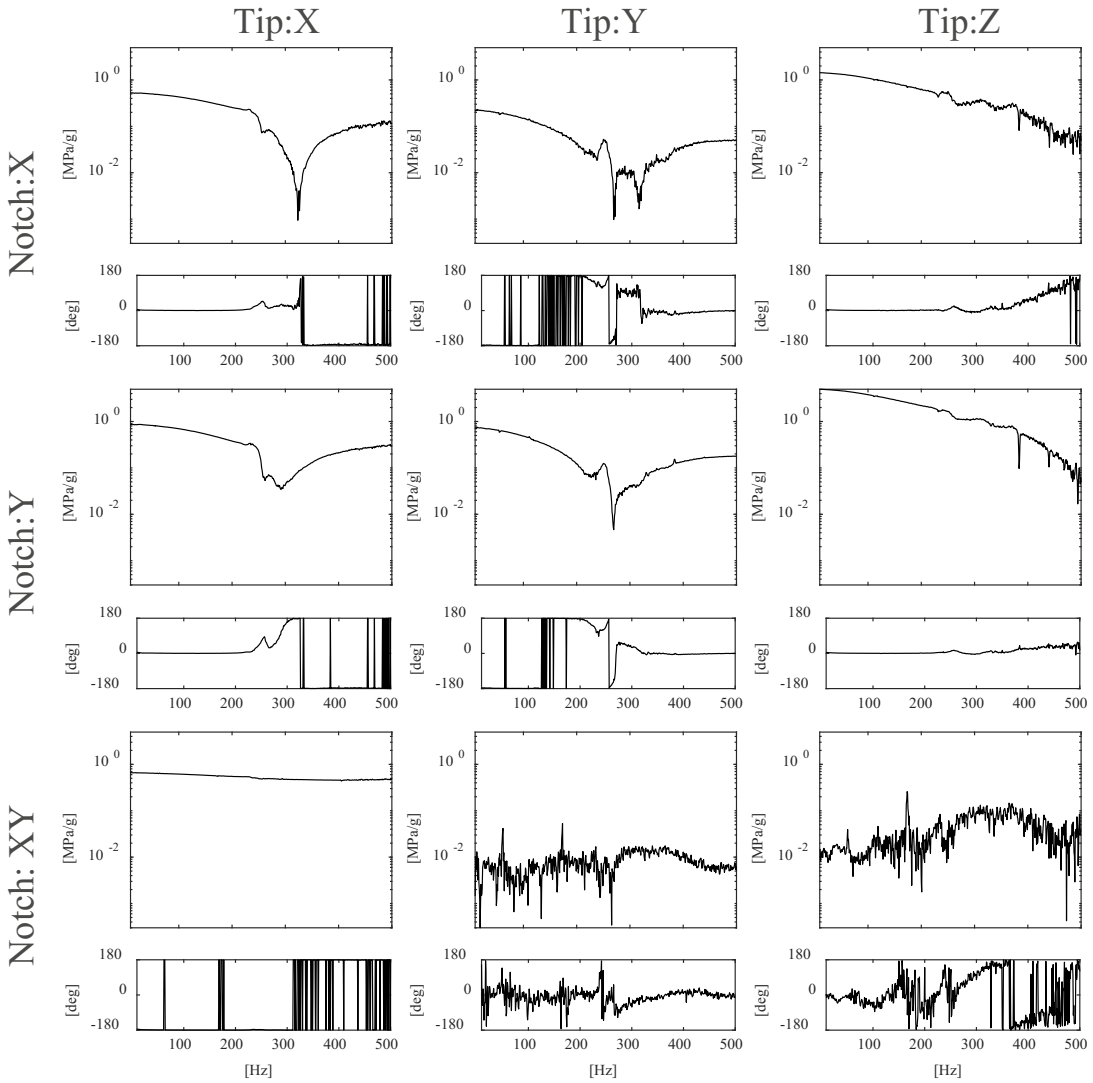

Figure 66: 3x3 Transfer Functions matrix ($\hat{\mathbf{H}}_{\sigma a}$) between *Tip* accelerometer (inputs) and *Notch* strain gauge rosette (outputs), estimated on *Spec*-0.

Table 11: Standard guidelines to estimate the S-N curve from testing data [97]

Type of Test	Minimum Number of Specimens	% Replication
Preliminary and Exploratory	$6 \div 12$	$17 \div 33$
Reaserch and Development	$6 \div 12$	$33 \div 50$
Design Allowables Data	$12 \div 24$	$50 \div 75$
Reliability Data	$12 \div 24$	$75 \div 88$

with the minimum number of tested samples and the *Percent Replication*, defined as [98]

$$\%\text{Rep} = 100\left[1 - \frac{N_{level}}{N_{spec}}\right] \tag{84}$$

where N_{level} is the total number of stress levels and N_{spec} is the total number of specimens. Following these standard rules, 12 specimens have been chosen as total number of samples to be tested at 3 different stress levels, i.e. 4 specimens to be tested at each level. With these data, the *Percent Replication* is equal to 75% and the type of test result to be between the 3rd and 4rd classes, which statistically guarantees a good S-N curve approximation from the experimental data.

The test specifications are flat PSDs (white noise) with the same RMS value for all the three control directions of accelerometer *Tab*. For the definition of the three test levels, in agreement to the test durations predicted by the fatigue damage model, values of 1.2, 1.7 and 2.4 gRMS guarantee the specimen breakage in the high-cycle fatigue region ($10^4 \div 10^6$ cycles), thus neglecting the effects of possible localized yielding at the crack.

Moreover, the short-testing analysis described in the previous section underlines that the MIMO target technique can effect the specimen' fatigue damage accumulation, providing altered scale factors for each excited mode shape. In order to validate the aforementioned results, the two MIMO target generation techniques (*EDRM-max* and *0ph-Lcoh Method*) will be compared in two distinct excitation bandwidths:

i) *Single-Mode Excitation*. The excitation bandwidth is $[10 \div 85]$ Hz and it guarantees the excitation of the only first bending mode of the specimen (*Mode I* at 56 Hz).

ii) *Multi-Mode Excitation*. The excitation bandwidth is $[10 \div 200]$ Hz and it guarantees the simultaneous excitation of the first two bending modes of the specimen (*Mode I* at 56 Hz and *Mode II* at 118 Hz).

The frequency bands are defined with the purpose to keep excited the modal shapes of the specimen, even during the decay of the natural frequencies due to the propagation of the crack. This technique is in agreement with the physics of fatigue tests, where the resonances of the specimen are excited throughout the entire duration of th test [99]. This choice is also in accordance with the actual testing required by standards [4].

Therefore, 48 tests are performed in total, subdivided into different typologies: 24 tests are conducted in single-mode excitation (12 tests for each MIMO target technique) and 24 in multi-mode excitation (12 tests for each MIMO target technique). As a result, 4 different S-N curves will be experimentally estimated.

It is worth to notice that, in order to reduce the uncertainties on the experimental data and to increase the repetition accuracy of the measurements, all the specimens have been obtained from the same batch of aluminium planks and clamped on the fixture with a torque wrench. Moreover, a preventive analysis was carried out by comparing the dynamic properties of all the test specimens, in order to detect possible processing defects which can effect the specimen structure and thus alter the modal parameters. Figure 67 shows the comparison of the estimated TFs between *Tab* and *Tip* accelerometers. In particular, the figure compares the amplitude and the frequency of the peaks corresponding to the first two bending modes of the specimens. In Figure 67 the boxplot representation [100] is adopted to identify possible outliers in the statistical sample. Since the method does not require a priori knowledge of the statistical data distribution, it is a useful toll to initially show the spread of the data set. In the boxplot rappresentation, the central mark of box indicates the median. The bottom and top edges of the box indicate the first quartile (Q_1) and the third quartile (Q_3), respectively. Thus, the 25% of the data fall below Q_1 and the 75% are above Q_3. The entire box, named *Interquartile Range* (*IQR*), shows the middle 50% of scores (the range between the 25th and 75th

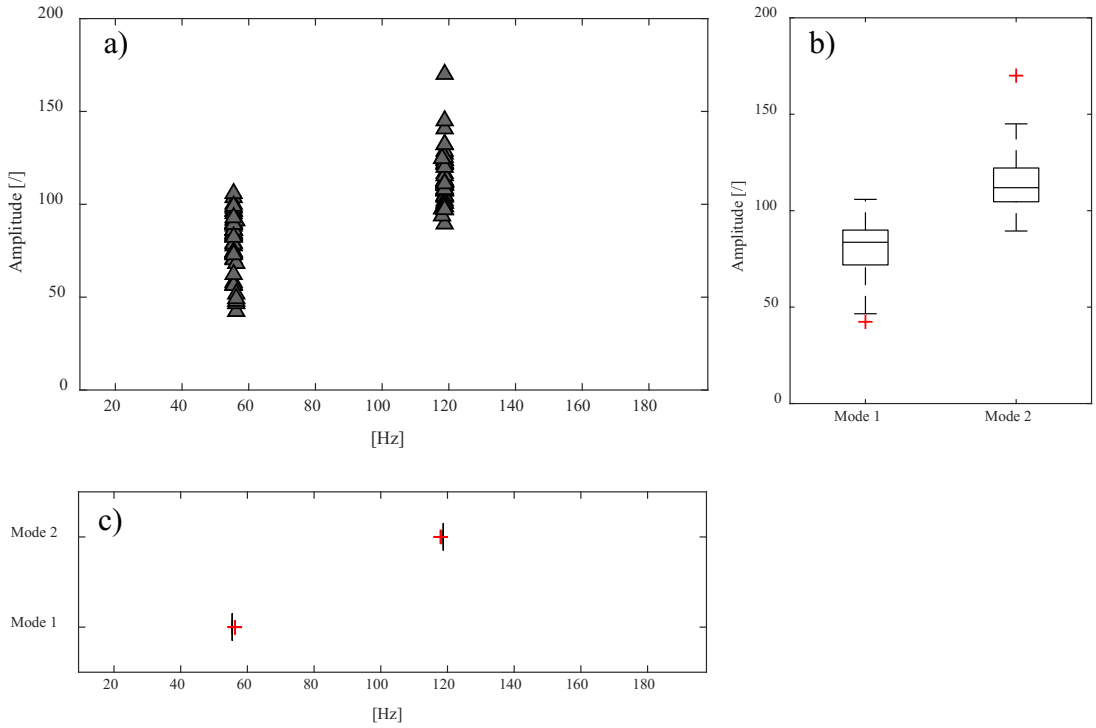

Figure 67: Fatigue test campaign: pre-test analysis of the specimens dynamic properties for outliers investigation. a) peaks detection at resonance conditions of the estimated TFs between *Tab* and *Tip* accelerometers. b) boxplot representation comparing the amplitude values of the resonance peaks. c) boxplot representation comparing the frequency values of the resonance peaks. Red-cross symbols indicate outliers

percentile). The whiskers extend to the most extreme data points (not considering outliers) and they are useful for providing a visual indicator regarding the spread of the data. Outliers are defined as data points that are located outside 1.5 times the *IQR* [101], i.e. outside the whiskers of the boxplot. In Figure 67 the outliers are individually plotted using a red-cross symbol. It is important to underline that, all the specimens detected as outliers have been removed from the presented results, in order to guarantee the minimum source of uncertainty in this fatigue testing analysis.

5.4.3.1 *Single-mode excitation*

The results of the fatigue-testing campaign in single-mode excitation are shown in Figure 68. In particular, the figure offers two different diagrams; the plot in the upper part of the figure compares the results in terms of RMS of the recorded accelerations of the table (a_{Tab}) and the corresponding time-to-failure in seconds. It can be noted as the RMS levels (a_{Tab}) represented in ordinates are greater than the reference excitation levels at each control axis (1.2, 1.7 and 2.4 gRMS). In fact, since the excitation is applied at the same time in three control directions, the square root of the squares sum of the measured RMS values on each control axis has been chosen as equivalent RMS value of the table accelerations

$$a_{Tab} = \sqrt{a_{Tab,X}^2 + a_{Tab,Y}^2 + a_{Tab,Z}^2} \tag{85}$$

It is worth to notice that this values corresponds to the RMS value of the trace of the control SDM, and therefore it could be the proper datum to provide the overall energy employed for exciting the specimen.

The upper diagram of Figure 68 highlights the potential of the novel proposed MIMO target generation technique (*EDRM-max*) with respect to the most common in standard practice (*0ph-Lcoh Method*), depicted in gray and dark symbols, respectively. The *EDRM-max* is capable of fully exploiting the total energy of the table by proper combining the test specifications. As a result, the dynamic response of specimen is maximised and the resulting time-to-failure significantly shortened. It can be seen that the durations resulting from the *EDRM-max* are comparable with the ones of the *0ph-Lcoh Method* corresponding to the next-higher excitation level.

The second diagram in the bottom part of Figure 68 instead, reports the results of the fatigue tests in terms of RMS value of the actual von Mises equivalent stress (σ_{vM}) and the corresponding total number of cycles to failure (N0). In particular, since the response to the single-mode excitation is a narrow-band process ($\alpha_2 = 0.996$), the total number of cycles has been calculated by multiplying the expected number of zero up-crossing per second (Equation 55) with the total test duration in seconds ($N0 = n_0^+ T$). Of course, the stress-cycles results confirm the previous outcomes shown in the acceleration-duration diagram, i.e. the results of *EDRM-max* are comparable with the ones of the next-higher excitation level in the *0ph-Lcoh Method*. However, the most notable

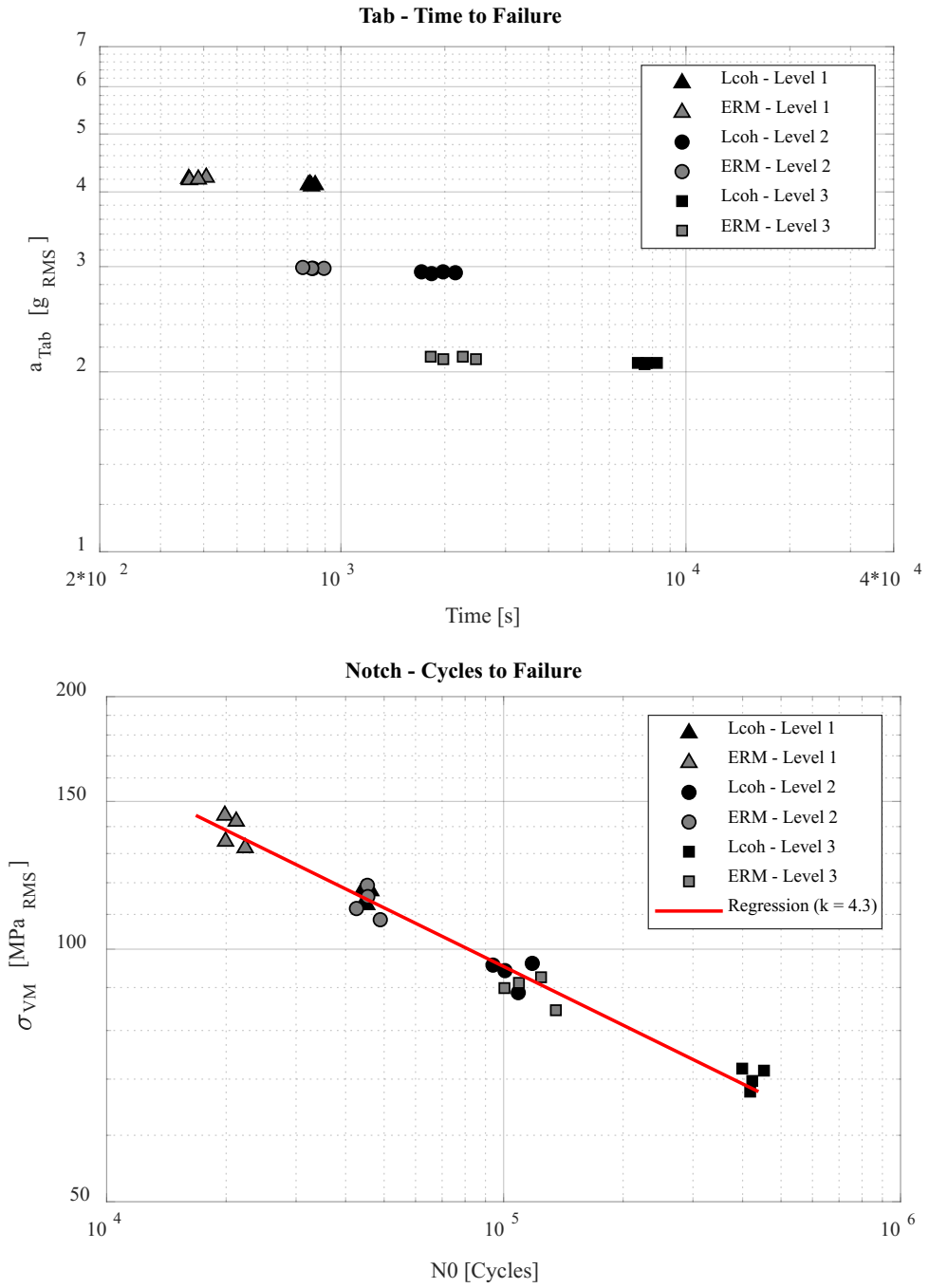

Figure 68: Fatigue test campaign: single-mode excitation results.

Table 12: Test data report of the fatigue tests carried out with the *0ph-Lcoh* method in single-mode excitation. $a_{Tab} = \sqrt{a_{Tab,X}^2 + a_{Tab,Y}^2 + a_{Tab,Z}^2}$; $a_{Tip} = \sqrt{a_{Tip,X}^2 + a_{Tip,Y}^2 + a_{Tip,Z}^2}$; TtF = Time-to-Failure; $N0 = n_0^+ T$.

	Test	a_{Tab}	a_{Tip}	TtF	σ_{vM}	N0
	#	[g_{RMS}]	[g_{RMS}]	[min]	[MPa_{RMS}]	[Cycles]
	1	4.1	31.0	14.0	117.3	$4.6 * 10^4$
	2	4.1	31.1	13.4	117.8	$4.4 * 10^4$
Level 1	3	4.1	29.8	13.7	113.0	$4.5 * 10^4$
2.4 g_{RMS}	4	4.1	30.1	13.6	113.9	$4.5 * 10^4$
	mean	4.1	30.5	13.7	115.5	$4.5 * 10^4$
	std	0	0.6	0.2	2.4	$0.9 * 10^3$
	5	2.9	25.3	35.80	96.2	$1.2 * 10^5$
	6	2.9	24.8	30.5	94.3	$1.0 * 10^5$
Level 2	7	2.9	23.4	33.0	88.8	$1.1 * 10^5$
1.7 g_{RMS}	8	2.9	25.2	28.5	95.7	$0.9 * 10^5$
	mean	2.9	24.7	32.0	93.8	$1.1 * 10^5$
	std	0	0.9	3.2	3.4	$1.0 * 10^4$
	9	2.1	17.8	126.5	67.6	$4.2 * 10^5$
	10	2.1	18.9	120.9	72.1	$4.0 * 10^5$
Level 3	11	2.1	18.3	128.2	69.7	$4.2 * 10^5$
1.2 g_{RMS}	12	2.1	18.8	137.3	71.7	$4.5 * 10^5$
	mean	2.1	18.5	128.2	70.3	$4.2 * 10^5$
	std	0	0.5	6.8	2.1	$2.2 * 10^4$

Table 13: Test data report of the fatigue tests carried out with the *EDRM-max* in single-mode excitation. $a_{Tab} = \sqrt{a^2_{Tab,X} + a^2_{Tab,Y} + a^2_{Tab,Z}}$; $a_{Tip} = \sqrt{a^2_{Tip,X} + a^2_{Tip,Y} + a^2_{Tip,Z}}$; TtF = Time-to-Failure; $N0 = n_0^+ T$.

	Test	a_{Tab}	a_{Tip}	TtF	σ_{vM}	N0
	#	[g_{RMS}]	[g_{RMS}]	[min]	[MPa_{RMS}]	[Cycles]
	1	4.2	37.9	6.0	144.4	$2.0 * 10^4$
	2	4.2	34.8	6.8	132.1	$2.2 * 10^4$
Level 1	3	4.2	35.4	6.1	134.4	$2.0 * 10^4$
2.4 g_{RMS}	4	4.2	37.4	6.4	142.0	$2.1 * 10^4$
	mean	4.2	36.4	6.3	138.2	$2.1 * 10^4$
	std	0	1.5	0.4	5.9	$1.8 * 10^3$
	5	3.0	31.3	13.8	119.1	$4.5 * 10^4$
	6	3.0	28.5	14.9	108.4	$4.9 * 10^4$
Level 2	7	3.0	30.4	13.7	115.5	$4.5 * 10^4$
1.7 g_{RMS}	8	3.0	29.4	12.9	111.8	$4.6 * 10^4$
	mean	3.0	29.9	13.8	113.7	$4.6 * 10^4$
	std	0	1.2	0.8	4.6	$2.6 * 10^3$
	9	2.1	24.3	37.6	92.6	$1.2 * 10^5$
	10	2.1	23.6	30.4	89.9	$1.0 * 10^5$
Level 3	11	2.1	23.9	33.0	91.2	$1.1 * 10^5$
1.2 g_{RMS}	12	2.1	22.2	41.0	84.6	$1.4 * 10^5$
	mean	2.1	23.5	35.5	89.6	$1.2 * 10^5$
	std	0	0.9	4.7	3.5	$1.6 * 10^4$

result here is that the distribution of the experimental data points of both the procedures can be approximate in a least squares sense by the same straight line, red depicted in the figure. In fact, in logarithmic scale Equation (49) represents a straight line with slope k. In this case, a slope k equal to 4.3 provides the best fit of the linear regression to the experimental data of both the two procedures. Since the application of the *EDRM-max* and the *0ph-Lcoh Method* leads to the same approximation of the S-N curve, it is reasonable to conclude that the two procedures cause the same fatigue damage and thus the same mechanism of crack on the specimen.

Furthermore it is worth to notice that, with the single-mode excitation just the first bending mode of the specimen is excited during the fatigue test. In accordance with the results presented in the short-testing analysis of Section 5.4.2, if just one mode shape is excited, then the response SDMs resulting from the *EDRM-max* and from the *0ph-Lcoh Method* are simply scaled between each other, with a constant scale factor in the entire frequency band of interest. This case is perfectly in agreement with the assumptions taken by Allegri and Zhang in [70] to provide the general scaling law for accelerated multi-axis fatigue testing (Equation 66). In this context, the *EDRM-max* can be considered as a methodology able to accelerate the fatigue test with respect to the standard *0ph-Lcoh Method*, because it induces the same fatigue damage in a shorter time.

Finally, Tables 12 and 13 summarise the experimental data obtained during the single-mode excitation with the *0ph-Lcoh Method* and *EDRM-max*, respectively. In addition to the experimental results of each single test, the tables provide also some statistics such as the mean and the standard deviation of the data calculated for each excitation level.

5.4.3.2 *Multi-mode excitation*

The results of the fatigue tests conducted in multi-mode excitation are depicted in Figure 69. Also in this case, the figure presents two different diagrams: in the top, the overall RMS value of the table accelerations (a_{Tab}) is plotted against the time-to-failure in seconds; in the bottom instead, the RMS value of the equivalent von Mises stress (σ_{vM}) is represented against the total number of cycles (N0). Considering the acceleration-duration diagram, once again the capabilities of the *EDRM-max* on reducing the time-to-failure of the specimen are significant with respect to the *0ph-Lcoh Method*. In particular, the test data

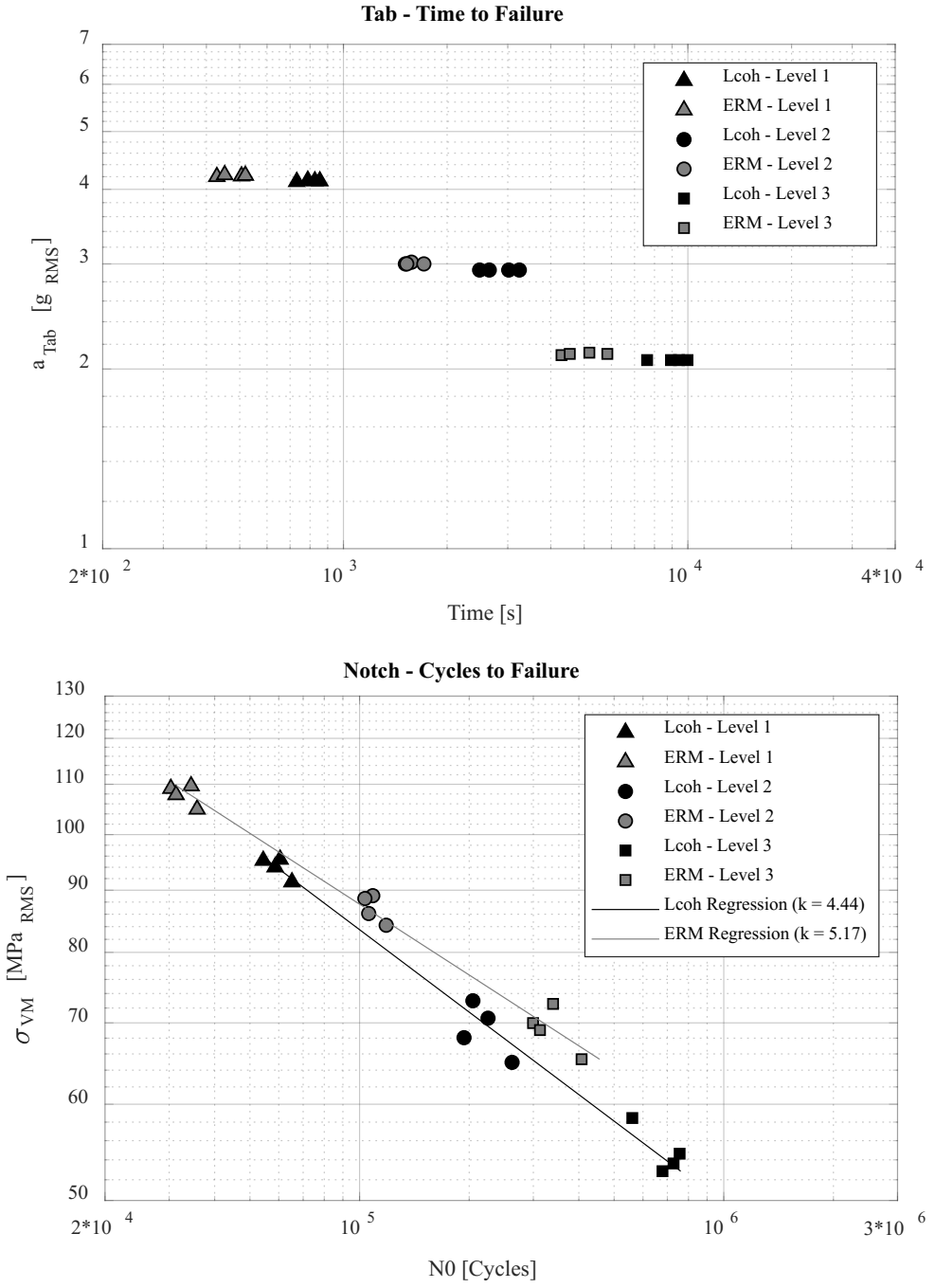

Figure 69: Fatigue test campaign: multi-mode excitation results.

Table 14: Test data report of the fatigue tests carried out with the *0ph-Lcoh* method in multi-mode excitation. $a_{Tab} = \sqrt{a^2_{Tab,X} + a^2_{Tab,Y} + a^2_{Tab,Z}}$; $a_{Tip} = \sqrt{a^2_{Tip,X} + a^2_{Tip,Y} + a^2_{Tip,Z}}$; TtF = Time-to-Failure; $N0 = n^+_0 T$.

	Test	a_{Tab}	a_{Tip}	TtF	σ_{vM}	N0
	#	[g_{RMS}]	[g_{RMS}]	[min]	[MPa_{RMS}]	[Cycles]
	1	4.1	43.1	13.1	94.0	$5.9 * 10^4$
	2	4.1	42.6	13.8	95.4	$6.1 * 10^4$
Level 1	3	4.1	43.5	12.2	95.2	$5.4 * 10^4$
2.4 g_{RMS}	4	4.1	43.6	14.2	91.4	$6.5 * 10^4$
	mean	4.1	43.2	13.3	94.0	$6.0 * 10^4$
	std	0	0.5	0.9	1.8	$4.5 * 10^3$
	5	2.9	35.2	44.2	73.0	$2.0 * 10^5$
	6	2.9	33.4	54.0	65.0	$2.6 * 10^5$
Level 2	7	2.9	33.1	41.4	68.1	$1.9 * 10^5$
1.7 g_{RMS}	8	2.9	32.4	50.3	70.6	$2.3 * 10^5$
	mean	2.9	33.5	47.5	69.2	$2.2 * 10^5$
	std	0	1.2	5.7	3.4	$3.0 * 10^4$
	9	2.1	26.1	126.9	58.5	$5.6 * 10^5$
	10	2.1	25.9	157.1	53.6	$7.3 * 10^5$
Level 3	11	2.1	25.5	166.2	54.6	$7.6 * 10^5$
1.2 g_{RMS}	12	2.1	24.9	148.9	52.9	$6.8 * 10^5$
	mean	2.1	25.6	149.8	54.9	$6.8 * 10^5$
	std	0	0.5	16.8	2.5	$8.6 * 10^4$

Table 15: Test data report of the fatigue tests carried out with the *EDRM-max* in multi-mode excitation. $a_{Tab} = \sqrt{a^2_{Tab,X} + a^2_{Tab,Y} + a^2_{Tab,Z}}$; $a_{Tip} = \sqrt{a^2_{Tip,X} + a^2_{Tip,Y} + a^2_{Tip,Z}}$; TtF = Time-to-Failure; $N0 = n_0^+ T$.

	Test	a_{Tab}	a_{Tip}	TtF	σ_{vM}	N0
	#	[g_{RMS}]	[g_{RMS}]	[min]	[MPa_{RMS}]	[Cycles]
	1	4.2	46.1	7.2	109.1	$3.0 * 10^4$
	2	4.2	43.9	7.5	107.8	$3.1 * 10^4$
Level 1	3	4.2	43.9	8.4	109.7	$3.4 * 10^4$
2.4 g_{RMS}	4	4.2	42.6	8.7	104.9	$3.6 * 10^4$
	mean	4.2	44.1	8.0	107.9	$3.3 * 10^4$
	std	0	1.5	0.7	2.1	$2.6 * 10^3$
	5	3.0	36.2	26.3	89.1	$1.1 * 10^5$
	6	3.0	35.5	25.2	88.6	$1.0 * 10^5$
Level 2	7	3.0	35.5	25.2	86.1	$1.1 * 10^5$
1.7 g_{RMS}	8	3.0	34.4	28.5	84.2	$1.2 * 10^5$
	mean	3.0	35.4	26.4	87.0	$1.1 * 10^5$
	std	0	0.7	1.5	2.3	$6.5 * 10^4$
	9	2.1	27.0	97.3	65.3	$4.1 * 10^5$
	10	2.1	29.1	71.0	70.0	$3.0 * 10^5$
Level 3	11	2.1	28.0	75.7	69.1	$3.1 * 10^5$
1.2 g_{RMS}	12	2.1	27.3	86.3	72.6	$3.4 * 10^5$
	mean	2.1	27.8	82.7	69.3	$3.4 * 10^5$
	std	0	0.9	11.5	3.0	$4.8 * 10^4$

shown in Table 14 and Table 15 underline that, the mean values calculated over the test durations of each excitation level resulting from the *EDRM-max* are between the 39% and the 45% shorter than the ones from the *0ph-Lcoh Method*. About the 40% of time-reduction is a remarkable achievement if one considers that the total energy utilized for exciting the specimen is the same and the way of combining the test specifications is the only different between the two MIMO target procedures.

The stress-cycles diagram in the bottom of Figure 69 instead, exhibits different results with respect to the case of single-mode excitation. In fact, the experimental data points of the two techniques are approximated by two distinct linear regressions. In particular, the parameters of the S-N curves resulting from the regression calculation are $k = 4.44$ $C = 3.36 * 10^{13}$ for the *0ph-Lcoh Method*, and $k = 5.17$ $C = 1.09 * 10^{15}$ for the *EDRM-max*.

In order to critically analyse these results, it is worth remembering that during the multi-mode excitation, the frequency band of excitation covers the first two natural frequencies of the specimen. Therefore, the bending mode on the Y-Z plane (*Mode I*) and the bending mode on the X-Y plane (*Mode II*) are simultaneously excited during the fatigue test. As it has been observed in the previous short-testing analysis, when multiple mode shapes are concurrently excited, the response SDMs resulting from different MIMO target techniques are diversely scaled at distinct natural frequencies. The scale factor between the response SDMs varies according to the capabilities of the adopted technique of better exciting the specific mode shape. As a consequence, the contribution on the fatigue damage of each single mode is different for different MIMO target techniques. Therefore, the two different linear regressions of Figure 69 confirm that, in multi-mode excitation, *EDRM-max* and *0ph-Lcoh Method* produce a different fatigue damage accumulation and a different crack propagation on the specimen under test.

5.4.3.3 *Fracture surface analysis*

Objective of this section is to conclude the analysis of the fatigue-testing campaign providing the results of the macroscopic visual examination of the specimen fracture surfaces. It is important to underline that, the aim of this analysis is to determine the overall appearance of the fractured surface and to compare the macro-effects (beach marks, ratchet lines, surface flatness, etc.) caused by the use of different MIMO target techniques. Thus, the photographs

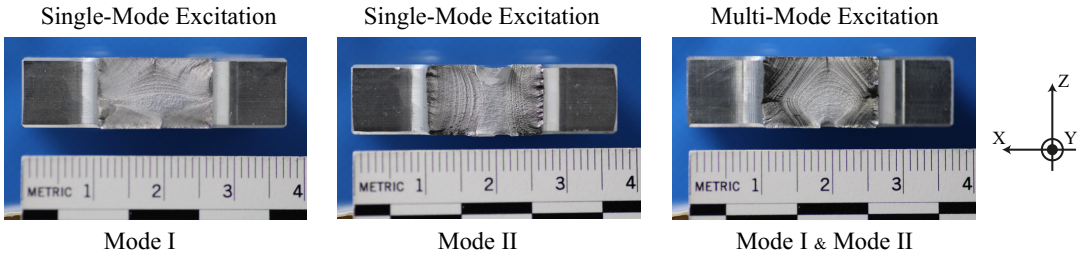

Figure 70: Fatigue test campaign: comparison of the fracture surface obtained by varying the frequency band of excitation. Mode I = [10-85] Hz (left); Mode II = [85-200] Hz (middle); Mode I & II = [10-200] Hz (right)

shown in the following of this section, have been taken by using *Canon EOS M6* mirrorless digital camera with Tokina 100 mm lens in a led light set-up, which provides images suitable for a good macroscopic examination of the specimen' fracture surface.

For the sake of completeness, before showing the comparison of the results deriving from the use of different MIMO target techniques, Figure 70 point out the features of the fracture surface when varying the frequency band of excitation. In particular, the figure compares the results when the first two natural modes are individually or simultaneously excited; The photos on the left side and in the middle of Figure 70 represent the single excitation of *Mode I* and *Mode II*, respectively. The orientation of the beach markers clearly highlights the different plane of bending of the two mode shapes. The last photo instead, on the right side of Figure 70, shows the fracture surface of a specimen subjected to the concurrent action of both mode shapes, i.e. *Mode I* and *Mode II* simultaneously. As one would expect, the crack propagation and the final fracture region are combinations of the two cases previously investigated.

Finally, Figure 71 and Figure 72 compare the fracture surfaces resulting from the application of the *0ph-Lcoh Method* and the *EDRM-max* during single-mode excitation and multi-mode excitation, respectively. First of all, it is worth noting that all the fracture surfaces are flat, which indicates the absence of plastic deformation during the fatigue process [102]. In addition to the photos of the specimen' cross-section, the PSDs of the respective von Mises equivalent stress are depicted in the top of the figures, in order to highlight the existing correlation between the stress state and the failure mode of the specimens. The

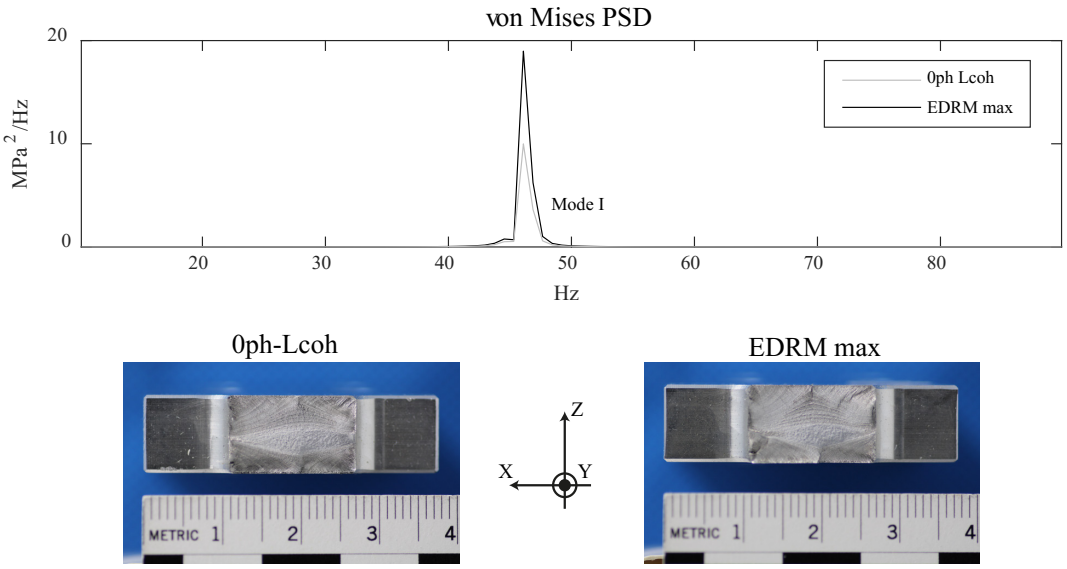

Figure 71: Fatigue test campaign: comparison of the fracture surface obtained by varying the target generation technique during the single-mode excitation.

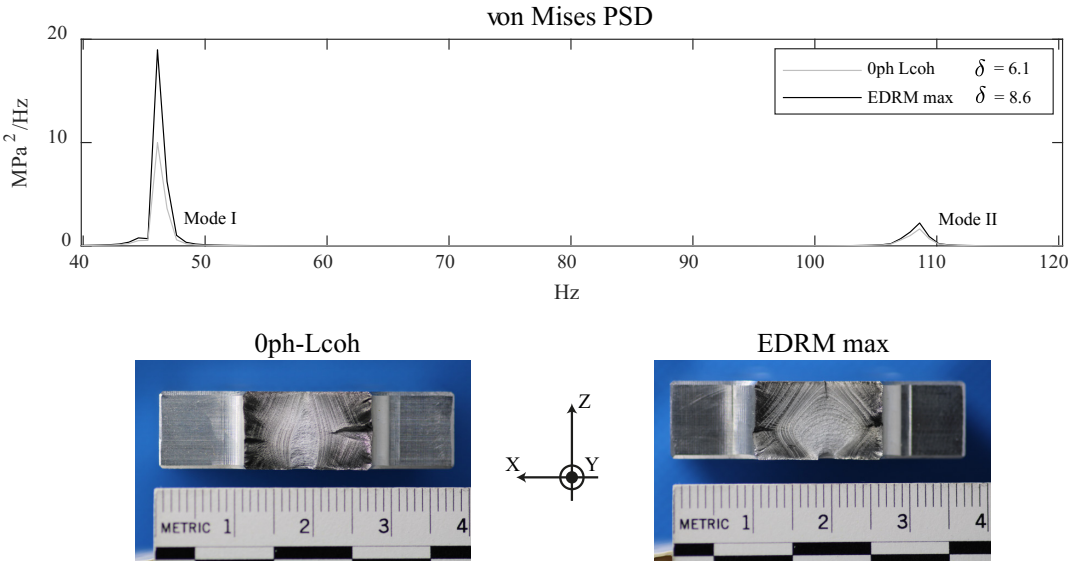

Figure 72: Fatigue test campaign: comparison of the fracture surface obtained by varying the target generation technique during the multi-mode excitation.

figures confirm and validate the outcomes proposed in the previous section. In fact, the fracture surfaces produced by the *0ph-Lcoh Method* and by the *EDRM-max* during single-mode excitation (Figure 71), are very similar and comparable. All the various stages of the fracture appear to be practically identical, i.e. the crack nucleation, the crack propagation and the final separation. The section corners are the four major crack initiation sites. Two evident ratchet marks on the long sides of the section reveal where the cracks have been coalesced. The final fracture zone is in the middle portion of the section and it is stretched in X-direction, in accordance with the excited mode that is the bending mode on the YZ plane. The identical fracture surfaces are in compliance with the previous results show in Figure 68, where the experimental data set of the two techniques are approximated by the same linear regression.

Figure 69 instead, compares the two techniques during the multi-mode excitation. In this case, the two fracture surfaces present some differences. The beach markers by going side to side into the cross-section, define different arch-shaped lines which point out a different direction of the crack propagation [103]. Furthermore, the shapes of the final fracture regions are different. In particular, the final fracture of the *EDRM-max* is more stretched along the X-direction than the one of the *0ph-Lcoh Method*, suggesting a greater contribution of the first bending mode. The von Mises PSDs, plotted in the top of Figure 69, support these results. The δ values, shown in the legend, correspond to the ratio between the amplitudes of the von Mises PSD at the two natural frequencies ($\delta = S_{vM}(f_{n,I})/S_{vM}(f_{n,II})$). *EDRM-max* exhibits an higher δ value, thus confirming the prevalence of *Mode I* in the propagation of the crack and in the subsequent failure mode. Therefore, obtaining two different fracture surfaces between the two target techniques is in accordance with the result shown in Figure 69, where the experimental data set of the two techniques are approximated by two different linear regressions.

Furthermore, it is worth specifying that just one fracture surface for each type of testing methodology has been shown in this section analysis. However, the crack surface has been checked for all the tested specimens, and all of them confirmed the shapes explained above and reported in Figure 71 and Figure 72.

5.5 CONCLUDING REMARKS

The purpose of the research activity presented in this chapter is to critically investigate the effects produced by the use of different MIMO control target generation techniques on the fatigue-life of components subjected to environmental control test. Nowadays, to assess in the laboratory the durability of specimens by means of multi-axis random vibration control test, the standard guidelines suggest to combine the test specifications following the *0ph-Lcoh Method*, i.e. defining the control SDM with decorrelated test specifications. Undoubtedly, this methodology is the easiest procedure to define the control target without any prior knowledge of the real vibration environment. However, the present work shows that different solutions adopted for combining the test specifications can seriously alter the response dynamic of the specimen under test and thus change the results of the durability test. Moreover, the original contribution of this chapter is to provide a novel technique for the definition of the MIMO control target which is capable of maximizing the resulting response dynamic of specimen. This means to subject the specimen to the most extreme environmental vibration obtainable from the combination of the standard test specifications.

An experimental campaign has been carried out on the three-axial electrodynamic shaker a the University of Ferrara, performing multi-axial random vibration control tests on notched specimens made of aluminium alloy. The test campaign has been divided in two main test activities: a short-testing campaign and a fatigue-testing campaign. In the short-testing campaign, the same specimen has been subjected to multiple random vibration control tests of a duration of two minutes. Each short-test has been carried out by using a different MIMO target generation technique, in order to finally compare the effects of each procedure on the same specimen. This first test campaign pointed out remarkable results. In particular, the novel presented technique *EDRM max/min* always guarantees the proper combination of the test specifications to get out the maximum/minimum specimen dynamic in terms of both acceleration responses or strain/stress. Thus, all the results deriving from other solutions are between the two extreme values defined by the *EDRM max/min*, evidently including the commonly used solution *0ph-Lcoh Method*. De facto, this analysis has highlighted the limitations of the standard guidelines on multi-axis vibration control testing. The short-test results demonstrated that

the solution suggested by Standards causes a vibration environment which is not the extreme possible. This means that, possibly, the real operative conditions can be more severe with respect to the laboratory ones. The *EDRM max* overcomes this limit by proper combing the tests specifications and better exciting all the existing mode shapes of the specimen.

In the fatigue-testing campaign instead, 48 specimens have been tested until rupture for comparing the proposed *EDRM-max* with the *0ph-Lcoh Method* in terms of fatigue damage, failure modes and durations of the notched specimens. In this case, the final objective of the test campaign was to experimentally establish the S-N curves during single-mode excitation and during multi-mode excitation. For both the excitation bandwidths, the *EDRM-max* has provided significantly shorter time-to-failure values than the *0ph-Lcoh Method*, thus confirming the evident potential shown during the short-test analysis. Moreover, interesting results have been obtained from the comparison of the estimated S-N curves. In single-mode excitation, the experimental data set deriving from the two MIMO target techniques have been approximated (in a least squares sense) by the same straight line. This means that the specimens exhibit the same fatigue behaviour independently on the adopted MIMO target technique. This result has been confirmed by the analysis on the fracture surfaces that have been found practical identical. In this context, the *EDRM-max* can be considered as a methodology to accelerate the fatigue test, because it produce the same fatigue damage in a shorter time.

In multi-mode excitation instead, the two techniques under investigation have shown S-N curves approximated from two distinct linear regressions and fracture surfaces with distinct macroscopical features. These results clearly highlight that the two techniques induce into the specimens a different fatigue damage accumulation and thus a different failure mode. In this context, it has been demonstrated that, when multiple natural modes are simultaneously excited, different combinations of the test specifications produce different fatigue behaviours of the specimen under test. Therefore it can be concluded that, the fatigue behaviour of the specimen in the operational environment can be replicate in the laboratory only if the MIMO control target is fully retrieved from the operational data, i.e. only if both the PSDs and the CSDs come directly from the operative conditions. All the other solutions (*0ph-Lcoh Method*, *0ph-Hcoh Method*, *EDRM-max*, etc.), which differently combine standard PSDs, will provide different fatigue behaviour and different failure modes

on the specimen tested in the laboratory. At least, if the CSDs data are not available, the *EDRM-max* ensures that the specimen is subjected to the most severe possible vibration environment. The resulting fatigue behaviour will be different from the operational one, but at least it will be the one with the shortest time-to-failure.

All the drawn observations have been obtained using ad-hoc machined specimens. However, despite the simple geometry involved, it is plausible that the outcomes of this work maintain validity also for real mechanical components.

6

CONCLUSIONS

The research activities presented in this thesis are part of the research project supported by the *Mech Vib*, Mechanics and Vibration Research Group at the University of Ferrara, which aims to develop novel multi-axis vibration testing methodologies by exploiting the 3-DoF shaker table, located in the laboratory of the Engineering Department. In 2017 in fact, the University of Ferrara purchased the *Dongling 3ES-10-HF-500*, an avant-garde excitation system capable of exciting test articles in three directions simultaneously. The opportunity to execute experimental campaigns with such an extremely innovative machine, provides the tools needed to perform advanced researching in the field of multi-axial environmental vibration control testing. De facto, nowadays the multi-axis dynamic testing is still considered as a pioneer application in the industrial practice, which is strongly related to single-axis testing based on SISO standards. In this context, the first purpose of this thesis has been to exploit the 3-DoF shaker table in order to highlight the advantages of using MIMO control strategy in laboratory dynamic testing. The experimental assessment presented in Chapter 3 compares the results of SISO and MIMO control strategies when performing sequential single-axis random control testing. Thus, in order to point out the different capabilities of the two control techniques, the same series of test has been carried out by using the 3-DoF shaker table of the University of Ferrara and a single axis shaker with similar performance characteristics. In particular, the experimental investigation has been focused on the analysis of the cross axis responses measured during the control test. Cross axis responses indicate the measuring vibration levels along the two axes orthogonal to the main axis of vibration (drive axis of excitation). It is worth to underline that, cross axis levels provide an indication on the quality

of the single axis test. High vibration levels measured on the cross axes means to subject the test article to undesired cross-excitations which can effect the resulting dynamic behaviour. In accordance with the Standard practice in fact, if the amplitude of the cross axis PSD is more than 0.2 times the amplitude of the required PSD on the drive axis of vibration, the single axis test should be deemed as invalid. Therefore, an EGR valve has been used as test article and a specifically designed fixture allowed the rotation of the specimen in the three single axis test configurations, i.e. transversal, longitudinal and vertical configuration, corresponding to the principal directions of the specimen. The results of the sequential single axis test campaign, have clearly revealed the enormous advantages deriving from the use of the MIMO control strategy. The MIMO configuration, firstly ensures to closely replicate the required PSD profile on the drive axis of vibration, and secondly (but equally important) it guarantees the simultaneous control of the cross axis vibrations below the acceptable thresholds, thus always meeting the Standard specifications. With the SISO control strategy instead, only the PSD profile on the drive axis of vibration is feedback controlled, while cross axes are free to respond according to the natural dynamic behaviour resulting from the coupling between test article and excitation system. The results of the control test have demonstrated that the SISO control strategy is not capable of managing cross axis resonances. At the most problematic frequencies, the vibration levels on the cross axis reached and exceeded the PSD profile in the main axis of vibration. More specifically, the cross axis PSDs have been found up to 14 dB higher that the permitted level, i.e. cross-PSD amplitudes 27 times higher than the acceptable threshold.

Therefore, the proposed experimental assessment has evidently proved the inadequacy of the SISO control strategy, also for performing very simple single axis control tests. In the light of what has been pointed out, the MIMO control strategy can significantly improve the test results, guaranteeing the full control of the entire vibration environment. It can be finally concluded that, this research activity has provided a further evidence on the benefits of the MIMO control to the environmental testing community. This positive contribution aims to definitively turn the multi-axis testing into the main reference procedure for practical environmental control test.

However, besides the experimental activity aimed at promoting the use of MIMO control, the main objective of the thesis is to investigate the definition

process of the MIMO control target. Throughout this manuscript in fact, it has been demonstrate that the challenges of MIMO random control start even before the actual test, or precisely in the test definition phase. The first step of any successful MIMO random control test is the proper definition of the control target, which is a full Spectral Density Matrix where the definition of each entrie of the matrix (PSD or CSD) is important and can alter the final result of the control test. The reference SDM can be entirely defined by means of field measured data. However, very often operational data are unavailable or unusable for laboratory testing and therefore the reference SDM has to be completed starting from standard PSD profiles. Defining the CSD terms with no information about the cross-correlation between each pair of control channels could be complicated and it could not guarantee the physical meaning of the control target. The procedure currently suggested by the Standards, when operational measurements are not fully available and the test specifications are provided in terms of PSDs only, is the so called *Independent References Method* (or *0ph-Lcoh Method*). The *IRM* specifies the reference SDM as a diagonal matrix by simply setting low coherence for all the cross terms. This techniques is user-friendly and it always complies with both mathematical and physical requirements. For this reasons, nowadays the *IRM* is the most common MIMO target technique.

The purpose of the this thesis was to provide alternative solutions that, in addition to meeting the mathematical constraints, were able to offer additional contributions to enhance the quality of the control test. In particular, two distinct aspect have been explored. Firstly, the possibility to replicate the PSD test specifications by exploiting as low drives power as possible. Secondly, the possibility of combining the PSD test specifications in order to get out the maximum dynamic response from the specimen under test. Both aspects are critical issues when performing environmental control test. The former is even mentioned in the US Military Standard as *minimum drives criteria*. The idea of reducing the power required by the multiple shakers to perform the control test is a desired solution because it preserves the excitation system, avoiding possible DACs overloads which could damage the expensive test equipments. In this context, two novel MIMO target generation techniques have been disclosed in Chapter 4 of this thesis, namely *Minimum Drives Method (MDM)* and *Minimum Single Drive Method (MSDM)*. Both are focused on the drives power reduction, but the *MDM* aims to equally minimise all the multiple

drives of the excitation system, the *MSDM* instead, has been developed for managing the case in which most of the power is required by a specific drive of the multiple shakers. Even if the final goal of the two MIMO target techniques is different, the basic architecture of both the algorithms is the same. Both are based on the *Phase Pivoting Principle* which is the innovative phase selection methodology proposed in this thesis in order to obtain physically realizable reference matrices. The novel techniques have been theoretically and experimentally compared with respect to the nowadays state-of-the-art procedures. Specifically, the experimental campaign has been carried out with the 3-DoF shaker table. Moreover, in order to point out the pros and the cons of each technique, the control tests have been performed adopting different number control channels and controlling test specifications with different shape profiles and different bandwidths. For all the combinations tested, the *MDM* resulted the MIMO target procedure which offered higher drives power reduction: about the 30% with respect to the standard *IRM*. The test results also confirmed the impressive efficacy of the *MSDM* on minimising the overworked drive by fairly spreading the drives power in a more advantageous way. Generally, an extra power reduction on the overstressed drive of 10-15% compared to the *MDM*.

Finally, it is worth to underline that both the procedures are fully automated. This feature is a remarkable novelty of the proposed methods because, firstly, no extra data are required to complete the control target, except the reference PSDs (test specifications) and the FRFs matrix (anyhow estimated in the pre-test phase of any control test). Secondly, no particular experience of matrix computations is required of the user who wants to carry out the control test. For these reasons, and for the notable capability of preserving the test equipment, the *MDM* has been recently implemented in the environmental control solutions of Simcenter Testlab (release 2019.1.3).

The investigation of the control target techniques finally concludes in Chapter 5, which shows the critical analysis carried out on the effects caused by the application of different MIMO control targets on the fatigue-life of the specimen under test. In this context, an innovative procedure has been proposed, namely the *Extreme Dynamic Response Method (EDRM)*, which aims to combine the test specifications in order to recreate in the laboratory the most severe vibration environment possible. The objective of the *EDRM* is to fully exploit the test specifications to proper excite the specimen dynamic in the entire

frequency band of interest and thus to influence the fatigue behaviour of the specimen. The *EDRM* has been compared with the standard solution *IRM* (also called *0ph-Lcoh Method*) via intense fatigue-testing campaign, during which 48 specimens have been tested until rupture by means of the 3-DoF shaker table at the University of Ferrara. The specimens have been specifically designed for this application. Thus, they were cantilever beams with rectangular section, made of aluminium alloy and notched near the location of maximum bending moment, in order to localise the zone of prevalent damage accumulation. Moreover, the comparison between the novel technique and the standard one, has been done by tacking into account two different excitation bandwidths, i.e. the *single-mode excitation* and the *multi-mode excitation*. With the former, just one bending mode of the specimen was excited. With the latter instead, two bending modes with different bending plane were simultaneously excited. First of all it is worth to underline that, in both the excitation modalities, the use of the *EDRM* has always induced the shortest time-to-failure of the specimen under test. The average life duration caused by the *EDRM* was typically 40-50 % lower than the standard *IRM*. The average time-to-failure reduction between the two methods, in one case even reached the 72%. These results confirmed the potential of the proposed MIMO target technique to recreate in the laboratory the most extreme vibration conditions, starting from the same set of PSD test specifications.

However, more generally the comparison of the fatigue tests carried out with different excitation modes, led to distinct final observations. In *single-mode excitation*, the response SDMs resulting from the two MIMO target techniques were simply scaled between each other. As a consequence, the two corresponding data set have been approximated by the same S-N curve. Moreover, at the end of the test, the two techniques exhibited fracture surfaces with identical microscopical characteristics. Therefore, when a single mode shape is excited the *EDRM* and the *IRM* cause the same fatigue damage. Under this hypothesis, the *EDRM* can be considered as a methodology to accelerate the multi-axial fatigue test, starting from specified multiple reference PSDs.

In contrast, the fatigue tests carried out in *multi-mode excitation* demonstrated that the resulting response SDMs were not equally scaled between each other in the entire frequency band of excitation. The multiple mode shapes were excited with different intensity, according to the capabilities of the adopted MIMO target technique. Consequently, the fatigue results of the *EDRM* and

the *IRM* have been approximated with distinct S-N curves, thus leading to distinct fracture surfaces. Therefore it can be concluded that, when multiple mode shapes are simultaneously excited, the particular methodology adopted for combining the test specifications significantly alters the fatigue behaviour of the specimen under test. This implies that, in case of missing operational CSDs, the laboratory conditions will differ from the in-field ones whichever the adopted MIMO target generation technique (*EDRM*, *IRM*, etc.). The risk is to underestimate the fatigue damage to undergo the specimen during laboratory testing. In this context the *EDRM* at least guarantees to recreate in the laboratory the most severe conditions possible, and thus to subject the specimen to the most damaging vibration environment.

BIBLIOGRAPHY

[1] U. Musella, G. D'Elia, A. Carrella, B. Peeters, E. Mucchi, F. Marulo, and P. Guillaume. "A minimum drives automatic target definition procedure for multi-axis random control testing." In: *Mechanical Systems and Signal Processing* 107 (2018), pp. 452–468. DOI: 10.1016/j.ymssp.2018.01.039.

[2] G. D'Elia, U. Musella, E. Mucchi, P. Guillaume, and B. Peeters. "Analyses of drives power reduction techniques for multi-axis random vibration control tests." In: *Mechanical Systems and Signal Processing* 135 (2020). DOI: 10.1016/j.ymssp.2019.106395.

[3] G. D'Elia and E. Mucchi. "Comparison of single-input single-output and multi-input multi-output control strategies for performing sequential single-axis random vibration control test." In: *JVC/Journal of Vibration and Control* 26.21-22 (2020), pp. 1988–2000. DOI: 10.1177/1077546320909975.

[4] United States Department of Defence. "Environmental Engineering Considerations and Laboratory Tests." In: *MIL-STD 810G w/CHANGE 1* (2014).

[5] Ministere de la Defense Delegation Generale pour l'armement. "Essais generaux en environment des materials (General tests of materials in environment)." In: *GAM EG-13* (1986).

[6] North Atlantic Treaty Organization NATO. "Environmental Testing - AECTP-100-600." In: *STANG 4370* (2019).

[7] S.J. Zand. "Three Hundred Years of Vibration Engineering." In: *Zeitschrift fur angewandte mathematik and physik* IXb.5-6 (1958), pp. 737–747.

[8] V.J. Junker. "The evolution of USAF Environmental Testing. Dynamic problems in flight vehicles." In: *Task 137010. Wright-Petterson Air Force Base* Command: i-73 (1965).

[9] Department of the Air Force Wright-Patterson Air Force Base. "Military Standard Environmental Test Methods for Aerospace and Ground Equipment." In: *MIL-STD 810A* (1962).

[10] D. Rizzo and M. Blackburn. "The history of a decision: A standard vibration test method for qualification." In: *Journal of the IEST* 60.1 (2017), pp. 9–20. DOI: 10.17764/1098-4321.60.1.9.

[11] International Organization for Standardization. "Road vehicles - Environmental conditions and testing for electrical and electronic equipment." In: *ISO 16750-3* (2012).

[12] D. Gregory, F. Bitsie, and D.O. Smallwood. "Comparison of the response of a Simple Structure to Single Axis and Multiple Axis Random Vibration Inputs." In: *Proc. of 79th Shock and Vibration Symposium* (2008).

[13] M. Ernst, E. Habtour, A. Dasgupta, M. Pohland, M. Robeson, and M. Paulus. "Comparison of electronic component durability under uniaxial and multiaxial random vibrations." In: *Journal of Electronic Packaging, Transactions of the ASME* 137.1 (2015). DOI: 10.1115/1.4028516.

[14] L.D. Jacobs, G.D. Nelson, and J.H. Hofer. "Responses of structures to SDoF vs. MDoF vibration testing." In: *Proc. of the Society for Experimental Mechanics Series* 5 (2016), pp. 83–94. DOI: 10.1007/978-3-319-29859-7_9.

[15] G. Nelson and L. Jacobs. "Comparison of Multi-Axis and Single Axis Testing on Plate Structures." In: *Proc. of the 85th Shock and Vibration Symposium* (2019).

[16] Y. Soucy and A. Côté. "Reduction of overtesting during vibration tests of space hardware." In: *Canadian Aeronautics and Space Journal* 48.1 (2002), pp. 77–86. DOI: 10.5589/q02-006.

[17] M.A. Underwood and T. Keller. "8 Actuator System provides 1 DOF to 6 DOF controlled Satellite Qualification Testing up to 100 Hz." In: *Proc. of 28th Aerospace Testing Seminar* (2014).

[18] P.M. Daborn, C. Roberts, D.J. Ewins, and P.R. Ind. "Next-generation random vibration tests." In: *Proc. of the Society for Experimental Mechanics Series* 8 (2014), pp. 397–410. DOI: 10.1007/978-3-319-04774-4_37.

[19] P.M. Daborn, P.R. Ind, and D.J. Ewins. "Enhanced ground-based vibration testing for aerodynamic environments." In: *Mechanical Systems and Signal Processing* 49.1-2 (2014), pp. 165–180. DOI: 10.1016/j.ymssp.2014.04.010.

[20] P.M. Daborn. "Scaling up of the Impedance-Matched Multi-Axis Test (IMMAT) technique." In: *Proc. of the Society for Experimental Mechanics Series* 9B (2017), pp. 1–10. DOI: 10.1007/978-3-319-54735-0_1.

[21] C. Roberts and D. Ewins. "Multi-axis vibration testing of an aerodynamically excited structure." In: *Journal of Vibration and Control* 24.2 (2018), pp. 427–437. DOI: 10.1177/1077546316642064.

[22] M.A. Underwood and T. Keller. "Rectangular control of multi-shaker systems: Theory and practical results." In: *Journal of the IEST* 47 (2004), pp. 80–86. DOI: 10.17764/jiet.47.1.u8558668l644n166.

[23] W.E. Whiteman and M. Berman. "Inadequacies in uniaxial stress screen vibration testing." In: *Journal of the IEST* 44.4 (2001), pp. 20–23. DOI: 10.17764/jiet.44.4.f72822w825r1156j.

[24] W.E. Whiteman and M.S. Berman. "Fatigue failure results for multi-axial versus uniaxial stress screen vibration testing." In: *Shock and Vibration* 9.6 (2002), pp. 319–328. DOI: 10.1155/2002/109715.

[25] M. Mršnik, J. Slavič, and M. Boltežar. "Multiaxial vibration fatigue - A theoretical and experimental comparison." In: *Mechanical Systems and Signal Processing* 76-77 (2016), pp. 409–423. DOI: 10.1016/j.ymssp.2016.02.012.

[26] H. Himelblau and M.J. Hine. "Effects of Triaxial and Uniaxial Random Excitation on the Vibration Response and Fatigue Damage of Typical Spacecraft Hardware." In: *Proc. of 66th Shock and Vibration Symposium* (1995).

[27] M.A. Underwood, T. Keller, and R. Ayres. "Multi-shaker control: A review of the evolving state-of-the-art." In: *Sound and Vibration* 51.8 (2017), pp. 8–16.

[28] D.O. Smallwood. *A Random Vibration Control System for Testing a Single Test Item with Multiple Inputs*. Tech. rep. Sandia National Laboratories, 1982.

[29] M.A. Underwood. *Applications of Digital Computers, in: Shock and Vibration Handbook*. New York (NY), US: Mc. Graw Hill, 2001, pp. 27.1–27.36.

[30] M.A. Underwood. *Adaptive control method for multiexciter sine tests*. Tech. rep. United States Patent, nr. 5299459, 1994.

[31] M. Appolloni, R. B. Daca, A. Cozzani, and R. Knockaert. "Multi-Degrees-Of-Freedom vibration platform with MIMO Controller for future spacecraft testing and application case for virtual shaker testing." In: *Proc. of 29th Aerospace Testing Seminar* (2015).

[32] United States Department of Defence. "Environmental Engineering Considerations and Laboratory Tests. METHOD 527.1: Multi-Exciter Test." In: *MIL-STD 810G w/CHANGE 1* (2014).

[33] M.A. Underwood. "Multi-exciter testing applications: theory and practice." In: *Proc. of Institute of Environmental Sciences and Technology* (2002).

[34] P. K. Aggarwal. *Dynamic (Vibration) Testing: Design Certification of Aerospace System*. Tech. rep. NASA Marshall Space Flight Center, 2010.

[35] M. Alvarez Blanco, K. Janssens, and F. Bianciardi. "Experimental verification of projection algorithms and optimization routines for acoustic field uniformity enhancement in MIMO direct field acoustic control." In: *Proc. of ISMA 2016 - International Conference on Noise and Vibration Engineering* (2016), pp. 17–31.

[36] D. Benasciutti and R. Tovo. "Fatigue life assessment in non-Gaussian random loadings." In: *International Journal of Fatigue* 28.7 (2006), pp. 733–746. DOI: 10.1016/j.ijfatigue.2005.09.006.

[37] M. Troncossi and A. Rivola. "Response analysis of specimens excited with non-Gaussian acceleration profiles." In: *Proc. of ISMA 2014 - International Conference on Noise and Vibration Engineering and USD 2014 - International Conference on Uncertainty in Structural Dynamics* (2014), pp. 799–808.

[38] P. Wolfsteiner. "Fatigue assessment of non-stationary random vibrations by using decomposition in Gaussian portions." In: *International Journal of Mechanical Sciences* 127 (2017), pp. 10–22. DOI: 10.1016/j.ijmecsci.2016.05.024.

[39] M. Palmieri, M. Česnik, J. Slavič, F. Cianetti, and M. Boltežar. "Non-Gaussianity and non-stationarity in vibration fatigue." In: *International Journal of Fatigue* 97 (2017), pp. 9–19. DOI: 10.1016/j.ijfatigue.2016.12.017.

[40] R. Zheng, H. Chen, D. Vandepitte, and Z. Luo. "Multi-exciter stationary non-Gaussian random vibration test with time domain randomization." In: *Mechanical Systems and Signal Processing* 122 (2019), pp. 103–116. DOI: 10.1016/j.ymssp.2018.12.013.

[41] R. Zheng, H. Chen, X. He, and D. Vandepitte. "Multiple-input multiple-output non-stationary non-Gaussian random vibration control by inverse system method." In: *Mechanical Systems and Signal Processing* 124 (2019), pp. 124–141. DOI: 10.1016/j.ymssp.2019.01.055.

[42] A. Steinwolf, B. Cornelis, B. Peeters, H. Van Der Auweraer, A. Rivola, and M. Troncossi. "On the use of kurtosis control methods in shaker testing for fatigue damage." In: *Journal of Testing and Evaluation* 48.1 (2020). DOI: 10.1520/JTE20180149.

[43] A. Angeli, B. Cornelis, and M. Troncossi. "Synthesis of Sine-on-Random vibration profiles for accelerated life tests based on fatigue damage spectrum equivalence." In: *Mechanical Systems and Signal Processing* 103 (2018), pp. 340–351. DOI: 10.1016/j.ymssp.2017.10.022.

[44] C. Lalanne. *Mechanical Vibration and Shock Analysis*. 3rd ed. Vol. 5: Specification Development. USA: John Wiley & Sons, 2014.

[45] D.O. Smallwood. *Multiple Shaker Random Vibration Control - An Update*. Tech. rep. Sandia National Laboratories, 1999.

[46] M.A. Underwood and T. Keller. "Recent system developments for multi-actuator vibration control." In: *Sound and Vibration* 35 (2001), pp. 16–33.

[47] M.A Underwood, R. Ayres, and T. Keller. "Filling in the MIMO matrix part 1- Performing random tests using field data." In: *Sound and Vibration* 45.3 (2011), pp. 8–14.

[48] S. Ammanagi and C.S. Manohar. "Optimal cross-spectrum of road loads on vehicles: theory and experiments." In: *Journal of Vibration and Control* 22.19 (2016), pp. 4012–4024. DOI: 10.1177/1077546315570107.

[49] L.A. Martin and S.P. Schneider. "Spectral density matrices used to characterize vibration environments." In: *Sound and Vibration* 51.11 (2017), pp. 8–13.

[50] M. Ross, L.D. Jacobs, G. Tipton, G. Nelson, K. Cross, N. Hunter, and J. Harvie. "6-DOF shaker test input derivation from field test." In: *Proc. of the Society for Experimental Mechanics Series* 9B (2017), pp. 11–22. DOI: 10.1007/978-3-319-54735-0_2.

[51] L.D. Jacobs, M. Ross, G. Tipton, K. Cross, Jr. Hunter N., J. Harvie, and G. Nelson. "Experimental execution of 6DOF tests derived from field tests." In: *Proc. of the Society for Experimental Mechanics Series* 9B (2017), pp. 125–132. DOI: 10.1007/978-3-319-54735-0_14.

[52] U. Musella, M.A. Blanco, D. Mastrodicasa, G. Monco, E. Di Lorenzo, S. Manzato, B. Peeters, E. Mucchi, and P. Guillaume. "Combining Test and Simulation to Tackle the Challenges Derived from Boundary Conditions Mismatches in Environmental Testing." In: *Proc. of 37th IMAC Conference* (2019).

[53] B. Peeters and J. Debille. "MIMO Random Vibration Control: algorithm and simulations." In: *Proc. of the Shock and Vibration Symposium* (2016).

[54] B. Peeters and J. Debille. "Multiple-input-multiple-output random vibration control: Theory and practice." In: *Proc. of the 2002 International Conference on Noise and Vibration Engineering, ISMA* (2002), pp. 507–516.

[55] D.O. Smallwood, Tom D. Woodall, and E.J. Buksa. "Minumum Drive requirements for a multiple input multiple output linear system." In: *Proc. of Annual Technical Meeting - Institute of Environmental Sciences* (1986), pp. 295–301.

[56] D.O. Smallwood. "Multiple-Input Multiple-Output (MIMO) linear systems extreme inputs/outputs." In: *Shock and Vibration* 14.2 (2007), pp. 107–131. DOI: 10.1155/2007/701837.

[57] D.O. Smallwood. "Minimum input trace for multiple input multiple output linear systems." In: *Proc. of 59th Annual Technical Meeting of the Institute of Environmental Sciences and Technology: Connect, Learn, Grow, Recharge, ESTECH 2013* (2013), pp. 625–643.

[58] D.O. Smallwood. "A Proposed Method To Generate a Spectral Density Matrix for a Multiple Input, Multiple Output (MIMO) Vibration Test." In: *Proc. of 80th Shock and Vibration Symposium* (2010).

[59] J.S. Bendat and A.G. Piersol. *Random Data: Analysis and Measurement Procedures*. 4rd ed. Vol. 729. New York (NY), US: John Wiley and sons, 2011.

[60] G.H. Golub and C.F. Van Loan. *Matrix Computations*. 3rd ed. Baltimore: The Johns Hopkins University Press, 1996.

[61] S.L. Campbell and C.D Meyer Jr. *Generalized inverses of linear transformations*. New York: Dover Pub. Inc., 1991.

[62] W. Heylen, S. Lammens, and P. Sas. *Modal Analysis Theory and Testing*. 2nd ed. Katholieke Universiteit Leuven, Faculty of Engineering, Department of Mechanical Engineering, Division of Production Engineering, Machine Design and Automation, 1998.

[63] D.O. Smallwood and T.L. Paez. "A frequency domain method for the generation of partially coherent normal stationary time domain signals." In: *Shock and Vibration* 1.1 (1993), pp. 45–53. DOI: 10.3233/SAV-1993-1106.

[64] H. Caruso and A. Dasgupta. "A Fundamental Overview of Accelerated Testing Analytical Models." In: *Journal of the IEST* 41.1 (1998), pp. 16–20. DOI: 10.17764/jiet.41.1.3626j43p305q1978.

[65] Charles R. Farrar, Thomas A. Duffey, Phillip J. Cornwell, and Matthew T. Bement. "Review of methods for developing accelerated testing criteria." In: *Proc. of the International Modal Analysis Conference - IMAC* 1 (1999), pp. 608–614.

[66] B. Cornelis, S. Manzato, B. Peeters, R.V. der Vorst, and J. Hiatt. "A mission synthesis procedure for sine-on-random excitations in a helicopter application." In: *Proc. of the Society for Experimental Mechanics Series* 9B (2017), pp. 197–209. DOI: 10.1007/978-3-319-54735-0_21.

[67] C. Lalanne and M. Bozio. "Writing a Mechanical Vibration Specification From E.R.S. and F.D.S." In: *ESTECH 2002, IEST - 48th Annual Technical Meeting and Exposition* (2002).

[68] C. Lalanne. *Mechanical vibration and shock analysis*. 3rd ed. Vol. 4: Fatigue Damage. John Wiley & Sons, 2014.

[69] A.M. Hopf. "Highly accelerated life testing for design and process improvement." In: *S V Sound and Vibration* 27.11 (1993), pp. 20–24.

[70] G. Allegri and X. Zhang. "On the inverse power laws for accelerated random fatigue testing." In: *International Journal of Fatigue* 30.6 (2008), pp. 967–977. DOI: 10.1016/j.ijfatigue.2007.08.023.

[71] G.M. Hieber. "Use and abuse of test time exaggeration factors." In: *Test Engineering and Management* 61.2 (1999), pp. 14–16.

[72] L.D. Lutes and S. Sarkani. *Random vibrations: analysis of structural and mechanical systems*. Butterworth-Heinemann, 2004.

[73] M.A. Miner. "Cumulative damage in fatigue." In: *Journal of Applied Mechanics* 12 (1945), pp. 149–164.

[74] D. Benasciutti and R. Tovo. "Spectral methods for lifetime prediction under wide-band stationary random processes." In: *International Journal of Fatigue* 27.8 (2005), pp. 867–877.

[75] K.G.F. Janssens. "Universal cycle counting for non-proportional and random fatigue loading." In: *International Journal of Fatigue* 133 (2020). DOI: 10.1016/j.ijfatigue.2019.105409.

[76] D.E. Newland. *An Introduction of Random Vibration and Spectral Analysis*. Essex, England: Longmsn Group Limited, 1993.

[77] P.H. Wirsching, T.L. Paez, and K. Ortiz. *Random Vibrations: Theory and Practice*. Dover Publications, 2006.

[78] T. Dirlik. "Application of Computers in Fatigue Analysis." In: *Ph.D. Thesis, University of Warwick* (1985).

[79] A. Niesłony. "Comparison of some selected multiaxial fatigue failure criteria dedicated for spectral method." In: *Journal of theoretical and applied mechanics* 48.1 (2010), pp. 233–254.

[80] A. Yaich and A. El Hami. "Multiaxial fatigue damage estimation of structures under random vibrations using Matsubara's criterion." In: *International Journal of Fatigue* 124 (2019), pp. 253–264. DOI: 10.1016/j.ijfatigue.2019.03.003.

[81] A. Niesłony and E. Macha. *Spectral Method in multiaxial fatigue*. 2007.

[82] A. Preumont and V. Piefort. "Predicting random high-cycle fatigue life with finite elements." In: *Journal of Vibration and Acoustics, Transactions of the ASME* 116.2 (1994), pp. 245–248. DOI: 10.1115/1.2930420.

[83] A. Carpinteri, A. Spagnoli, and S. Vantadori. "Reformulation in the frequency domain of a critical plane-based multiaxial fatigue criterion." In: *International Journal of Fatigue* 67 (2014), pp. 55–61. DOI: 10.1016/j.ijfatigue.2014.01.008.

[84] A. Cristofori, D. Benasciutti, and R. Tovo. "A stress invariant based spectral method to estimate fatigue life under multiaxial random loading." In: *International Journal of Fatigue* 33.7 (2011), pp. 887–899. DOI: 10.1016/j.ijfatigue.2011.01.013.

[85] X. Pitoiset, A. Kernilis, A. Preumont, and V. Piéfort. "Some tools for a multiaxial random fatigue analysis with finite elements." In: *European Journal of Mechanical and Environmental Engineering* 44.1 (1999), pp. 11–15.

[86] X. Pitoiset and A. Preumont. "Spectral methods for multiaxial random fatigue analysis of metallic structures." In: *International Journal of Fatigue* 22.7 (2000), pp. 541–550. DOI: 10.1016/S0142-1123(00)00038-4.

[87] D. Benasciutti. "Some analytical expressions to measure the accuracy of the "equivalent von Mises stress" in vibration multiaxial fatigue." In: *Journal of Sound and Vibration* 333.18 (2014), pp. 4326–4340. DOI: 10.1016/j.jsv.2014.04.047.

[88] A. Karolczuk, M. Kurek, and T. Łagoda. "Fatigue life of aluminium alloy 6082 T6 under constant and variable amplitude bending with torsion." In: *Journal of Theoretical and Applied Mechanics (Poland)* 53.2 (2015), pp. 421–430. DOI: 10.15632/jtam-pl.53.2.421.

[89] A. Pothula, A. Gupta, and G.R. Kathawate. "Fatigue failure in random vibration and accelerated testing." In: *JVC/Journal of Vibration and Control* 18.8 (2012), pp. 1199–1206. DOI: 10.1177/1077546311419545.

[90] Yu Jiang, Gun Jin Yun, Li Zhao, and Junyong Tao. "Experimental Design and Validation of an Accelerated Random Vibration Fatigue Testing Methodology." In: *Shock and Vibration* 2015 (2015), pp. 1–13. DOI: 10.1155/2015/147871.

[91] R.G. Budynas and J.K. Nisbett. *Shigley's Mechanical Engineering Design*. 9rd ed. McGraw-Hill, 2011.

[92] H.T. Corten and T.J. Dolon. "Cumulative fatigue damage." In: *Institution of mechanical engineering and american society of mechanical engineers* (1956), 235–246.

[93] A.M. Freudenthal and R.A. Heller. "On stress interaction in fatigue and a cumulative damage rule." In: *Journal of the Aerospace Sciences* 26 (1959), 431–42.

[94] S.A. Clevenson and R. Steiner. "Fatigue life under random loading for several power spectral shapes." In: *NASA-TR-266, Langley Station, Hampton, VA* (1967).

[95] L.W. Root. "Random-sine fatigue data correlation." In: *The Shock and Vibration Bulletin* 33.II (1964), 279–285.

[96] Y.L. Lee, J. Pan, R. Hathaway, and M. Barkey. *Fatigue Testing and Analysis: Theory and Practice*. 2008, p. 416.

[97] ASTM International. "Standard Practice for Statistical Analysis of Linear or Linearized Stress-Life and Strian-Life (S-N) Fatigue Data." In: *Designation:E739-10* ().

[98] New York. *Statistical Theory and Methodology in Science and Engineering*. 2rd ed. John Wiley and sons, 1965.

[99] M. Paulus and A. Dasgupta. "Semi-empirical life model of a cantilevered beam subject to random vibration." In: *International Journal of Fatigue* 45 (2012), pp. 82–90. DOI: 10.1016/j.ijfatigue.2012.06.008.

[100] J.W. Tukey. *Exploratory Data Analysis*. London, 1977.

[101] D.C. Montgomery and G.C. Runger. *Applied Statistics and Probability for Engineers*. 6rd ed. John Wiley & Sons, 2014.

[102] J.L. Gonzalez-Velázquez. *Fractography and Failure Analysis*. 1rd ed. Vol. Structural Integrity Book 3. Springer, 2018.

[103] A.J. McEvily and J. Kasivitamnuay. *Metal Failures: Mechanisms, Analysis, Prevention*. 2rd ed. John Wiley & Sons, 2013, p. 504.